
**Description and modification of electron beam
induced deposits for plasmonics**

**Im Fachbereich Physik der
Freien Universität Berlin eingereichte
Dissertation**

**zur Erlangung des akademischen Grades
Doktor der Naturwissenschaften
- Dr. rer. nat -**

vorgelegt von
Caspar Haverkamp

2017

Erstgutachterin: Prof. Dr. Silke Christiansen

Zweitgutachter: Dr. Ivo Utke

Disputation am: 20.10.2017

Contents

1	Introduction	1
2	Fundamentals and experimental methods	3
2.1	Basic electrodynamics	3
2.2	Permittivity models	9
2.3	Scattering: From classical scatterer to plasmonics	17
2.4	Optical measurements	22
2.5	Simulation of electromagnetic waves	26
2.6	Scanning electron and transmission electron microscopy	29
2.7	Electron beam induced deposition (EBID): Process and purification	31
3	From common to novel EBID precursors applied to plasmonics	38
3.1	MeCpPtMe ₃ (Platinum)	38
3.1.1	Structural properties of EBID-platinum	39
3.1.2	Permittivity of EBID-platinum: Optical measurements and a model	42
3.2	Me ₂ Au(acac) (Gold)	46
3.2.1	Structural properties of EBID-gold	47
3.2.2	Plasmonic nanostructures by EBID-gold: Fabrication and optical properties	48
3.3	Cu(tbaoac) ₂ (Copper)	52
3.3.1	A novel copper precursor for EBID: Deposition and 3D structures	54
3.3.2	Structural properties of EBID-copper	57
3.3.3	Permittivity of EBID-copper: Optical measurements and a model	61
3.3.4	Plasmonic scattering by EBID-copper	65
4	Coating EBID nanostructures: From PVD to ALD	67
4.1	EBID helices with a pure gold shell by physical vapor deposition (PVD)	69
4.1.1	Darkfield scattering of a single helix	69
4.1.2	Dissymmetry transmission measurement and simulation	71

4.2	Atomic layer deposition (ALD) of platinum on EBID nanostructures	74
4.2.1	Properties of ALD platinum	76
4.2.2	ALD coated EBID nanostructures: Scattering and dissymmetry	80
5	Purification of EBID nanostructures	84
5.1	Purification of an EBID-gold pillar with water vapor	85
5.2	Plasma purification of EBID-gold nanostructures	85
5.2.1	Geometrical modification by plasma purification: Core-shell structure . .	86
5.2.2	Quality of gold shell after purification	88
5.2.3	Plasmonic scattering of a single purified EBID-gold helix	91
5.2.4	Limitations of plasma purification of nanostructures	92
6	Summary and Outlook	95
	Kurzfassung	99
	Abstract	100
	References	101

1 Introduction

3D printing is a relatively new technological development which holds the promise to change the way of production in many areas. Some refer to it as a new technological revolution [1]. With this method it is possible to produce three-dimensional objects with a feature size around $150\ \mu\text{m}$ [2]. The desired structure is designed with a 3D CAD software and then realized by the printer [1]. Even printing of biological tissue is currently investigated, with the goal to rebuild whole organs [3]. While this technique can be used to fabricate macroscopic objects, other techniques have to be employed to structure material with the same flexibility on a microscopic scale. One possible microscopic production method is two-photon direct laser writing. With this method, the focus of the laser beam is used to directly cure exposed photoresist while the unexposed resist is subsequently removed. With this technique it is e.g. possible to build small lenses directly on top of optical fibers [4].

Even smaller features, with the advantage of single-step production, can be realized by focused electron/ion beam induced deposition (FIBID/EBID) [5, 6]. For this process, a precursor is vaporized and locally injected into a scanning electron microscope. Through the impact of the electron beam the molecules are separated into a volatile part which is pumped out of the chamber and a part which is bound to the substrate [7]. The three-dimensional patterning is achieved by moving the electron beam above the substrate, which can also be combined with a CAD software to create the desired shape [5]. A variety of different precursors exist to deposit materials including insulators, metals and semiconductors [8]. With its ability to deposit structured material in a size range well below the optical wavelength, EBID is a promising candidate for the fabrication of metamaterials. Metamaterials are structures designed and assembled from artificial building blocks. In the same way as the optical properties of conventional materials are determined by the effective response of their atoms and the average over all electro-magnetic variations of the atomic structure, metamaterials obtain their optical properties from their building blocks. This is only given, and by definition true for metamaterials, with sizes of the building blocks significantly below the interacting wavelength [9]. Through design of the individual building blocks, materials can be created which have properties not found in nature.

In addition, the ability to grow metallic structures makes EBID a valuable tool for the fabrication of plasmonic structures. The field of plasmonics investigates the interaction of electro-magnetic fields with small metallic particles as well as with metal-dielectric interfaces [10]. One of the most famous examples is the high scattering cross-section of small metallic particles which has its origin in the excitation of a free electron gas inside the metal, a so-called localized surface plasmon. The theoretical description of a plane wave scattered at a sphere has been developed

by Mie [11] and is referred to as Mie theory. The scattering intensity and the strong localized near-field depend on the material as well as on the shape of the particle [10]. From a geometrical point of view is EBID with its nanometer lateral resolution and three-dimensional growth capabilities a most suitable method to fabricate plasmonic structures. However, most of the metal containing EBID precursors result in a material with a high carbon content and thus a weak metal response. The typical morphology is a carbonaceous matrix in which small metal particles are embedded,[12] limiting the use of EBID for plasmonic application. Despite this drawback of carbon contamination, already as-deposited EBID material shows interesting optical properties. An array of EBID-platinum helices shows polarization dependent light transmission, acting as a circular polarizer [13]. Simulation of the performance with different metal content shows an increase in optical response when increasing the metal content of the material. To truly understand the optical response of an array it is crucial to know the response of the individual structure.

The focus of this thesis lies on the characterization of EBID materials and their modification to allow for an optical description of single metallic EBID nanostructures, such as helices. To accurately describe the optical response of a material, its complex dielectric function has to be determined. This is difficult for EBID materials because of their small structural size, making common techniques as ellipsometry not easy applicable. In this thesis the complex dielectric function will be determined by imaging ellipsometry as well as by numerical analyzing transmission and reflection and described by a Maxwell-Garnett model. It will be investigated to which extent the metal influences the properties of the EBID material, since it just contributes a minor fraction to the material content while the material mostly consists of carbon. Furthermore, the improvement of the plasmonic response when adding a pure metallic shell onto the structure is addressed. Different methods are used such as post-coating of the nanostructures with pure metal as well as purification of the nanostructure itself. Post-coating deposition of a pure metal shell by physical vapor deposition (PVD) as well as by a novel coating of EBID nanostructures with atomic layer deposition (ALD) is presented. During purification carbon of the outer part of the structure is removed resulting in a shell with a much higher metal content. In this thesis the effect of oxygen plasma purification, especially on 3D nanostructures, will be investigated. Additionally the thesis contributes into the search of new EBID precursors, aiming for the possibility to deposit other metals, but also for deposition with higher metal content. A new copper containing precursor is investigated with regard to its deposition properties, its chemical composition and optical properties. Besides the possible plasmonic applications of copper due to its similar electron configuration as silver and gold, it could also replace the commonly used platinum precursor for electrical contacting in electron microscopy as copper is more conductive.

2 Fundamentals and experimental methods

If not explicitly mentioned otherwise the content of the following chapter is taken from textbooks [14–16].

2.1 Basic electrodynamics

The base of description for all electrodynamic effects is provided by Maxwell's equations. These equations give an accurate description even for small objects with just a few nanometers in size without the need for quantum mechanic corrections. Although for the description of the material response to electro-magnetic fields often quantum mechanic theory is required, e.g. to derive the bandstructure and herewith explaining the spectral dependent absorption of semiconductors. However, these effects can often be added into the classical description of the material in a phenomenological approach. The macroscopic Maxwell equations are four coupled partial differential equations:

$$\operatorname{div} \mathbf{D} = \rho_{\text{free}}, \quad \operatorname{div} \mathbf{B} = 0 \quad (2.1)$$

$$\operatorname{rot} \mathbf{E} = -\frac{\partial \mathbf{B}}{\partial t}, \quad \operatorname{rot} \mathbf{H} = \left(\frac{\partial \mathbf{D}}{\partial t} + \mathbf{J}_{\text{free}} \right) \quad (2.2)$$

Here, \mathbf{E} is electric field strength, \mathbf{D} is the electric displacement field, \mathbf{H} is the magnetic field strength and \mathbf{B} is magnetic flux. ρ_{free} and \mathbf{J}_{free} are the free charges and currents, respectively. Maxwell's equations state that charges are the source of the electric displacement and that the magnetic field is charge free, equation 2.1. The two rotational equations 2.2 couple the electric and magnetic fields with each other. In vacuum the two fields \mathbf{E} , \mathbf{D} for the electric part and \mathbf{H} , \mathbf{B} for the magnetic part are proportional to each other and connected by the permittivity of vacuum ϵ_0 and permeability of vacuum μ_0 . In matter the effects of polarization \mathbf{P} and magnetization \mathbf{M} have to be included.

$$\mathbf{D} = \epsilon_0 \mathbf{E} + \mathbf{P} \quad (2.3)$$

$$\mathbf{H} = \frac{1}{\mu_0} (\mathbf{B} - \mathbf{M}) \quad (2.4)$$

These can be permanent effects which arise from specific crystal structures or can be induced by the impinging field. Equations 2.3 and 2.4 are the material equations. In this formulation all quantities are averaged over the microscopic fields \mathbf{E} and \mathbf{B} . The dipole field \mathbf{P} can be induced by an electric field \mathbf{E} and has in the first approximation a linear relation, $\mathbf{P} = \varphi \epsilon_0 \mathbf{E}$. The proportion-

ality factor, in time space, between the polarization field and the electric field is called electric susceptibility. Materials can have permanent polarization due to their crystal structure or charge displacement in molecules. This additional polarization can be added as a constant polarization effect to the one which is induced by an external electric field. In the following the permanent polarization is assumed to be zero. For timescales of the electro-magnetic field in the same order as the ones for the polarization, the relation between \mathbf{E} and \mathbf{P} becomes more complicated. In this case the polarization does not occur instantly but depends on the electric field at all previous times up to now

$$\mathbf{P} = \int_{-\infty}^t d\tau \varphi(t - \tau) \epsilon_0 \mathbf{E}(t - \tau). \quad (2.5)$$

Taking the Fourier transformation with respect to the time of \mathbf{E} and \mathbf{P} with the convolution theorem and considering isotropic material, the relation in the frequency domain is

$$\mathbf{P} = \epsilon_0 \alpha \mathbf{E}. \quad (2.6)$$

α is called the polarizability. Inserting the polarization into equation 2.3 leads to the relation between \mathbf{E} and \mathbf{D} .

$$\mathbf{D} = \epsilon_0 \underbrace{(1 - \alpha)}_{\epsilon_r} \mathbf{E} \quad (2.7)$$

$$\mathbf{D}(\omega) = \epsilon(\omega) \mathbf{E}(\omega) \quad (2.8)$$

ϵ_r is called the relative permittivity and is a macroscopic measure of the polarization inside a material in the presence of an external field. ϵ is defined as the relative permittivity times the vacuum value ($\epsilon \epsilon_0$).

The total current density can be divided into three parts:

$$\mathbf{J} = \mathbf{J}_{\text{free}} + \mathbf{J}_{\text{P}} + \mathbf{J}_{\text{mag}} = \mathbf{J}_{\text{free}} + \text{rot} \mathbf{M} \quad (2.9)$$

The three terms are the contributions of the free electrons currents \mathbf{J}_{free} , the polarization currents \mathbf{J}_{P} and the currents from the magnetization of the atoms themselves \mathbf{J}_{mag} .

Two types of electrons exist inside a material:

$$\rho = \rho_{\text{free}} + \rho_{\text{bound}} \quad (2.10)$$

Electrons which are bound to a specific atom ρ_{bound} and thus can not move freely through the material and free delocalized electrons ρ . The bound electrons determine the optical response of

insulators. While also present in metals, here the optical response is often mostly determined by the free electrons. The bound charges are moved from their equilibrium state and by that produce a polarization field.

$$\operatorname{div} \mathbf{P} = -\rho_{\text{bound}} \quad (2.11)$$

A uniform polarization inside a material cannot result in net charges because the polarization is just due to the separation of charges. However, with a non-uniform polarization or at material boundaries net charges can occur. By this the external electric field is reduced and part of its energy is stored in the polarization of the material. Applying an electric field to free charges, for example free electrons in a metal, leads to a flow of charges described by the current \mathbf{J}_{free} . The electrons can be described as free charges while their mass has to be adapted to an effective mass which is material dependent and gives credit to the background formed by the ion cores. Thus these charges have no restoring force by definition.

Wave equation To derive the wave equation in matter the following assumptions are made; no free charges are present, considering only the bound charges, an isotropic material and no magnetization, $\mathbf{M}=0$. Thus the only charges are the bound charges, equation 2.11, and the only current originates from the change of polarization.

$$\mathbf{J} = \frac{\partial \mathbf{P}}{\partial t} \quad (2.12)$$

Taking only this contribution into account a wave equation for the electric field inside a dielectric medium can be derived by taken the rotation of equation 2.2 for the electric field and inserting the material equations 2.3 and 2.4.

$$\Delta \mathbf{E} - \mu_0 \epsilon_0 \frac{\partial^2 \mathbf{E}}{\partial t^2} = \mu_0 \frac{\partial \mathbf{P}}{\partial t} \quad (2.13)$$

In vacuum no polarization is present and the right-hand side of the equation vanishes.

$$\epsilon_0 \mu_0 \frac{\partial^2 \mathbf{E}}{\partial t^2} - \Delta \mathbf{E} = 0 \quad (2.14)$$

A similar equation can be derived for the magnetic field \mathbf{B} . The important result from this equation is the plane wave solution $\mathbf{E} = \mathbf{E}_0 e^{i(\omega t - \mathbf{k} \cdot \mathbf{r})}$, with the angular frequency ω and the wavevector

k. The solution describes a wave which travels with the speed of light c :

$$c = \frac{1}{\sqrt{\mu_0 \epsilon_0}} \quad (2.15)$$

In the presence of a dielectric medium equation 2.13 has to be evaluated. The solution is assumed to have a harmonic field dependence with \mathbf{E} proportional to $\exp(i(\omega t - kz))$. In an isotropic material it is expected that the polarization field has the same dependence as the electric field, so that the time derivation on the right side becomes $-\omega^2 \mathbf{P}$ and the space derivation for the electric field $-\mathbf{k}^2$. If \mathbf{P} is set proportional to \mathbf{E} , according to equation 2.6 with the proportionality factor α the solution for the wave equation inside dielectrics is a plane wave with the following relation between \mathbf{k} and ω :

$$\mathbf{k}^2 = \frac{\omega^2}{c^2}(1 + \alpha) \quad (2.16)$$

The refractive index n is defined as the ratio between the phase velocity of a wave, $v_{\text{phase}} = \frac{\omega}{k}$, and the speed of light in vacuum $n = \frac{c}{v_{\text{ph}}}$. With this definition the root of the refractive index is $\sqrt{n} = 1 + \alpha$. Instead of using the polarization field equation 2.13 can be derived with the dielectric displacement 2.8. The result is a similar expression than 2.16 reading:

$$k^2 = \frac{\omega^2}{c^2} \epsilon_r^2 \quad (2.17)$$

From this comparison the relationship of the refractive index to the permittivity becomes $n = \sqrt{\epsilon_r}$. More general when also taking magnetic effects into account:

$$n = \sqrt{\mu_r \epsilon_r} \quad (2.18)$$

Both material parameters, the refractive index as well as the permittivity, fully describe the material response to the electro-magnetic field and can be converted into each other. The refractive index can be more intuitively in the context of propagating waves since its real part directly describes the reflection and the angle of refraction. In absorbing materials the refractive index becomes complex $\tilde{n} = n + i\kappa$. κ is called the extinction coefficient, which is directly proportional to the absorption coefficient a in the Lambert-Beer law $I = I_0 \exp(-ax)$, describing the intensity I attenuation of an electro-magnetic wave traveling through a medium of thickness x .

$$a = \frac{4\pi\lambda}{\kappa} \quad (2.19)$$

Here λ is the wavelength of light. The permittivity on the other hand is directly related to the complex conductivity σ by $\varepsilon = 1 + \frac{i\sigma}{\varepsilon_0\omega}$. The electrical conductivity is furthermore related to the penetration depth of an electro-magnetic wave into materials with free electrons, like metals. The excitation of free electrons results in a current which hinders the wave to propagate into the material,

$$\delta = \sqrt{\frac{2}{\omega\sigma}}. \quad (2.20)$$

The skin depth δ quantifies how far an electromagnetic wave is traveling into a material before its intensity is decreased to $1/e$ of its initial value. The material is assumed to have a permeability of 1. The skin depth shows e.g. that the interaction between a wave and a metallic particle is mainly determined by the material properties at the surface of the particle.

Boundary conditions From Maxwell's equations boundary conditions for the electric and magnetic field at the interface between two materials with different refractive indices can be derived. From the continuous condition of the tangential component of the electric field and the continuous condition of the normal component of the magnetic field the Fresnel formulas can be derived. These describe the reflection and transmission coefficients depending on the angle of incidence and the refractive indices of the two materials. Since the refractive index is wavelength dependent, in most cases the reflection and transmission of light at interfaces is as well. These formulas provide the fundamentals of any transmission and reflection calculations. The two independent linear polarization states of light are chosen to be p (parallel to the plane of incidence) and s (perpendicular to the plane of incidence). An important result from the Fresnel formulas is that light, which is linearly polarized in either s or p polarization, does not change its state of polarization upon reflection. For any other arbitrary polarization of the incoming beam the reflected beam normally shows an elliptical polarization where both the main axis of polarization as well as the degree of ellipticity has changed. This effect is the basis of ellipsometry measurement.

Polarization of light As light is a transverse wave, the electric field vector is oscillating in a plane perpendicular to the propagation direction. A light beam traveling in the z-direction can accordingly have components of the electric field in the x-y plane. Each linear polarization (LP) can be described by the superposition of x- and y- polarized light with different amplitudes. In elliptically polarized light the field vector rotates at a constant velocity in the x-y plane, where the tip forms an ellipse. Elliptically polarized light can be described by the superposition of

x- and y-polarized light with an additional phase difference. A different amplitude additionally rotates the main axis of the ellipse. Elliptically polarized light is classified into right and left handed, dependent on the rotation direction referred to the traveling direction. The special case of circularly polarized light is obtained with a phase difference of $\pi/4$ and the same amplitudes. Linearly polarized light may be described by two circularly polarized light (CPL) waves with opposite handedness and the same amplitude. The phase shift between left circularly polarized light (LCP) and right circularly polarized light (RCP) than defines the orientation of polarization. CPL can experimentally be obtained by a linear polarizer in combination with a quarter wave plate. A quarter wave plate is an optical component composed of two main axis with different refractive indices and a thickness which is chosen to imprint a phase difference of $\lambda/4$ onto the two perpendicular polarized fields.

Circular dichroism is defined as the difference in absorption between LCP and RCP light. Another quantity which is easier to access is the difference in transmission T, named the dissymmetry factor g which is defined as:

$$g = 2 \left(\frac{T^{LCP} - T^{RCP}}{T^{LCP} + T^{RCP}} \right) \quad (2.21)$$

To determine the absorption both the transmission and the reflection has to be measured, while in the latter case the quantification solely relies on the transmission spectrum.

Electrodynamic description of dissymmetry In electrodynamic theory the different transmission of LCP light and RCP light is described as a cross-coupling between electric and magnet fields propagating in the same direction [17]. The Maxwell's equations have to be rewritten as follows:

$$\begin{pmatrix} \mathbf{D} \\ \mathbf{B} \end{pmatrix} = \begin{pmatrix} \epsilon_0 \epsilon_r & \frac{-i\chi}{c} \\ \frac{i\chi}{c} & \mu_0 \mu_r \end{pmatrix} \begin{pmatrix} \mathbf{E} \\ \mathbf{H} \end{pmatrix} \quad (2.22)$$

The introduced chirality factor χ is a measure for the coupling between the electric and magnetic fields. Calculating the refractive index leads to the following expression:

$$n_{\pm} = \sqrt{\epsilon\mu} \pm \chi \quad (2.23)$$

The plus and minus sign stands for the left and right circularly polarized light. From equation 2.23 it follows that even for positive permeability and permittivity, the refractive index can be negative for a large χ value.

2.2 Permittivity models

electron charge	e	plasma frequency	$\omega_p = \frac{N_{\text{free}} e^2}{m_{\text{free}} \epsilon_0}$
effective electron mass	m	(derived parameter)	
electron density	N	oscillator strength	$f_b = \frac{N_{\text{bound}} e^2}{m_{\text{bound}} \epsilon_0}$
damping coefficient	γ	(derived parameter)	
resonant frequency	ω_0		

Table 2.1: Parameter used for the Drude-Lorentz model of the permittivity.

Drude model A simple analytic model to describe the permittivity of a material is the Drude-Lorentz model. This model considers two different origins of the electromagnetic response; bound and free electrons. The free electrons are e.g. the conduction electrons of a metal or a highly doped semiconductor. The bound electrons are fixed to an atom and cannot move freely through the material. Nevertheless in the presence of an electric field the electrons are deflected from their equilibrium positions leading to a polarization field inside the material which weakens the incident field. In the Drude-Lorentz model the equation of motion of electrons is the starting point to derive an expression of the permittivity.

$$\ddot{\mathbf{r}} + \gamma \dot{\mathbf{r}} + \omega_0^2 \mathbf{r} = \frac{e}{m_e} \mathbf{E} \quad (2.24)$$

m_e is the electron mass, e is the electron charge, γ is the damping coefficient and ω_0 the eigenfrequency of the bound electrons. The mass of the electrons is the effective optical electron mass, influenced by the bonding state of the electron. The parameter γ describes the damping of the electron. In textbooks for mechanics the damping term is often described by the velocity times a damping coefficient without the particle mass. In the case of electrons inside a material, the damping is influenced by the crystal structure. To include this the effective mass has to be used. ω_0 is the eigenfrequency of bound electrons and describes their restoring force. The electric field describes the external electric field as the driving force of the electrons. Its assumed to have a harmonic time dependence. Without any external stimuli the electric field is just due to the electrons themselves if they are out of their equilibrium positions.

The solution of equation 2.24, in the case of an linearly polarized electric field is

$$x = \frac{e}{m} \frac{1}{(\omega_0^2 - \omega^2) - j\omega\gamma} \mathbf{E}. \quad (2.25)$$

The induced dipole moment \mathbf{P} , is given by the electron density N multiplied by the electron

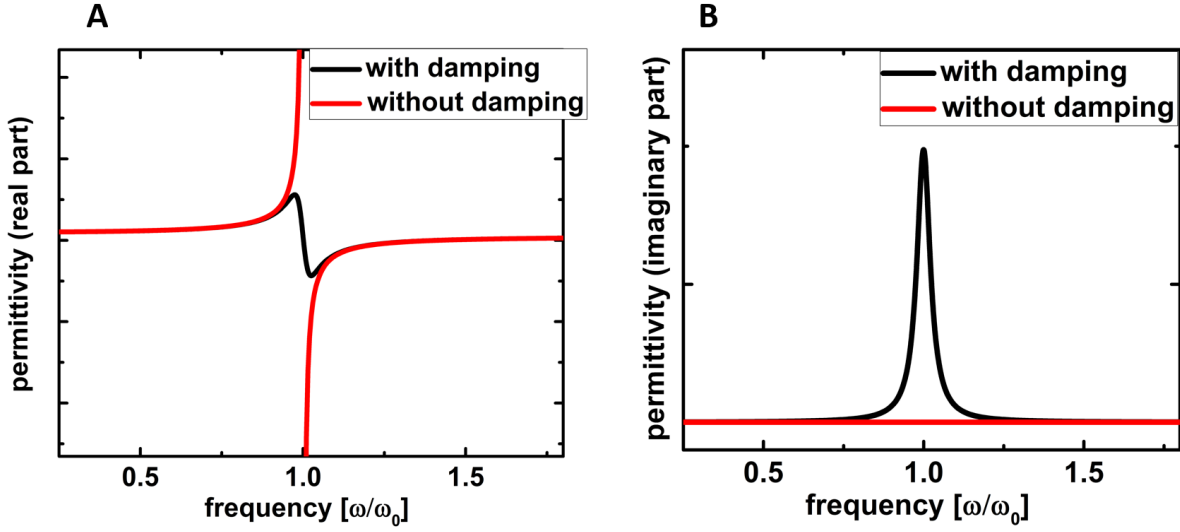


Figure 2.1: A) Real part of the permittivity from the Drude-Lorentz model around the electronic transition centered at ω_0 . B) Imaginary part of the permittivity for the same case as in A.

charge e and the deflection x , out of their initial position:

$$\mathbf{P} = Nex, \quad (2.26)$$

$$\mathbf{D} = \epsilon_0 \mathbf{E} + \mathbf{P} = \epsilon_0 \epsilon_r \mathbf{E}, \quad (2.27)$$

By inserting the electron displacement into the definition of the dielectric displacement \mathbf{D} , it follows for the permittivity:

$$\epsilon = \epsilon_0 \left[1 + \frac{f_b}{(\omega_0^2 - \omega^2) - j\gamma\omega} \right] \quad (2.28)$$

$f_b = \frac{Ne^2}{m\epsilon_0}$ is the oscillator strength. To describe the permittivity of real materials often more than one oscillator is needed. The permittivity is then a summation over all transitions.

$$\epsilon = \sum_{j=1}^{N_{osc}} \left(\frac{f_j}{\omega_j^2 - \omega^2 - i\gamma_j\omega} \right) \quad (2.29)$$

The oscillator model can also be used to describe other resonances in the material as e.g. phonon resonances. The general behavior of a single oscillator is shown in figure 2.1 for the real part A and the imaginary part B, respectively. A damping term is needed to avoid an infinite value for the real part of the permittivity.

For a metal with free electrons the equation of motion 2.24 is adapted in the following way: Since no restoring force is present ω_0 is set to zero. The mass describes the effective optical mass of the free electrons. The damping term γ describes the damping of free electrons e.g. by collisions with the crystal lattice. It has to be further adopted for material dimensions below 10 nm in any direction. In that case an additional loss channel gains importance since all electrons start to 'feel' the border of the material. The collisions of the electrons with the material border can be considered in modifying the damping term γ in the following way:

$$\gamma = \gamma_{bulk} + A \frac{r}{v_F} \quad (2.30)$$

γ_{bulk} is the value as it was introduced before for the bulk material, A is a constant which depends on the actual shape of the particle or surface, r is the radius of the particle and v_F is the Fermi velocity of electrons. The formula for the permittivity due to free electrons is

$$\varepsilon_r = 1 - \frac{\omega_p^2}{\omega^2 + \gamma^2} \quad \varepsilon_i = \frac{\omega_p^2 \gamma}{\omega^3 + \omega \gamma^2}. \quad (2.31)$$

Without damping it further simplifies to

$$\varepsilon_r = 1 - \frac{\omega_p^2}{\omega^2} \quad \varepsilon_i = 0. \quad (2.32)$$

ω_p is the plasma frequency of the metal. Electron damping gives rise to a complex permittivity as well as to a decrease of the absolute value of the real part of the permittivity, figure 2.2. For increasing damping the negative value of the real part is lowered. If $\omega \ll \omega_p$ the second term can be neglected which the real part of the permittivity results in a constant value of 1. To account for the constant polarization field present in a lot of metals, often the 1 is replaced by ε_∞ , with values usually between 1 and 10. The imaginary part is zero when the damping coefficient is zero, thus it describes the absorption of the material. The imaginary part shows a continuous decrease with increasing frequency. The plasma frequency determines the response of the free electron gas. For example the border between negative and positive values of the permittivity for $\omega < \omega_p$ or $\omega > \omega_p$ respectively. To illustrate the physical meaning of the plasma frequency the electric field from equation 2.24 is assumed to be caused by density fluctuations of the electron cloud itself. A difference in the electron density leads to an electric field and thus to a driving force towards the equilibrium state. The force is proportional to the displacement of the electrons with respect to their equilibrium positions. The change in electron density at any given point can be written as $\Delta N = N_0 e \frac{dr}{dx}$ where N_0 is the electron density at equilibrium condition and ds/dx describes the volume change (or in the one dimensional case the distant change) the electrons

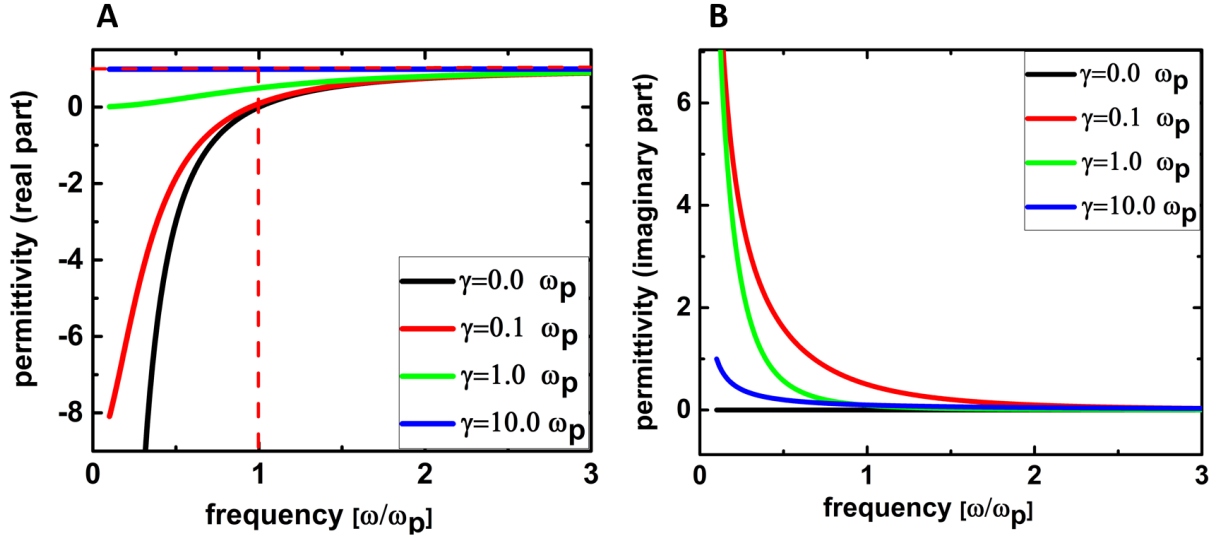


Figure 2.2: A) Real part of the permittivity for a metal according to the Drude-Lorentz model, plotted for different damping coefficients relative to the plasma frequency. B) Imaginary part of the permittivity for the same values as in A.

occupy. With the first Maxwell equation, $\text{div}(\mathbf{E}) = \frac{\Delta N}{\epsilon_0}$, and the definition of the electric field as the force per unit charge $\mathbf{E} = \mathbf{F}/e$, it follows for the force acting on the electrons:

$$|\mathbf{F}| = \frac{N_0 e^2}{\epsilon_0} x \quad (2.33)$$

The force on the electrons is proportional to their initial density multiplied by the deflection of the electrons. Putting this force into the equation of motion 2.25 results into an oscillation with the frequency ω_p . This leads to the conclusion that the plasma frequency is the frequency of electrons oscillating in their own electric field. Table 2.2 lists the measured electron densities

metal	free electron density [$\frac{1}{m^3}$] [18]	plasma frequency [eV] [19]
Cu	8.47	10.83
Au	5.90	9.03
Ag	5.86	9.01

Table 2.2: Electron density and plasma frequency of three common noble metals Cu, Ag, Au.

and plasma frequencies of three common noble metals. As expected, the plasma frequencies follow the same trend as the free electron densities, supporting this simple theory. In figure 2.3 the permittivity of gold obtained from the Drude-Lorentz model with the parameters obtained from [19] compared to the measured values from Johnson and Christy [20] for the real and

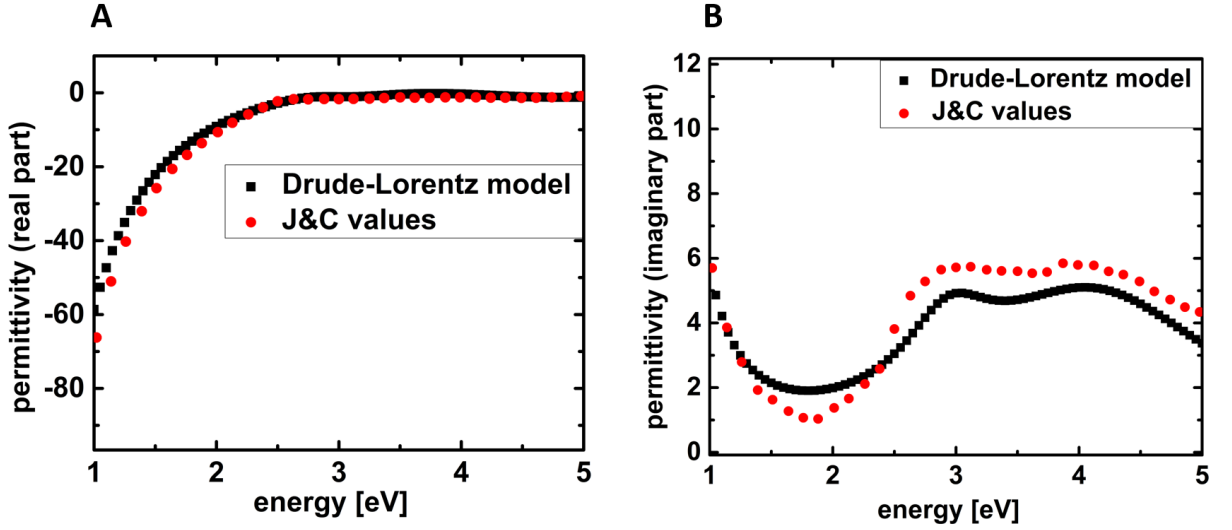


Figure 2.3: A) Real part of the permittivity of gold plotted by the Drude-Lorentz model with the parameters from [19], compared to the measured values from [20]. B) Imaginary part of the permittivity for the same values as in A.

imaginary part in A and B, respectively, are plotted. Five oscillators with different strength are used to fit the model to the dielectric function attribution to the interband transitions in gold. The measured real part is very well resembled by the model. The shape of the imaginary part can be resembled with five oscillators, while the remaining discrepancy could be reduced by adding further oscillators. Even though the plasma frequency describes the collective oscillations of the electrons in a metal and explains why a metal becomes semi-transparent for energies above the plasma frequency, the color appearance, in the case of common noble metals like silver, gold, or copper is due to the position of the interband transitions. For the case of gold and copper these are located in the visible spectrum giving both metals its shiny gold and reddish appearance. For silver the interband transitions starts in the UV region, resulting in almost perfect reflectance in the whole visible range.

Description of mixed materials In the above paragraph the permittivity of a material has been characterized by its bound electrons, described by Lorentz-oscillators and contributions of the free electrons. These describe a material of one phase. In cases of an inhomogeneous material which consists of two or more phases in their own morphology, effective medium theory is applied to determine the permittivity. The average distance of the two phases has to be below the wavelength of the interacting light. As this is often the case in EBID materials from organo-metallic precursors where metal inclusion are embedded in an amorphous carbon matrix. In this respect it is expected that the resulting material responses is described based on the original

permittivities of the primary materials. Mixture in the form of $\epsilon_{\text{eff}} = f\epsilon_1 + (1 - f)\epsilon_2$, where f is the volume filling fraction of material one, ϵ_1 and ϵ_2 are the permittivities of the first and second component respectively and ϵ_{eff} the effective permittivity of the composition, is expected to give a rather poor estimation of the material. As seen before, the material responds to the incident field by an induced polarization which in return will influence the surrounding material.

Instead, a model can be used which takes the interaction through material polarization into account. To describe the optical properties of a heterogeneous material in terms of its components. The most common effective medium theories are; the Maxwell-Garnett (MG) theory and the Bruggeman theory [21]. The derivation of both theories starts with the local electric field inside a dielectric material. When an electric field \mathbf{E} is applied to a dielectric material the local field $\mathbf{E}_{\text{local}}$ acting on the individual atoms is given by:

$$\mathbf{E}_{\text{local}} = \mathbf{E} + \frac{4\pi\mathbf{P}}{3\epsilon_0} = \epsilon_r\mathbf{E}_{\text{avg}} \quad (2.34)$$

The polarization \mathbf{P} of a material with the polarizability α where N_A is the unit volume density of atoms polarized in the electric field is given by:

$$\mathbf{P} = N_A\alpha\epsilon_0\mathbf{E}_{\text{local}} \quad (2.35)$$

Limited to the case of linear relation between the electric field and polarization field. Inserting the local electric field from equation 2.34 into the formula 2.35 the following expression for the polarization is obtained:

$$\mathbf{P} = \frac{N_A\alpha}{1 - \left(\frac{4}{3}N_A\alpha\pi\epsilon_0\right)}\epsilon_0\mathbf{E} \quad (2.36)$$

This equation shows that the polarization is still proportional to the electric field but instead of the simple form of equation 2.6 another term has to be considered. Thus the permittivity in this case is not $1+\alpha$ but instead $1 + \frac{N_A\alpha}{1 - \left(\frac{4}{3}N_A\alpha\pi\epsilon_0\right)}$, or rewritten:

$$\frac{3}{4\pi\epsilon_0} \frac{\epsilon - 1}{\epsilon + 2} = N_A\alpha \quad (2.37)$$

This formula is known as the Clausius-Mossotti equation and it relates the permittivity of a material with the polarizability of its constituents. In the case of two materials the summation should be performed over the polarizabilities of the two materials instead of their permittivities.

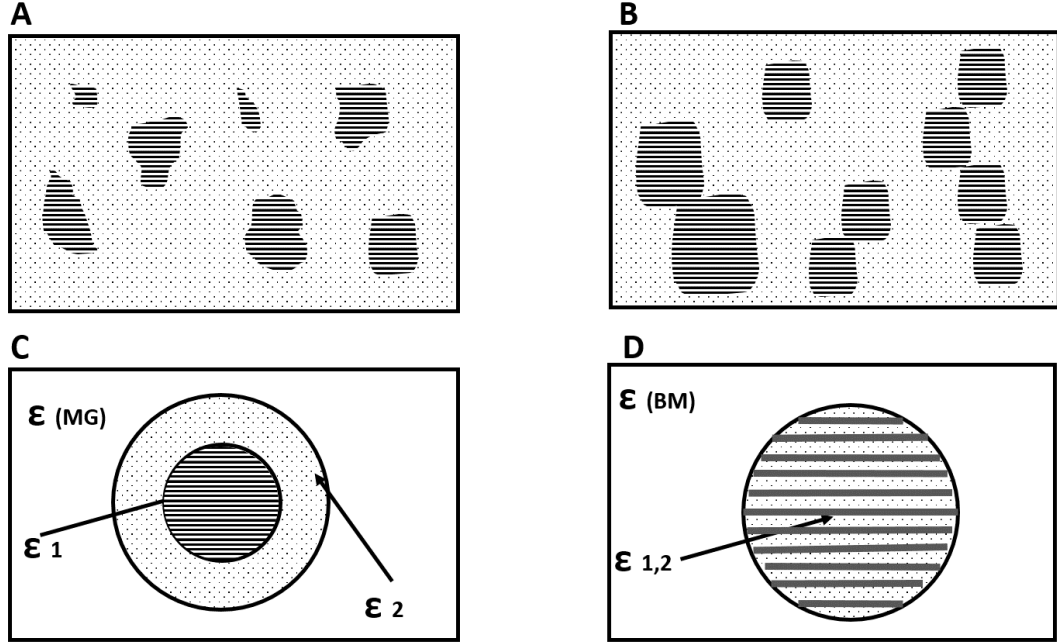


Figure 2.4: A, C) Microstructure and model of the material according to the Maxwell-Garnett theory. The radii are determined by the filling fraction of both materials. B, D) Microstructure and model according to the Bruggeman theory, both adapted from [24].

If rewriting the single phases with the relation given by 2.37 the following formula is derived:

$$\frac{\epsilon_{\text{eff}} - 1}{\epsilon_{\text{eff}} + 2} = N_1 \frac{4\pi}{3} \epsilon_0 \alpha_1 + N_2 \frac{4\pi}{3} \epsilon_0 \alpha_2 = f_1 \frac{\epsilon_1 - 1}{\epsilon_1 + 2} + f_2 \frac{\epsilon_2 - 1}{\epsilon_2 + 2} \quad (2.38)$$

By the volume average of a sphere with the boundary condition that the sum of the volume fraction of all phases is 1, the atomic density N_A can be replaced by the volume fraction f of the i -th phase. So far it has been assumed that the particles are placed in vacuum. The next step is to include a background medium in which the particles are embedded. It has been shown that with such a background material equation 2.38 keeps its form, but replacing $\epsilon \rightarrow \epsilon/\epsilon_b$ and the permittivity of the inclusions by $\epsilon_i \rightarrow \epsilon_i/\epsilon_b$ [22]. This yields a general expression of the dielectric function [23].

$$\frac{\epsilon_{\text{eff}} - \epsilon_b}{\epsilon_{\text{eff}} + 2\epsilon_b} = f_1 \frac{\epsilon_1 - \epsilon_b}{\epsilon_1 + 2\epsilon_b} + f_2 \frac{\epsilon_2 - \epsilon_b}{\epsilon_2 + 2\epsilon_b} \quad (2.39)$$

Equation 2.39 is of a general form and connects the effective permittivity of a material with the permittivities of its components and their volume fraction. In the Maxwell-Garnett theory, considering a mixture of two phases, one phase is set to be the background medium. Thus one

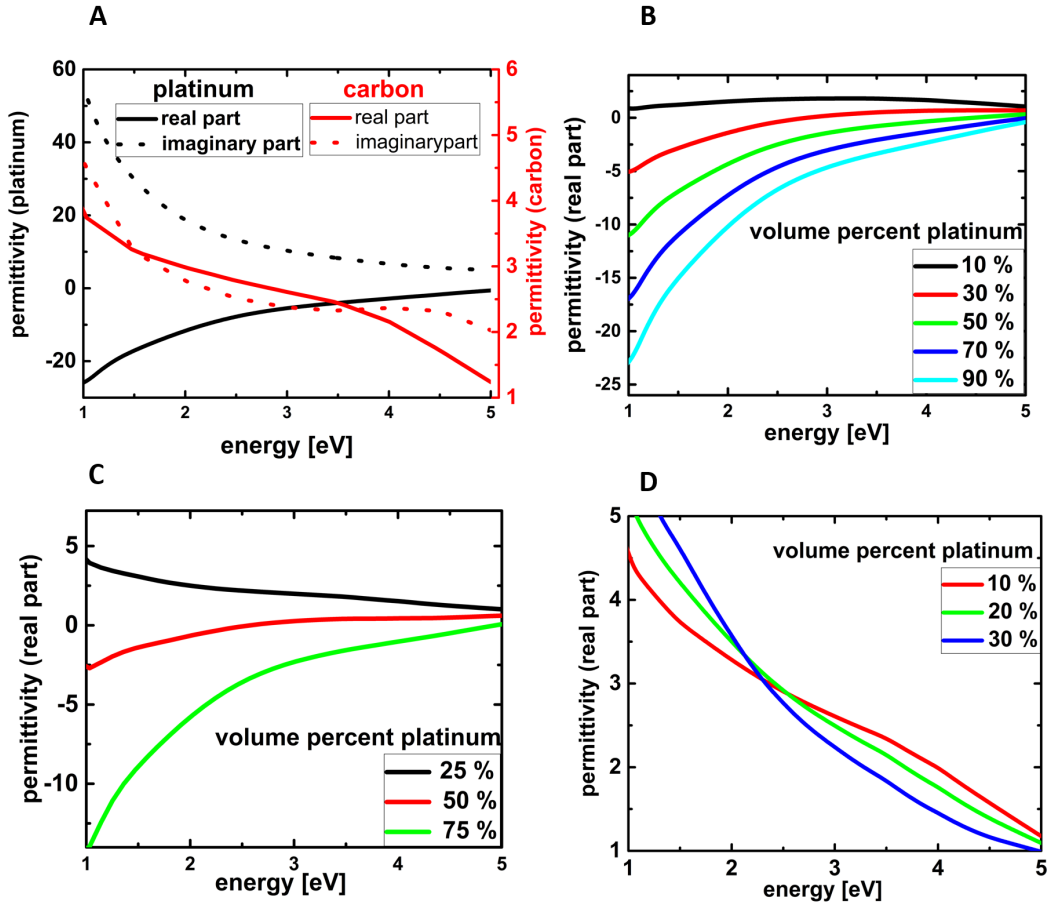


Figure 2.5: A) Permittivity of carbon and platinum used for different mixing models. B) Average with respect to the volume fraction. C) Bruggeman model for three different volume fractions. Maxwell-Garnett model with three different volume fractions.

term on the right side equals zero. The formula can be solved for the effective permittivity as follows [24]:

$$\epsilon_{MG} = \epsilon_b \frac{\epsilon_1 + 2\epsilon_b + 2f(\epsilon_1 - \epsilon_b)}{\epsilon_1 + 2\epsilon_b - 2f(\epsilon_1 - \epsilon_b)} \quad (2.40)$$

Another interpretation is that both inclusions are in an imaginary background medium which is the effective medium itself. In that case the left side of the equation becomes zero. The effective permittivity, referred to as Bruggeman-formula is

$$\epsilon_{BG} = \frac{b + \sqrt{8\epsilon_1\epsilon_2 + b^2}}{4}, b = (2f_1 - f_2) + (2f_2 - f_1)\epsilon_2. \quad (2.41)$$

The different material structures associated with the Bruggeman (BG) or Maxwell-Garnett (MG)

model are depicted in figure 2.4, A,C for the MG and B,D for the BG case respectively. In the MG structure each inclusion is surrounded by the background material. Thus, the volume fraction is given by the ratios of the two circles in figure 2.4 C, while in the case of BM both phases are randomly mixed with each other and the volume filling factor f is given by the probability to encounter phase 1 or 2 [23]. The BG formula is symmetric in terms of the two permittivities. In contrast in the MG approach the effective permittivity changes, depending on the choice of the background medium. While in the case of a very low volume fraction of one phase the choice for the background medium might be obvious, if both components occupy similar volumes, the decision might be ambiguous. Figure 2.5 B,C and D shows the real part of the permittivity of a mixed material consisting of platinum and carbon calculated with different models. The used permittivity values are shown in figure 2.5 A. In figure 2.5 B the permittivity of the mixed material is an average of the two permittivities with respect to the volume fraction $\epsilon = f_1 \epsilon_{Pt}(1 - f) \epsilon_C$. In figure 2.5 C the permittivity is calculated with the BM formula 2.41. The curves look similar to the average model, however other values are obtained for the same volume fraction. Figure 2.5 D shows the permittivity calculated with the Maxwell-Garnett model, with carbon material as background and platinum as inclusions. The plot differs a lot from the other two models. As expected after the summation over dipole polarizabilities the values of the real part of the permittivity is positive over the whole energy range. An effective medium in the Maxwell-Garnett model is dielectric.

2.3 Scattering: From classical scatterer to plasmonics

Rayleigh scattering Scattering is a universal physical phenomenon important in many fields. Scattering is the redirection of light when interacting with any object [25]. One of the first scattering processes that have been investigated was the scattering of light by small particles[26]. The incident light induces polarization and charge oscillations which result in the emission of light. Scattering is named elastic when the frequency of light not change during the scattering process. In the case where the photon energy, hence the frequency, of the light changes, the process is categorized as inelastic scattering. The elastic scattering process of light with small particles is described by the Rayleigh theory. The theory is valid in the small size limit where the wavelength of the incident light is much larger than the particle size. This criterion is often defined using the dimensionless parameter $\beta = \frac{2\pi nr}{\lambda}$, where r is the radius of the spherical particle, λ the wavelength of the incident light and n is the refractive index of the medium

surrounding the particle. The criterion can then be expressed as [25]:

$$\beta \ll 1. \quad (2.42)$$

In the derivation of the Rayleigh scattering cross-section of a spherical particle the assumption is made that the polarization induced by the incident light is uniform throughout the sphere.

$$\mathbf{P} = \mathbf{P}_0 \frac{4\pi r^3}{3} \quad \mathbf{P}_0 = 3\varepsilon_0 \frac{\varepsilon - 1}{\varepsilon + 2} \mathbf{E} \quad (2.43)$$

\mathbf{P} is the dipole field of the sphere with the magnitude \mathbf{P}_0 [26]. The total Rayleigh cross-section is obtained by calculating the Poynting vector for the light radiated by the dipole, while averaging over the two polarization states and all solid angles. The Poynting vector is proportional to $P^2 \lambda^{-4}$. The total cross-section for the Rayleigh scattering C_{Ry} , taken from reference [27] is

$$C_{Ry} = \frac{8\pi\varepsilon_b^2}{3} \left(\frac{2\pi}{\lambda} \right)^4 r^6 \left(\frac{\varepsilon - \varepsilon_b}{\varepsilon + 2\varepsilon_b} \right)^2. \quad (2.44)$$

Here, the refractive index is transformed to the permittivity with ε_b as the permittivity of the background. One important property of the scattering cross-section is the λ^{-4} dependence, explaining the well-known example of the blue color of the sky by scattering of light by dust particles. For this case a constant dielectric function of dust particles is assumed. However, when accessing metal particles and their scattering properties in the visible spectral range, it has to be considered that the dielectric function is not constant. While the term depending on λ does continuously decrease with increasing wavelength, the last term in brackets becomes maximal when the denominator fulfills the condition:

$$\Re(\varepsilon) = -2\varepsilon_b. \quad (2.45)$$

2.45 is called Fröhlich condition [14]. Assuming the dielectric function of a perfect metal without any damping 2.32, the frequency of the dipole resonance is at

$$\omega_r = \frac{\omega_p}{\sqrt{3}}. \quad (2.46)$$

Equation 2.46 shows that the plasma frequency of the metal determines the position of the dipole resonance. For noble metals the plasma frequencies are around 10 eV which would result in a resonance in the ultra-violet region. Thus it is necessary to include the damping coefficient γ . The damping shifts the frequency where the real part of the permittivity equals -2 to significantly

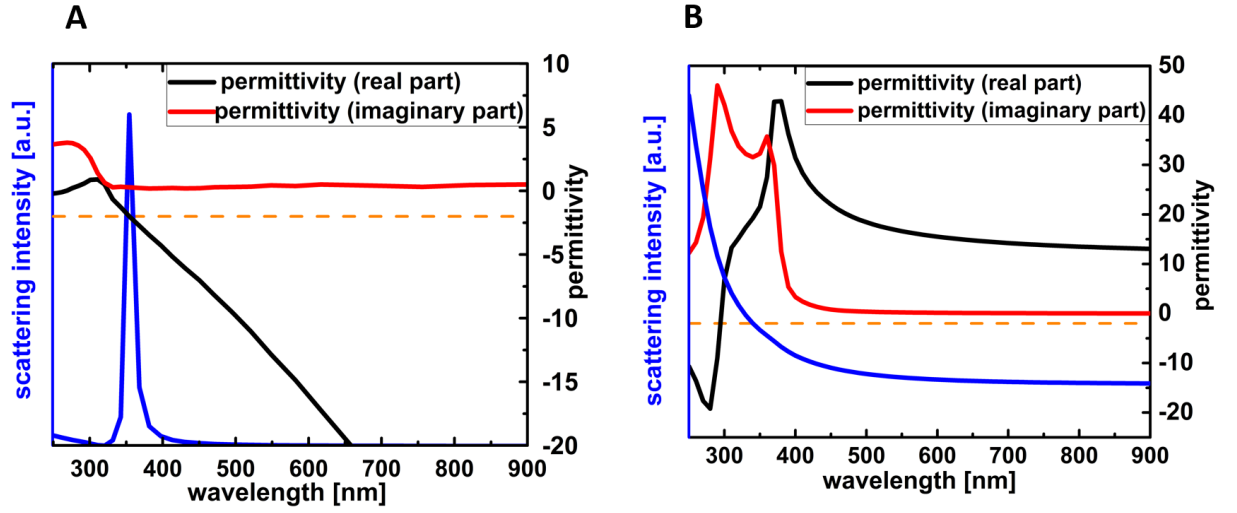


Figure 2.6: The complex permittivity and the Rayleigh scattering cross-section calculated by equation 2.44 for silver A) and silicon B). Both materials exhibit a position where the real part is -2 (orange line), but just in the case of silver a strong resonance occurs because of the low imaginary part compared to silicon.

lower energies.

$$\omega_r(\varepsilon = -2) = \sqrt{\frac{\omega_p^2}{3} - \gamma^2} \quad (2.47)$$

Figure 2.6 shows the complex permittivity and scattering cross-section of a silver A) and a silicon B) sphere with a radius of 30 nm in vacuum, representative for a noble metal and a semiconductor. While the dielectric function is complex the real part of equation 2.44 has to be used [14]. Silver exhibits a strong resonance around 350 nm. Even though silicon fulfills the Fröhlich condition around 350 nm, the imaginary part and thus the absorption are too high to exhibit a resonance at this wavelength.

Mie scattering The full analytic solution of a plane wave scattered by a spherical particle was developed by Gustav Mie in 1904 [11] and is referred to as Mie theory. While the original work was about a sphere consisting of a homogenous material it was later extended to different shapes and to the case of coatings (core-shell particle) [28]. The scattering problem of a sphere has to be solved by identifying a solution for Maxwell’s equations inside and outside the sphere while satisfying the boundary conditions. On the surface of the sphere the tangential part of the electric field and normal part of the magnetic field have to change continuously. The total field outside the sphere $\mathbf{E}_{\text{out}}, \mathbf{H}_{\text{out}}$ is a superposition of the incident field $\mathbf{E}_{\text{in}}, \mathbf{H}_{\text{in}}$ with the scattered field

$\mathbf{E}_{sc}, \mathbf{H}_{sc}$. The intensity, described by the pointing vector \mathbf{S} outside the sphere has three different contributions: the incoming field \mathbf{S}_{in} , the scattered field \mathbf{S}_{sc} and a mixed term \mathbf{S}_{ext} , which arises from the interaction between the two.

$$\mathbf{S} = \mathbf{E}_{out} \times \mathbf{H}_{out} = \mathbf{S}_{in} + \mathbf{S}_{sc} + \mathbf{S}_{ext} \quad (2.48)$$

The integration of the intensities over the surface of the sphere A , containing the scatterer, gives the energy rate W

$$W_{in,sc,ex} = e \int_A \mathbf{r} \mathbf{S}_{in,sc,ex} dA. \quad (2.49)$$

The total energy rate W_{abs} , corresponding to \mathbf{S} from 2.48, is then expressed as:

$$W_{abs} = W_{in} - W_{sc} + W_{ext}. \quad (2.50)$$

The signs are usually chosen such that the energy rate absorbed inside the integration area W_{abs} and the energy rate scattered outwards W_{sc} are both positive. In the case of a non-absorbing medium around the scatterer, the energy rate through a closed surface from the incident beam is zero $W_{in} = 0$. The energy extinction rate of the scatterer is therefore the sum of energy absorption and scattering rate. Often the energy rates W are normalized either to the incoming intensity I_{in} , or to the incoming intensity and the geometrical shadow of the scatterer G .

$$C_{sc,ex} = \frac{W_{sc,ex}}{I_{in}} \quad (2.51)$$

$$Q_{sc,ex} = \frac{W_{sc,ex}}{GI_{in}} \quad (2.52)$$

The cross-section C has the unit cm^{-2} . The scattering and extinction efficiency Q is a dimensionless parameter. In geometrical optics the maximum value of Q equals one since incident rays can be either absorbed or deflected. However, plasmonic particles can exhibit significantly higher values. To find concrete solutions for C and G , the electromagnetic fields are expressed by vector harmonic functions. C and G can then be expressed by an infinite series [29]. A variety of numerical implementations exist, to calculate the Mie cross-sections of spherical particles. The code used in this thesis is MiePlot [30].

Plasmons The reason for the high scattering cross-section of small metal particles, as seen in figure 2.7, is the collective excitation of free electrons by the incident electromagnetic field. This collective oscillations arise at discrete energies and are called a localized surface plasmon

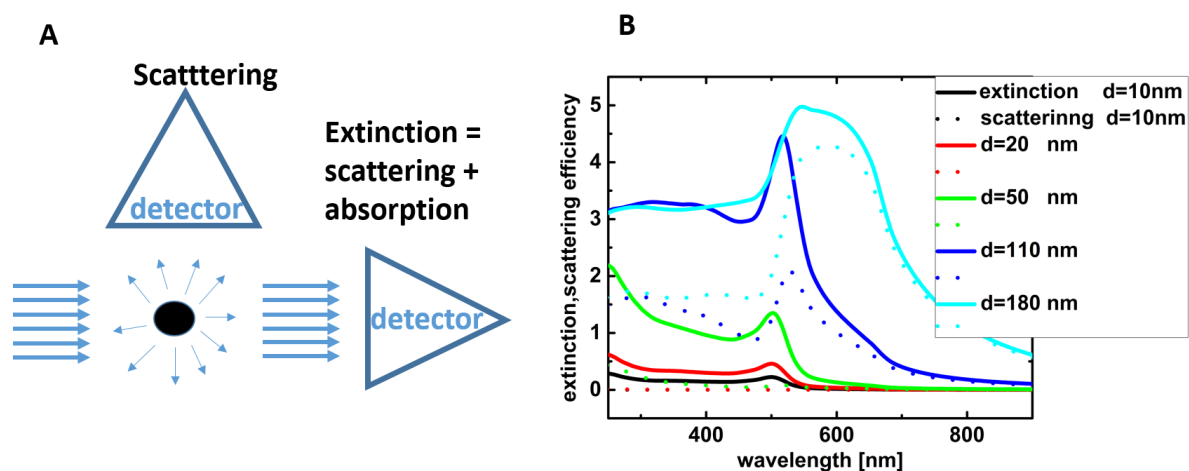


Figure 2.7: A) Dependence of the detector (triangles) position on the measured quantity. B) Scattering and extinction cross-section of a gold sphere with varying diameter from 10 - 130 nm, shows the wavelengths shift and increase broadening of the resonance with increasing size. Calculation are done according to Mie theory [31] with the material parameter of gold from [20].

polariton (sometimes just referred to as localized surface plasmon). In general, a plasmon describes the quantized oscillations of free electrons. A polariton is a coupled state between a fundamental excitation like a plasmon (or a phonon) and an electro-magnetic wave. Such coupling was first proposed in solid state physics for the coupling between phonon and photons [32]. Plasmons also exist as volume plasmons in bulk metals, for frequencies higher than the plasma frequency. The frequency of the dipole plasmon of a small metal particles is, according to the Drude-Lorentz model, at $\omega_p/\sqrt{3}$ (equation 2.46). For larger particles higher order multipoles start to contribute to the plasmonic response. Figure 2.7 A shows a sketch of the two mechanism of light interacting with a particle, scattering and absorption. The figure depicts the dependence of the detector position on the quantity measured. In the light path the sum of scattering and absorption is measured, called extinction. Out of the light path, just the scattered portion can be detected. Figure 2.7 B shows the scattering and extinction cross-sections for gold spheres with different diameters, calculated by Mie theory [30]. There are three important observations from the graph. First, the scattering and extinction increase with increasing particle size. Second, the scattering increases faster than the extinction, which means that the resonance of very small particles is mainly absorptive while for larger particle the scattering is dominant. Third, the position of the resonance shifts towards larger wavelengths for larger particles, which is different for the quasistatic limit, where the position of the resonance is determined by the values of the permittivity only. So far the results are valid for spherical particles. The solution from Mie theory relies on rotational symmetry of the boundary conditions. A change of the geometrical shape of the

scattering object thus leads to a change of the plasmon resonances. The resonance position of gold and silver particles significantly change when changing their geometrical form. Herewith, the resonant behavior can be tuned over a broad spectral range [14].

2.4 Optical measurements

Darkfield scattering measurement There are different experimental setups for measuring the scattering cross-section of plasmonic particles. Darkfield microscopy is a very convenient and popular method [33]. In a darkfield setup the sample is illuminated under high angles. The objective is only collecting light under a lower angle, thus only scattered light is detected. In the case of a single planar surface, no light enters the objective and the picture is dark [34]. The spectra in this thesis are recorded with a Zeiss Axio Imager optical microscope under dark field configuration. All samples are illuminated with unpolarized light of a halogen lamp through a 100x objective with a numerical aperture of 0.75. The scattered light is collected with the same objective and out-coupled through a 400 μm optical fiber to a Horiba iHR 320 spectrometer. By use of the fiber light is collected from a 1 μm spot. The experimentally detected signal is proportional to the scattering efficiency of the structure and the light intensity of the source [35]. The recorded spectra have to be normalized to the intensity of the light source and corrected by the background, measured away from the structure. The source spectrum is measured with a highly reflective silver coated mirror.

Reflection and transmission measurements A great advantage of ellipsometry is its high accuracy because only the change of polarization is measured. However, in this thesis for the case of EBID material, the deposited areas are rather small. While a common ellipsometer has a spot size of several micrometers an optical microscope provides a rather easy way to focus light to 1 μm . A length scale which is accessible with EBID fabrication in a reasonable time. Transmission and reflection measurements are done with the optical microscope Zeiss Axio imager. For normalization purpose the intensity spectrum of the light source for transmission is directly measured. The fiber is placed in the middle of the deposit such that any scattering from the edges of the pad can be neglected.

Measurement of circular dichroism The dissymmetry transmission signal is measured with the same optical microscope as the scattering and transmission/reflection measurements. Additionally, in the transmission configuration a condenser with polarizing maintaining properties is

used. After a linear polarizer a lambda /4 wave plate is placed into the beam patch. The lambda /4 plate can be turned by 180 degree to obtain both circular polarizations.

Brute force algorithm The Fresnel coefficients for reflection and transmission both depend on the index of refraction of the material. For a single material an analytic expression for the reflection and transmission can be given. For an absorbing material the reflection R becomes:

$$R = \frac{(n - 1)^2 - \kappa^2}{(n + 1)^2 - \kappa^2} \quad (2.53)$$

The formula can be used for the case where the material is thick enough thus no reflection from the backside of the material has to be taken into account. This is easy achievable for example for a metallic surface which has a high reflectivity and thus a very small penetration depth of the field. Only a single quantity is measured by reflection, while two parameters have to be determined. Without any additional information this results in a range of possible n , κ values. In the case of thin or transparent materials a model of the layer stack has to be build, the same way as for the ellipsometry measurement. Due to the sub-wavelength thickness of the EBID and ITO layers, light within these layers is treated as coherent while the glass substrate is treated as semi-coherent [36]. To find the solution for the n and κ values a brute force approach is used. Within a specified range of n and κ values the transmission and reflection is calculated for every given combination and compared to the measured data. Within the brute force algorithm every layer is represented by a matrix as is every interface between two different materials. The transmission/reflection can then be represented by this matrices (transfer matrix method). In this thesis the limit of difference between measured and calculated transmission and reflection values is set to be below 10^{-9} to accept the solution.

Ellipsometry The working principle of an ellipsometer is taken from reference [37]. In ellipsometry measurements a complex reflection coefficient ξ is defined, as the ratio of the reflection coefficients for the p and s polarized states $\xi = \frac{r_p}{r_s}$. The ratio is usually defined by a real and imaginary part in the following way:

$$\xi = \frac{|r_p| \exp(i\delta_p)}{|r_s| \exp(i\delta_s)} = \tan \Psi \exp(i\Delta) \quad (2.54)$$

Where $\tan(\psi) = \frac{|r_p|}{|r_s|}$ and $\Delta = \delta_p - \delta_s$. These equations are relating the measurable parameters ψ and Δ to the material properties. In the simplest case only a single reflection at a planar interface between a material and air occurs. For this case the dielectric function can be calculated by an

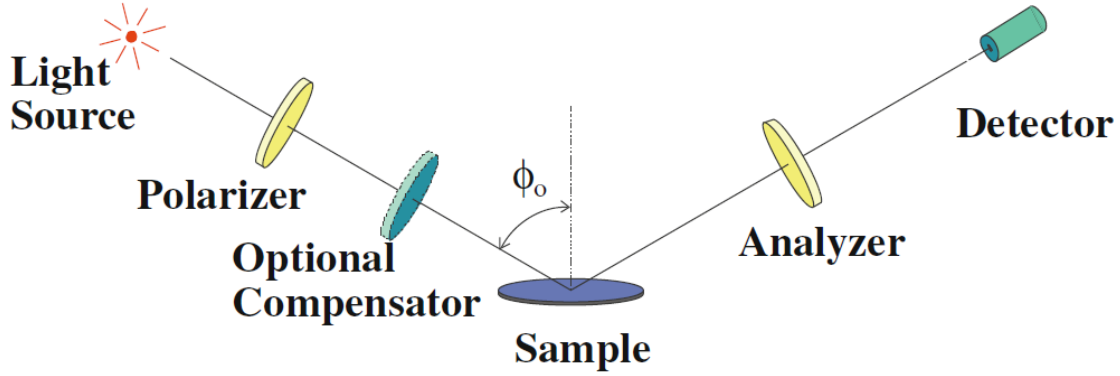


Figure 2.8: The basic components of an ellipsometer are the light source, polarizer, optical compensator, analyzer and detector [37].

analytic formula:

$$\varepsilon_r = \sin^2(\phi_0) + \sin^2(\phi_0) \tan^2(\phi) \left[\frac{1 - \xi}{1 + \xi} \right]^2 \quad (2.55)$$

With ϕ_0 the incident angle of light. Here, the parameters ψ and Δ are measured. ξ is calculated with 2.54 from which the permittivity can be directly deduced. In most cases, however, the layer stack consists of one or multiple thin layers on top of a substrate. In this case the measured values would give an effective or often called pseudoelectric dielectric function. The multiple reflection occurring between the interfaces have to be taken into account thus the measured values additionally depend on the thicknesses of the layers. A model has to be build with the input parameters being the permittivities and thicknesses of all layers, except the one being investigated. By numerical algorithms the measured values has to be fitted to the model for the unknown layer.

Figure 2.8 shows the basic components of an ellipsometer consisting of a light source, polarizer, compensator, analyzer and a detector. The compensator (λ -plate) is used to adjust any desired polarization. A laser can be used as a light source but it is limiting the operation to a single wavelength. For spectroscopic ellipsometry a tunable light source is needed. Here often a broad band white light source with additional filters is used. Ellipsometry enables a very accurate determination of the thickness of a sample with a precision below one nanometer. This feature is due to the relative nature of the measurements, as the change in polarization between the incoming and outgoing beam is measured. In this aspect ellipsometry has a great advantage compared to other

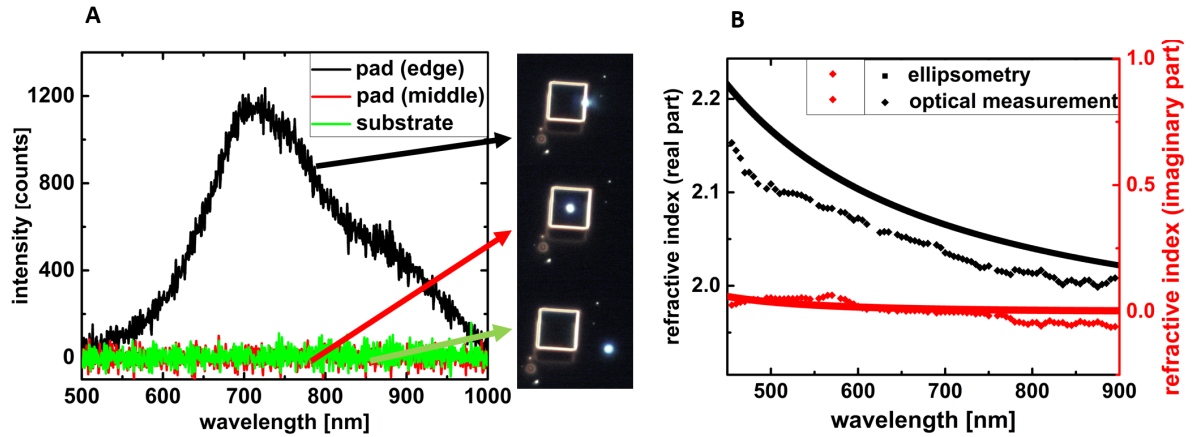


Figure 2.9: A) Darkfield scattering spectrum on the substrate (green), in the middle of the pad (red) and on the edge of the pad (black), together with an optical image of the position of the light spot. B) Permittivity of the ITO layer determined with ellipsometry and transmission/reflection measurements.

absolute optical measurements e.g. transmission and reflection.

The spectroscopic ellipsometry measurement in this thesis are performed with an UVISSEL (Horiba Jobin Yvon) phase modulated ellipsometer. The ellipsometer has an angle of incidence of 70 degree. The incident light is linearly polarized at an angle of 45 degree relative to the plane of incidence.

Imaging ellipsometry is performed with a Nanofilm EP4 from Accurion with an UV-VIS-IR nanochromat objective. The angle of incident is 45 degree and 55 degree.

Comparison of ellipsometry and the brute force algorithm To control the results of the algorithm the refractive index of a sputtered ITO layer is measured and compared to the values obtained by ellipsometry. Figure 2.9 shows the dark field scattering spectrum on the substrate, in the middle of the pad and on the edge of the pad. These points are visible in the photographs next to the image. The arrows indicate which spectrum the images correspond to. It can be seen that the EBID pad does not show any additional scattering. Just on the edge of the pad a significant scattering signal is visible due to rapid change in topography. However, in the middle of the pad where the light for the transmission and reflection measurements is taken no scattering can be detected. This is important for the algorithm where the only loss channels are the absorption in the layerstack and the reflection from the interface between the layers. Figure 2.9 B shows the permittivity of the ITO layer determined by ellipsometry and by optical measurements. The overall agreement is good. The real part has an offset of about 0.7 between the two measurements while the imaginary part is determined zero for both methods.

Raman scattering microscopy In contrast to the elastic Rayleigh and Mie scattering, Raman is an inelastic scattering process where the photon energy of the scattered light is different from the incident light [38]. The frequency of the photons changes due to the vibrational modes of molecules. Since Raman scattering induces a very small frequency shift between the incident and scattered light with a small scattering cross-section, a light source with a single wavelength is needed. The origin of the Raman signal is due to the change in polarization. In Raman spectroscopy a molecule is excited by the electric field \mathbf{E} with frequency ω_0 . The induced polarization according to formula 2.6 is $P = \epsilon_0 \alpha E$. If the vibration frequency of the molecule is ω_m with the amplitude q_0 as a small deflection from the initial position the polarizability can be expanded into a series of the following form:

$$\alpha = \alpha_0 + \left(\frac{\partial \alpha}{\partial q} \right)_0 q_0 \dots \quad (2.56)$$

Inserting this into equation 2.6 yields

$$P = \epsilon_0 \alpha E \cos(\omega_0 t) + \epsilon_0 \left(\frac{\partial \alpha}{\partial q} \right)_0 q_0 E \cos((\omega_0 + \epsilon_0 \omega_m) t) + \cos((\omega_0 - \omega_m) t). \quad (2.57)$$

The first term describes elastic scattering, while the second term gives rise to inelastic scattering where the frequency of light is shifted by the frequency of the molecular vibration, referred to as Stokes peak for the higher frequency and anti-Stokes peak for the shift to lower frequencies. Depending if a phonon is absorbed or emitted by the scattering process [38]. Equation 2.57 shows that only molecules with a change in polarization support Raman scattering. Thus, a pure metallic phase is normally not observable with Raman spectroscopy, while oxides of metal are [39]. The Raman spectroscopy in this thesis is carried out in a micro-Raman setup in backscattered configuration, using a LabRam HR800 (Horiba Scientific). The light source is a linearly polarized laser, emitting at a wavelength of 457 nm. An 100x object (numerical aperture 0.9) is used to focus the laser beam onto the sample, resulting in a spot size of about 700 nm. The spectra are taken with an Horiba iHR 320 spectrometer.

2.5 Simulation of electromagnetic waves

Mie theory gives the exact solution for the scattering problem of a plane wave with a sphere. This approach can be modified to e.g. coated spheres or ellipsoids. However, for more complex geometries no analytical solution to the scattering problem is available. Thus, numerical simulations have to be employed to understand light-matter interaction on a nanometer scale. A variety of different simulation techniques exist [40]. Under the most common ones are discrete

dipole approximation (DDA) [41], finite-element method (FE) [42] and finite difference time domain method (FDTD) [43]. While the last two FE & FDTD are used in this work to simulate the scattering and transmission of helical plasmonic structures. The FDTD method solves the Maxwell's equation in the time domain, with discrete time steps Δt . The discretization in space is done by using the algorithm proposed by Yee [44], and the cubic unit cells build up the so-called Yee lattice. It is a cubic lattice with the dimension $\Delta x, \Delta y, \Delta z$. While the computation with this discretization is very efficient the staircase approximation of structures and substrate can lead to numerical errors [45]. To minimize the probability of errors due to insufficient small mesh cells, the mesh dimensions are varied until no further changes in peak positions are observed. The final mesh size cell is 1 nm which is even below the recommended upper limit of $\lambda/20$ [46]. Another problem which arises in the time domain is that the optical properties of the material are in general dispersive. To compute the optical response in time domain a much larger frequency range needs to be provided than the frequency range of the simulation [40]. The FDTD simulations in this thesis are performed with the commercially available software Lumerical FDTD SolutionsTM and verified for analytically solvable cases. For calculation of scattering of EBID nanostructures the implemented TFSF (total-field-scattered-field) source is used. Hereby, the simulation domain is divided into a region, where the total field is computed and an outer region, where only the scattered field is computed. A plane wave is injected from below the structure with a linear polarization. Perfectly matched layers are used to hinder reflection from the simulation borders. The simulated setup cannot exactly resemble the experimental setup used for the measurement, where in darkfield configuration the sample is illuminated through an annular ring. In the case of gold nanodiscs it has been shown that this leads to a small blue shift of the resonance [47]. However, the accuracy of the simulation is high enough to resemble the measurement with its own uncertainties. Circularly polarized light is generated by two plane wave sources with the same amplitude, linearly polarized in the x and y direction and a phase difference of 90 and -90 degree for left- and right-circular polarized fields respectively. Contrary to FDTD, the limitation of a cubic lattice is not given in the FE approach. Here, the Helmholtz equation is solved in the frequency domain. Material properties, as the refractive index, can directly be used as input parameters without the need of an analytical model. The simulations are performed with the commercial software package Comsol [48]. For the simulations a three-dimensional spherical simulation domain with perfectly matched layers at the boundaries is used. The simulation is build up onto earlier verified models [49]. To determine the scattering spectrum over the whole spectral range of interest a Matlab script is used to parameterize the wavelength and extract all required quantities. Both simulations are verified by Mie calculations. Figure 2.10 A) shows the scattering cross-section of a gold sphere with a radius of 20 nm calculated by Rayleigh approximation, two different Mie calculators and the solution from Lumerical, where a gold sphere is placed inside the TFSF box and excited by a plane wave. Figure 2.10 B shows the setup in

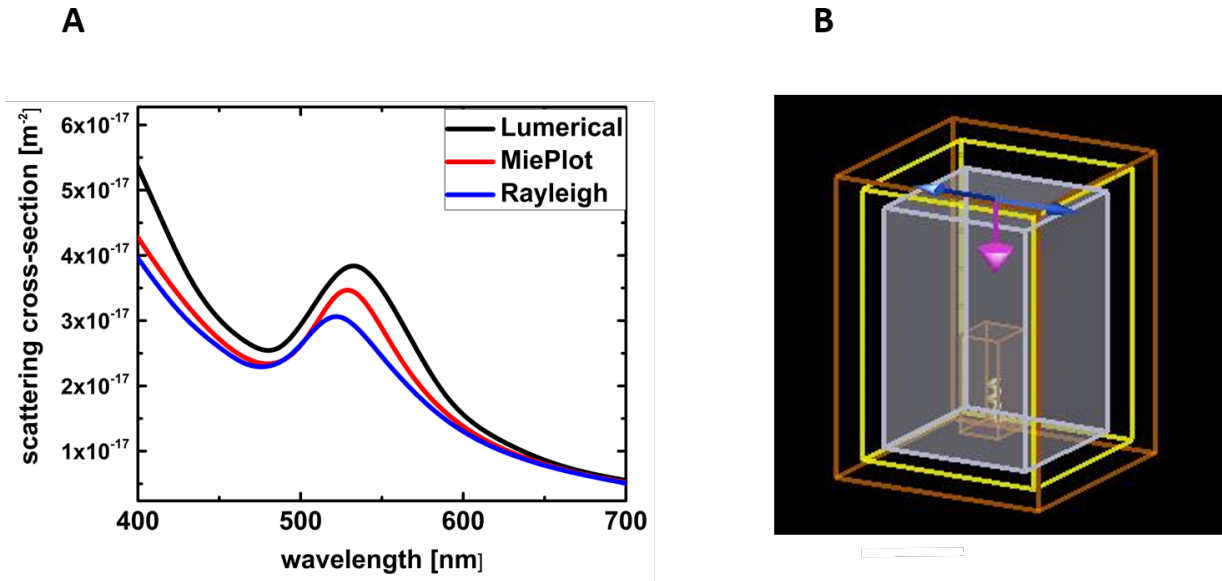


Figure 2.10: A Comparison of the scattering cross-section for a gold sphere with a radius of 20 nm calculated with the Rayleigh approximation, MiePlott [30] and Lumerical. B) Setup used in Lumerical with the TFSF source and a gold helix. Light is emitted from the top and collected in all directions.

Lumerical used for calculating the scattering intensity of the EBID nanostructures. The yellow box is the TFSF source where a linear polarized plane wave is injected from the top towards the helix. The same setup is used to calculate the cross-section for the gold sphere in A. The good agreement between the different methods proves on one hand the validity range of the Rayleigh approximation in the case of small particles and on the other hand the simulation setup used in Lumerical for calculating the scattering cross-section of more complex structures.

2.6 Scanning electron and transmission electron microscopy

Scanning electron microscope (SEM) The basic principles of the working mechanism of an electron microscope is taken from [50].

A scanning electron microscope (SEM) scans a focused electron beam under high vacuum conditions over a samples surface in a defined square pattern. The primary electrons (PE) undergo a collision cascade which defines an energy dependent interaction volume. Higher electron energies result in larger penetration depths. A compromise between surface sensitivity and lateral resolution has to be made when choosing the acceleration voltage (AC). A larger AC leads in most cases to a lower electron emission yield and a stronger signal from deeper regions while at the same time the lateral resolution is increased. To simulate the electron yield, energy distribution and penetration depth of electrons into matter Monte Carlo methods are most commonly used. The scattering cross-section calculated for the scattering of an electron with a charged ion core is used as an input parameter. The interaction between the PE with the material leads to several signals, e.g. secondary electrons (SE), backscattered electrons (BSE), Auger electrons, x-rays and cathodoluminescence. SE and BSE are used for imaging. BSE result from one or multiple elastic scattering events of PE with the atomic cores. These electrons are re-emitted through the surface and can then be collected by a detector. Because of the elastic scattering most BSE have high energies, close to the energy of the PE. The scattering probability and consequently the electron yield of the BSE depends on the atomic number. This provides a material contrast where heavier elements appear darker. BSE have an escape depth of up to several μm . SE result from inelastic scattering of either PE or BSE with outer shell electrons. The PE/BSE loses energy to an outer shell electron, ionizing the atom. The free electrons can diffuse to the surface and are re-emitted. The energies of SE are low, with an emission peak around 10 eV for most materials. While both SE and BSE have an energy distribution from zero to the PE energy, all re-emitted electrons with an energy below 50 eV are usually defined as SE. Due to their small escape depth of 1 to a few nm, SE containing more surface information compared to BSE with an escape depth of up to several micrometer. SE are collected by a positively biased grid in front of the detector. Their low velocities enable a high detection yield. BSE with higher energy are not as easy deflected such that only those emitted into the solid angle of the detector are collected. The surface sensitivity and the tilt dependent yield of SE and BSE result in an appearance of SEM micrographs similar to camera pictures. SE are normally categorized into three types. SE1 are the electrons excited by the PE, thus having the smallest lateral distribution. SE2 are electrons excited by BE within the escape range of the SE. A third contribution, SE3, comes from BE which interact with the wall of the vacuum chamber. The lateral resolution is controlled by the escape width of SE1 and SE2. The width of the SE1 escape peak is just several

nm while the peak SE2 can be of the order of μm .

Another energy loss channel for the PE is heating the sample. Through inelastic collisions the electrons transfer energy to the lattice vibrations of the sample. The heat impact is proportional to the beam current as well as to the beam energy.

Interaction between electrons and matter can lead to the ionization of atoms by removing deep core electrons. The relaxation of electrons from higher energy levels into the vacancy leads to radiation of photons with characteristic energies depending on the element. This is the basis for EDX (energy dispersive x-ray) analysis, a method to determine the material composition of a sample. However, to receive qualitative results for the element composition is highly demanding for several reasons. First, different elements have different cross-sections for EDX excitation, hence a standard is needed to quantify elements. Other effects are the absorption of lower energy quanta by heavier atoms and inversely higher energy quanta can excite EDX radiation from lighter elements. This correction are often summarized as ZAF correction for atomic number (Z), absorption (A) and fluorescence (F). The EDX analysis in this work has been done with a multifunctional Tescan Lyra 3 electron/ion microscope. The microscope is equipped with a Schottky field emitter for the electron column and a gallium ion source (FIB). Additionally, an EDX spectrometer (Bruker XFlash) is installed.

Transmission electron microscopy The working principle of a transmission electron microscope (TEM) is taken from reference [51]. In transmission electron microscopy a thin sample is investigated by the use of electrons which are transmitted through the sample. The electron energies are usually much higher in TEM (100 -200 kV) compared to typical energies in SEMs (0.5 - 30 kV). In TEM microscopy the pictures are categorized by the method they are obtained. In the simplest way a bright field (BF) detector is placed in the electron path below the sample. Sample positions where the electrons experience a stronger absorption and/or scattering appear dark, which is normally related to positions of heavier elements. The other detector type is the darkfield detector which collects scattered electrons. This type of detector is divided into annular darkfield field (ADF) detector and high angular annular darkfield HAADF detector.

The BF TEM images are taken with a Gatan Orius CCD-Camera inside a CM12 (Phillips) at an accelerating voltage of 120 KV. The HAADF measurements are done with a FEI Titan Themis³ 300 transmission electron microscope, equipped with a EDX spectrometer (Super-X).

Copper All copper-EBID depositions are performed in the Tescan electron microscope MIRA, equipped with a gas injection system from modular flow [52]. The precursor bis(t-butylacetoacetato)Cu(II), sometimes named $\text{Cu}(\text{tbaoc})_2$, is used for the fabrication of copper-

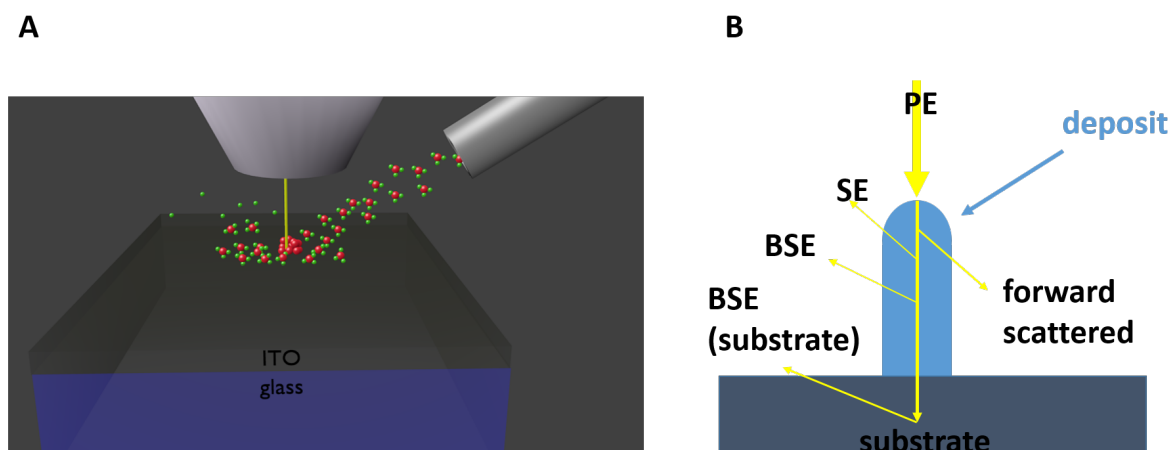


Figure 2.11: A) Sketch of the setup used for electron beam induced deposition (EBID). B) Electron path by deposition of a pillar, leading to vertical and lateral growth. B is adapted from [8].

containing deposits. The gas injection system (GIS) reservoir is manually filled prior to each deposition. The reservoir and needle can separately be heated and the temperatures are set to 100 °C for the reservoir and 105 °C for the needle. The GIS is adjusted to approximately 0.5 mm above the sample surface. The stage is heated to 100 °C. The chamber pressure during deposition is in the range of 10^{-4} mbar.

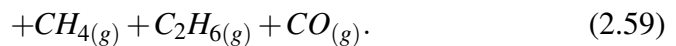
2.7 Electron beam induced deposition (EBID): Process and purification

Electron beam induced deposition (EBID) is based on the dissociative interaction of electrons with molecules attached on a substrate resulting in the deposition of one part of the molecule. The molecules are locally injected into the vacuum chamber by a GIS. A typical GIS has a reservoir where the precursor is filled into in its solid form. The reservoir can be heated to evaporate the precursor and is connected with the vacuum chamber of the SEM through a needle. The molecules diffuse through the needle onto the substrate, where they adsorb, diffuse and desorb and continuously are pumped out of the chamber. A steady state condition is reached when the supply and removal of molecules are equal. The interaction of PE with the substrate leads to an energy and lateral distribution of SE and BSE. A sketch of the deposition process is shown in figure 2.11 A. Several possible interaction of these electrons with the adsorbed molecules are summarized in the following table 2.3 [53]. Further results of electron-matter interaction that occur are polymerization and sputtering of the material. The first three interactions; scattering, vibrational and electronic excitation does not lead to any break of molecular bonds. The last four

interaction	process type
$e^- (E_i) + AB \rightarrow AB + e^- (E_i)$	elastic scattering
$e^- (E_i) + AB(v) \rightarrow AB + e^- (E_r)$	vibrational excitation (VE)
$e^- (E_i) + AB \rightarrow AB^* + e^- (E_i)$	electron excitation (EE)
$e^- (E_i) + AB \rightarrow A \cdot + B^-$	dissociative electron attachment (DEA)
$e^- (E_i) + AB \rightarrow A \cdot + B \cdot + (E_r)$	neutral dissociation
$e^- (E_i) + AB \rightarrow A \cdot + B^+ + 2e^- (E_r)$	dissociative ionization (DI)
$e^- (E_i) + AB \rightarrow A^- + B^+ + e^- (E_r)$	bipolar dissociation)

Table 2.3: Summarizing the different interactions between molecules and electrons in EBID [53].

dissociation processes, namely dissociative electron attachment, neutral dissociation, dissociative ionization and bipolar dissociation are responsible for the EBID process. By these processes the electron breaks bonds of the molecule resulting in a volatile part which is pumped out of the microscope chamber and a non-volatile part which forms the deposit. Depending on the electron energy there are different cross-section for the process types, resulting in different probabilities for the processes to occur. However, there are several problems to measure exact cross-sections for the different processes. For example, the formation of transient molecules during the EBID process is very hard to detect, if the transient molecules are further dissociated. The chemical reactions that occur during the interaction of electrons with molecules used for EBID have been studied by surface science techniques [54]. Even though the typical conditions for surface science analysis are different compared to those for EBID, (e.g. lower substrate temperature, lower power density), it gives an insight into the possible dissociation paths of the molecule [55]. The atomic composition of deposits of the gold precursor determined at low temperature, exposed by a broad electron beam from molecularly adsorbed molecules [54] are in the same range as measured from samples fabricated under typical EBID conditions [56]. Hence, the mechanisms identified at different conditions may also dominate the EBID process. For the gold precursor used in this thesis the following decomposition reaction has been identified [54].

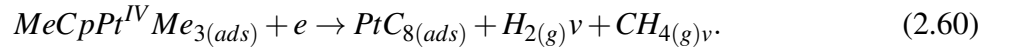


The adsorbed (ads) molecule reacts by a neutral dissociation path into the solid (s) fraction $Au^0C_6O_{0.8}$ and four molecules in the gas phase (g). The resulting EBID material has an atomic composition of 13 at.% Au, 77 at.% 10 at.% O. The cross-section has a maximum between 150 - 200 eV for the primary electrons. This suggests that the secondary electrons have a major contribution to the EBID growth. Exactly the full energy distribution of PE, SE and BE has to be taken into account and integrated over all dissociative cross-sections to determine the contribution of

each electron specimen [57].

TEM investigations on EBID structures show a carbonaceous matrix with gold inclusions of around 5 nm in size [58]. Concluding that the gold atoms are to a certain extent free to agglomerate.

A study on the precursor used for platinum containing EBID material [59] suggests a decomposition in the form of



With a similar primary electron energy dependence as for the gold precursor. To model EBID processes an integrated energy cross-section (η) is used which can be obtained self consistently from the simulation or comparison with growth rates [60]. Assuming rotational symmetry the deposition rate in units of dimension per time can be expressed by the following formula:

$$R(r) = V_m m(r) \int_0^{E_0} \eta(E) f_e(r, E) dE \quad (2.61)$$

The deposition rate depends on the density of adsorbed molecules on the surface (m), the electron energy distribution (f_e) and the energy dependent integrated dissociative cross-section of the molecules (η) [8]. V_m is the volume of the decomposed molecule.

An analytical description of the EBID process by a continuum model starts from the rate equation for the molecular density on the surface:

$$\frac{\partial m}{\partial t} = \underbrace{sJ \left(1 - \frac{m}{m_0}\right)}_{\text{adsorption}} + \underbrace{D_i \left(\frac{\partial^2 m}{\partial r^2} + \frac{1}{r} \frac{\partial m}{\partial r}\right)}_{\text{diffusion}} - \underbrace{\frac{m}{\tau}}_{\text{desorption}} - \underbrace{\eta f_e m}_{\text{decomposition}} \quad (2.62)$$

Four processes are taken into account. (1) The adsorption of molecules from the gas phase is proportional to the precursor flux J , a sticking probability s and the surface coverage $1 - \frac{m}{m_0}$. m_0 is the density of one monolayer where the whole surface is covered with molecules. (2) The diffusion from areas outside the electron beam into the deposition area is described with the diffusion coefficient D_i and the gradient of molecule coverage. r is the distance from the center of the electron beam. (3) The desorption depends on the residence time τ of a molecule on the surface after which it thermally desorbs. (4) The decomposition itself is proportional to the electron distribution and the molecular surface coverage $\eta f_e m$. For a complete picture the molecules dissociated in the gas phase have to be taken into account as well. While the basic mechanism is the same for molecules in vapor phase and adsorbed on the substrate the cross-sections and the electron densities differ [8]. The deposition process can be limited by

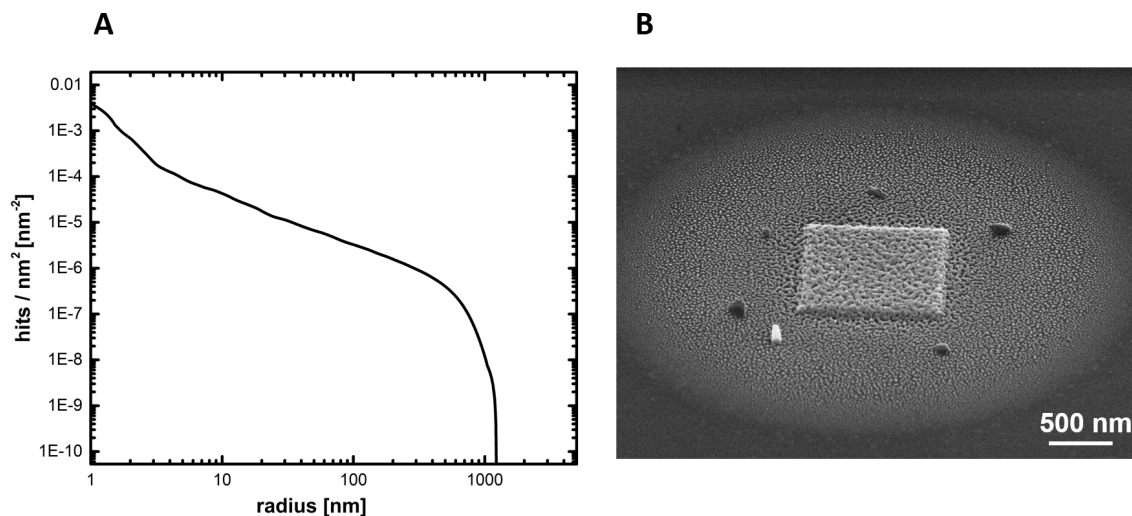


Figure 2.12: A) Normalized escape distance calculated of 200,000 electrons, with the Casino software [61] on a silicon substrate with a primary energy of 10 kV. B) EBID pad with a site length of 1 μm deposited with the gold precursor and a deposition halo with a radius of approximately 1 μm from the edge of the pattern.

the number of molecules [8]. The diameter of the GIS-needle is usually much larger than the focus of the electron beam. While the spot of the electron beam can be as small as 1 nm, the diameter of the GIS-needle is in the range of a few μm and thus the area on the substrate which is occupied by molecules is of the order of μm^2 as well. Consequently the lateral expansion of EBID deposition is limited by the electron range. Due to the discussed scattering processes of the electrons they can escape far from the impact of the primary electron beam. Figure 2.12 A shows the normalized escape distance from the primary electron beam, calculated with the simulation software Casino [61]. Even though the number of electrons emitted from the substrate strongly decreases with increasing distance from the PE, there are electrons emitted as far as 1 μm away from the center. The simulation has been performed with a beam energy of 10 kV and zero diameter onto a silicon substrate. Figure 2.12 B shows an EBID pad with a side length of 1 μm deposited with the gold precursor. The deposition time of the pad was 30 minutes. Depicted in the picture is that the electron density 1 μm away from the structure is still large enough to lead to a significant amount of co-deposition. This large co-deposition occurs in the molecular limited deposition regime. In an electron limited process the deposition rate in the proximity of the electron beam is magnitudes higher compared to μm distance, figure 2.12 A.

The deposition situation changes after an initial deposition step when the deposited area is covered with EBID material. The adsorption rate of the molecules as well as the SE and BSE yield must now be taken from the EBID material instead of the substrate, or even have a contribution

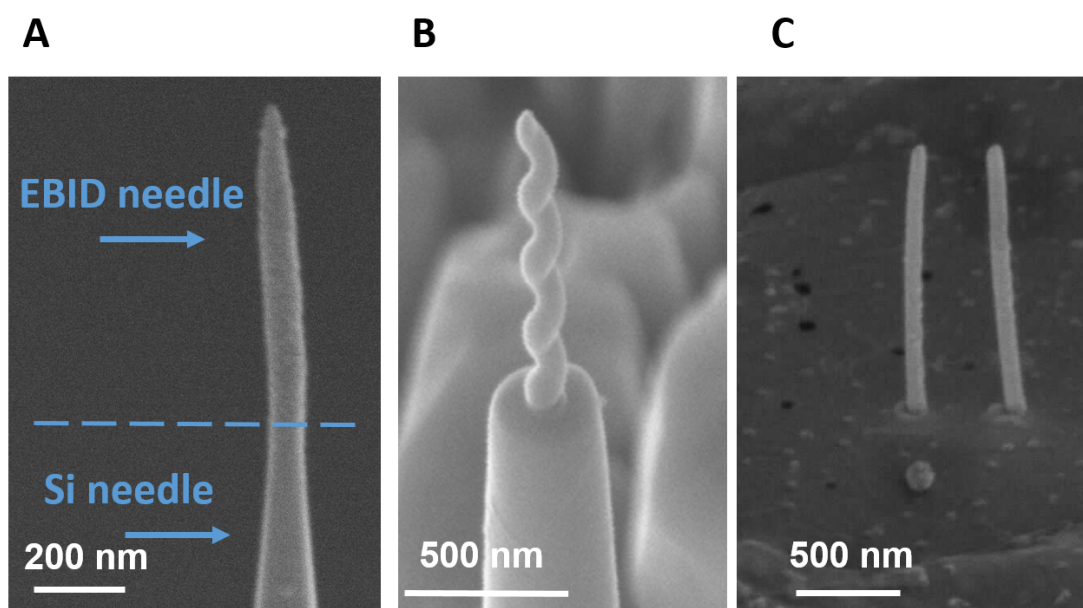


Figure 2.13: A) EBID needle onto a pre-thinned Si needle with a diameter around 100 nm. The dashed blue line indicates the border between the Si- and EBID-needle. B) EBID helix deposited onto a pre-structured pillar for TEM investigations. C) Two EBID pillars deposited on free standing graphen which hangs between GaN pillars.

from both, since the PE are still penetrating the substrate. The conditions further change for the deposition of non-planar structures. A pillar, the simplest three-dimensional structure is achieved if the electron beam is not moved but fixed at one point. The molecules now have to diffuse to the top of the pillar for further vertical growth. Additionally, the incident electrons are deflected from the EBID pillar and leaving the pillar to the sites resulting in lateral growth figure 2.11 B. Geometrical shape and atomic composition depend on the beam parameters and can be adapted as needed. Most important parameters are beam energy, beam current, dwell time, pixel spacing, number of loops, in the case of a repetitive pattern, and focus height [60].

There is a variety of different precursors available for EBID. These have to fulfill different demands e.g. a high vapor pressure, thermal stability and sufficiently long residence times when brought to the substrate [60]. The different types of EBID precursors can be categorized according to their ligands into 6 groups [8].

(1) Organic compounds, (e.g. CH_4) used for the deposition of carbon. This deposition is also observed in a SEM by the decomposition of residual gases in the vacuum chamber. Visible as darkening of the scanned area. (2) Hydrides, (e.g. Si_2H_6) (3) Halides, (e.g. TiCl_4) often toxic. (4)

Halogenphosphines, (e.g. PF_3AuCl) often corrosive and therefore not optimal for EBID. The gold precursor PF_3AuCl is one example of this group and results in pure metal deposition [62]. (5) (e.g. $\text{MeCpPt}(\text{Me})_3$) Organometallics, bonding of a metal atom to a carbon atom. $\text{MeCpPt}(\text{Me})_3$ is the precursor used for the deposition of platinum in this work. Sometimes the subgroup carbonyls (e.g. $\text{W}(\text{CO})$) is treated separately (6) Acetylacetonates, (e.g. $\text{Me}_2\text{Au}(\text{acac})$) oxygen metal bond. $\text{Me}_2\text{Au}(\text{acac})$ is the precursor which is used for the deposition of gold containing EBID structures in this thesis. Sometimes also referred to as organometallic since the gold atom is also bound to two carbon atoms (7) Alkoxides, (e.g. TEOS) Commonly used for the deposition of oxides.

Another feature of EBID deposition is the variety of possible substrates. The demands on the substrate are conductivity and a sticking probability of the precursor molecule. Hereby the EBID deposition can be placed onto the substrate with high precision of a few nanometer. Figure 2.13 shows three examples of different substrates and high lateral position control. In figure 2.13 A an EBID needle is deposited on top of a Si needle. The dashed blue line marks the border between the silicon pillar and the EBID needle. In figure 2.13 B, an EBID helix is deposited onto a pre-structured pillar with a diameter of 300 nm. This sample is used for TEM tomographic investigations. The structure can directly be investigated without the demanding sample preparation techniques, commonly used for TEM. In figure 2.13 C, two EBID needles are deposited onto free standing graphen. The graphen layer hangs between pillars of GaN. Even though the substrate is as thin as possible the electron yield of graphen is large enough to enable vertical growth.

Due to the high carbon content in EBID material from organic precursors, purification is an important topic. By varying the deposition parameters beam energy and beam current the composition of the material can be modified. A general trend is that higher beam current and/or energy leads to an increase metal content by a few atomic percent [12, 63]. The observation can most likely be explained by approaching full dissociation of all supplied molecules by this decreasing the number of partially dissociated molecules embedded into the structure. This is further supported by the observation of a cut-off energy, above no further improvement is observed [64]. Furthermore the generation of heat in the structure, especially with higher beam energy, may play a role. However, a higher substrate temperature does not lead to any improvement in the case of platinum precursor [56]. Deposition parameters are normally adjusted to the desired geometry and might not be completely free to choose for optimized composition. Stronger purification is achieved by adding reactive specimens, like oxygen, and electron irradiation at the same time [65, 66]. In contrast, electron in-situ post irradiation shows no effect [67]. Suggesting that a reactive specimen and an initial reaction power is needed.

Gold-EBID nanopillars showed a vertical decrease in gold content with increasing distance from

the substrate [68]. Suggesting a purification mechanism of the lower part due to a higher irradiation dose. In contrast to platinum, annealing of the gold containing deposits in vacuum leads to an improvement of the metal content [56]. A possible explanation is that the gold precursor contains oxygen and thus the required reactive species in itself, while the platinum precursor does not. Even for the gold precursor, purification by a heated substrate is rather limited while the purification under ambient condition can lead to almost complete purification of the deposits [69]. In summary, all purification methods apply an energy source like a laser beam [70], electron irradiation [68] or heat [56], where all can be combined with reactive species, most frequently used is atomic oxygen, atomic hydrogen or water vapor.

The following precursors are used within this thesis:

Gold Gold-EBID depositions are carried out in a FEI Strata dual beam system using the gold containing precursor $\text{Me}_2\text{Au}(\text{acac})$, which is inserted inside the chamber through an integrated Fei-GIS. The temperature of the precursor is set to 34 °C.

Platinum The platinum nanostructure depositions are performed in the same microscope as the gold depositions, with an additional GIS for the platinum precursor. The platinum deposition for the ellipsometry measurements has been done in a ZEISS crossbeam microscope equipped with a multi-GIS and the same precursor as in the FEI Strata, MeCpPtMe_3 . The reservoir is heated in the FEI to 60 °C and in the Zeiss crossbeam to 68 °C.

Selective-Carbon-Mill The purification with water vapor is done in-situ in the FEI Strata directly after deposition. A third flunch is used with the precursor named Selective-Carbon-Mill (SCM) with the chemical formula $\text{MgSO}_4 \cdot 7\text{H}_2\text{O}$. The temperature is set to 34 °C.

Carbon The carbon nanopillar is deposited with the precursor $\text{C}_{14}\text{H}_{10}$. The temperature of the reservoir is 80 °C.

3 From common to novel EBID precursors applied to plasmonics

3.1 MeCpPtMe₃ (Platinum)

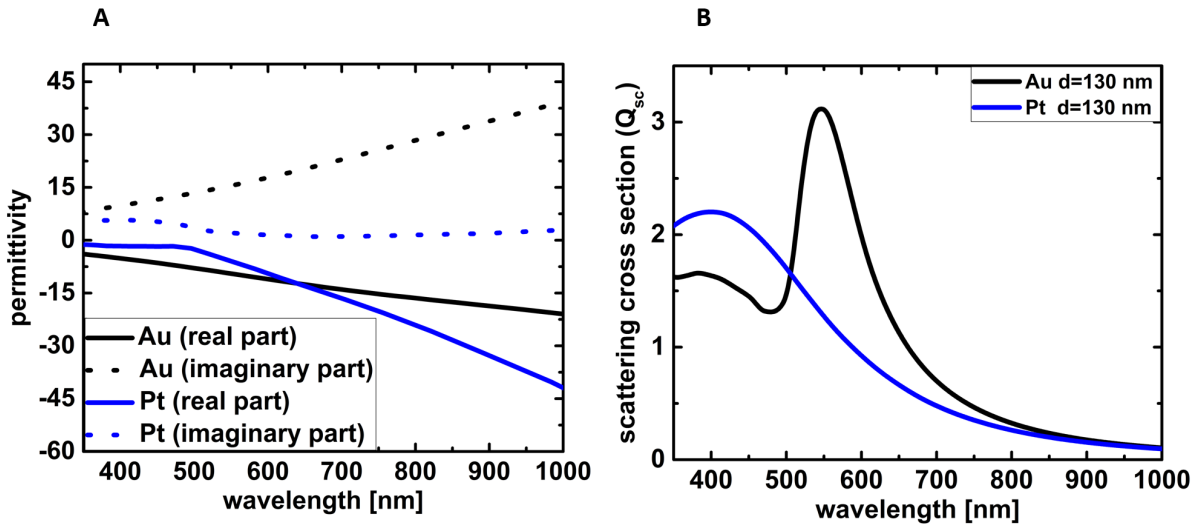


Figure 3.1: A) Comparison of the complex permittivity of platinum [19] and gold [20]. B) Scattering cross-sections, according to Mie theory [30], of a gold and platinum sphere with a diameter of 130 nm.

Platinum has shown to support localized surface plasmons on nanostructures which are tunable over a wide spectral range, starting from the UV into the infrared region. Compared to gold the scattering intensity of platinum is smaller and the width of the plasmon peak broader [71]. The reason is mainly the higher imaginary part of the dielectric function. This results in higher damping and thus a smaller scattering cross-section, with a broader linewidth and a blue shift of the resonances [72].

The same trend is displayed in figure 3.1 B for the scattering cross-section of a sphere with a diameter of 130 nm calculated by Mie theory [31]. The material data, plotted in figure 3.1 A, are taken from [19] for platinum and [20] for gold. Compared to gold, the resonance of the platinum sphere is shifted to lower wavelength.

Platinum has been used in plasmonic devices where the catalytic properties are of more importance than to achieve the highest scattering efficiencies [73]. An area inside the field of plasmonics where platinum could play an important role is the fabrication of substrates for surface enhanced Raman spectroscopy. This is the enhanced Raman signal observed on rough or

nanostructured metal surfaces [74]. The enhancement is due to two major contributions. One is the enhancement of light intensity in the proximity of metal nanoparticles, the other is a chemical contribution from a charge transfer between the molecule and the metal, dependent on the adsorb state of the molecule [74, 75]. E.g. a combination of a gold sphere with a platinum surface of distinct crystal orientation has shown to exhibit strong Raman enhancement [76].

In EBID the platinum containing precursor MeCpPtMe₃ is widely used, resulting in deposits with a platinum content of around 10 - 20 at.% with a large portion of carbon and a small amount of oxygen [8]. Besides planar deposits [65] the precursor was also used to fabricate high aspect ratio nanopillars [77]. In this study the material composition depends on the deposition parameters e.g. the dwell time. In addition to nanopillars Esposito et al [78] grew arrays of helices with focused electron and focused gallium ion beams. The as-deposited arrays showed a strong circular dichroism (CD) in the visible and near infrared region. Furthermore, they fabricated arrays of complex triple-helices which showed an improved CD signal of up to 37 % with an enhanced signal to noise ratio compare to the single helices [79]. In both cases the structures were modeled by finite difference time domain and showed good agreement between simulation and measurement. The material properties for the simulation were calculated by Maxwell-Garnett (MG) theory of amorphous carbon and platinum as input permittivities. Even though the good agreement between simulation and measurement suggests that the material properties from the MG approach well resemble the EBID material, no direct measurements of the permittivity has been done so fare. To further understand the performance of optical structures fabricated with EBID-platinum, a detailed knowledge of the material optical response is crucial.

3.1.1 Structural properties of EBID-platinum

Chemical composition The composition of EBID-platinum is investigated by EDX on differently thick samples. The thickest pad has a height of 383 nm which allows to probe the pad at a low beam voltage (4 kV) without any background signal from the substrate. Pads with heights below 100 nm are fabricated onto a silicon substrate and corrected by a thin film correction with the STRATAGEM software. The pads are measured under two different voltages (5kV and 25 kV). The measured compositions of the pads are shown in the figure 3.2 D. The measurements on planar structures suggest a rather high platinum content compared to other reported values from the same precursor [8]. Surprisingly an oxygen signal is detected even though the precursor itself does not contain any oxygen. This propose that the material composition is not solely determined by the composition of the precursor and deposition parameters but additionally by e.g. residual gases in the vacuum chamber. Another explanation is that the precursor, adsorbs

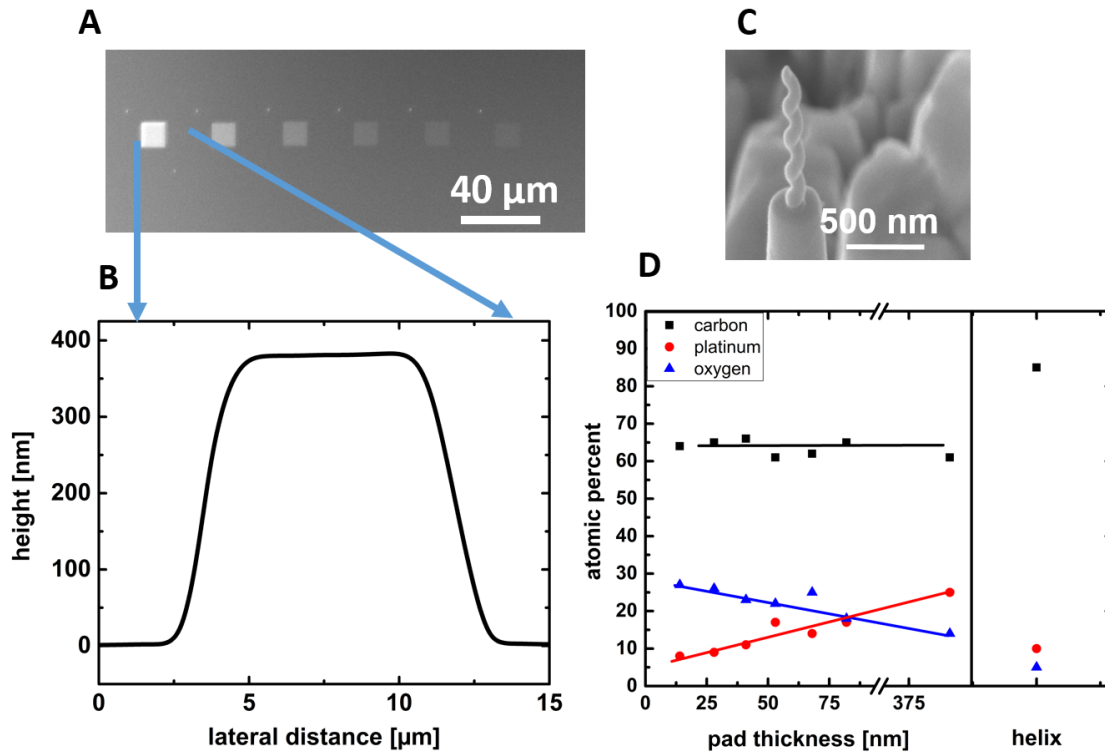


Figure 3.2: A) Array of 7 EBID pads with a side length of 10 μm and decreasing thickness from left to right. B) AFM image of the first EBID pad. C) EBID helix deposited on top of a pre-prepared pillar for EDX measurements inside a TEM. D) Atomic percent of pads with different heights. Corrected by a thin film correction. The data of the helix from C are added. Lines are to guide the eye.

moisture during storage. The thin pads give slightly lower platinum and higher oxygen values compared to the thick pad, with a small tendency of platinum increase and oxygen decrease with film thickness. A possibly reason is purification of the lower part of the pad during deposition due to a higher electron dose. In contrast to other purification processes of EBID deposits [80] the carbon content stays constant. This hints to another purification mechanism. Possibly adsorbed moisture is released during deposition. Since the oxygen from the moisture would have no covalent bonds and thus do not require high activation energy. Similar results have been observed for a copper containing precursor, where the oxygen content of the deposits was higher than the one of the precursor itself [81].

The data from the helix, figure 3.2 D, show a very low oxygen content. This might hint to a higher purification of the nanostructure due to a higher electron dose.

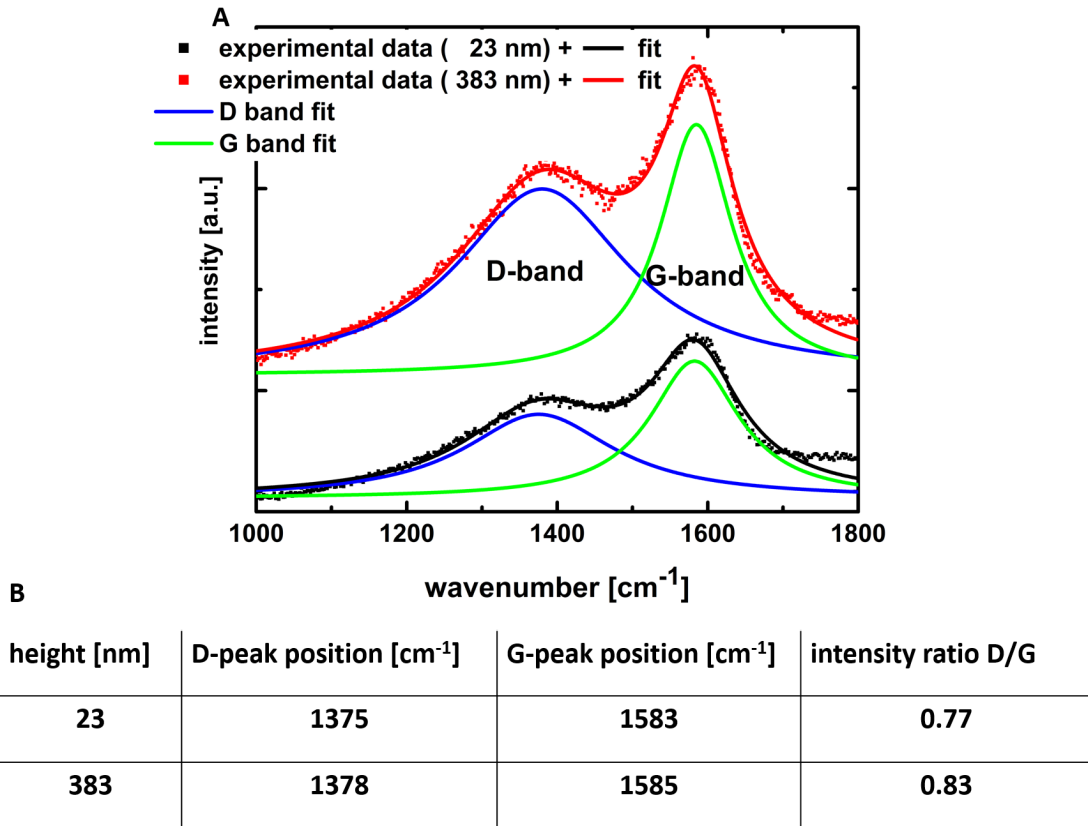


Figure 3.3: A) Raman spectra taken from EBID-platinum pads of 23 nm and 383 nm in height. Visible are the two characteristic peaks of the D and G band of amorphous carbon. B) Characteristic values of the Raman spectra for the two different heights.

Carbon configuration by Raman Spectroscopy The MG model describes the permittivity of a composite material. The solution depends on the permittivities of its constituents. While an analytical solution exist only for the case of two components, in EBID-platinum carbon, platinum and oxygen are present. However, the oxygen is not building its own phase and has to be treated as a perturbation of the platinum phase as platinumoxid or as an oxidized carbon phase. Even without the oxygen incorporation the properties of carbon based materials show a large variety depending on the structure [82]. To get some insights into the carbon structure formed during EBID, Raman spectroscopy is used. Figure 3.3 A shows the Raman spectra of EBID-platinum pads with a side length of 10 μm and heights of 23 nm (black) and 383 nm (red) respectively. Both peaks are fitted with a Lorentz shape function. Table 3.3 B shows the main characteristics of the carbon D- and G-band with their exact peak positions as well as their intensity ratios. For the pad of lower height both peaks appear at slightly lower wavelength. Also the peak intensity between the D and G peak decreases for the thinner pad.

The ratio of the peak intensities of D and G as well as the peak positions is an indicator for the amorphization state of carbon. The presence of both peaks indicates a combination of amorphous carbon and small graphite crystals [82]. A higher peak position as well as a higher D-peak to G-peak intensity ratio indicates a change from amorphous carbon to nanocrystalline [83]. For temperatures above 1800 °C a transformation of the crystal size was observed [84]. In this range an increase in the D to G ratio is related to a decrease in graphite cluster size, known as Tuinstra and Koenig relation [85]. However, for crystal sizes below two nm this relation is inverted [83]. EBID-platinum deposits have shown a change in carbon configuration during post irradiation by an electron beam [86]. The electron irradiation changes the carbon configuration from amorphous towards graphite. The effects from this transformation is a volume reduction due to a density decrease of the carbon matrix as well as an increase in conductivity. Also observed for carbon and cobalt containing precursors during post thermal annealing [87, 88].

In this thesis a different carbon configuration for thin and thick pads is observed, figure 3.4. The higher pad, with a longer deposition time, shows the feature of a carbon matrix with a higher ratio of graphite crystals to amorphous carbon. This suggests that the transformation starts already during the deposition process. A possible explanation for the different carbon configuration in thicker pads is the higher heat impact during longer deposition times. The observed change in the Raman peaks is attributed to the conversion of amorphous carbon into nanocrystalline carbon, with crystal sizes below 2 nm. Another observation during the annealing of a cobalt precursor was the release of oxygen [88], which agrees with the EDX analysis of platinum in this work, which shows a small oxygen decrease for thicker pads.

3.1.2 Permittivity of EBID-platinum: Optical measurements and a model

Permittivity from transmission and reflection To determine the permittivity of EBID-platinum the same method as in reference [36] is used. The EBID pads in figure 3.2 A have a side length of 10 μm and are grown onto a glass substrate covered with 50 nm ITO. The pads are deposited at 10 keV energy, 10 μs dwell time, a pitch of 10 nm, beam current of 300 pA and a varying number of loops (90, 180, 400, 2000) is used to achieve the different heights 23 nm, 46 nm, 95 nm and 383 nm. The pads are measured in transmission and reflection. The normalized spectra are used as input parameters for the brute force algorithm to determine the permittivity. Figure 3.4 A and B shows reflection and transmission measurements of pads of four different heights. The transmission shows a steady increase from 450 nm to 900 nm, while the reflection strongly depends on the thickness of the pad. As expected the thicker pads show a lower transmission, most likely just due to the longer optical path. Figure 3.4 C and D shows the retrieved real and

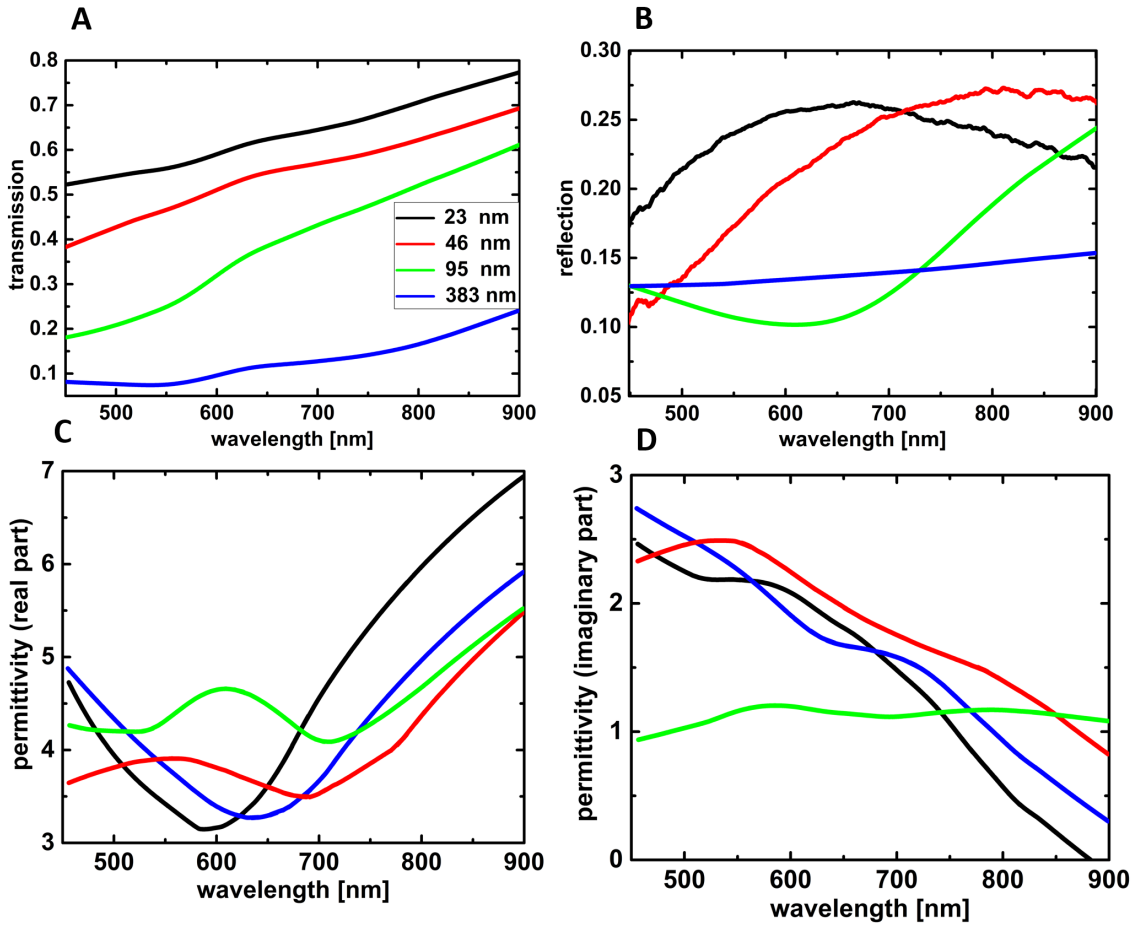


Figure 3.4: A) Measured transmission B) reflection spectra of square EBID-platinum pads of four different heights. Real C) and imaginary B) part of the permittivity, calculated with the brute force algorithm.

imaginary part of the permittivity. The lower pads show a minimum value of 3 around 650 nm for the real part of the permittivity. This minimum seems to shift towards higher wavelength together with a small increase. By the 95 nm high pad and even more pronounced in the case of the 383 nm high pad an additional maximum appears around 600 nm. The height dependence of the permittivity has its origin in the different platinum content and the different carbon configuration. However, for all pad heights the retrieved values are above 3 which indicates a dielectric rather than a metallic behavior. The imaginary part shows small values in the measured wavelength range while it continuously decreases to longer wavelength.

Permittivity from ellipsometry A common technique to determine the permittivity of thin films is ellipsometry. Normally performed on large areas makes ellipsometry no suitable tool

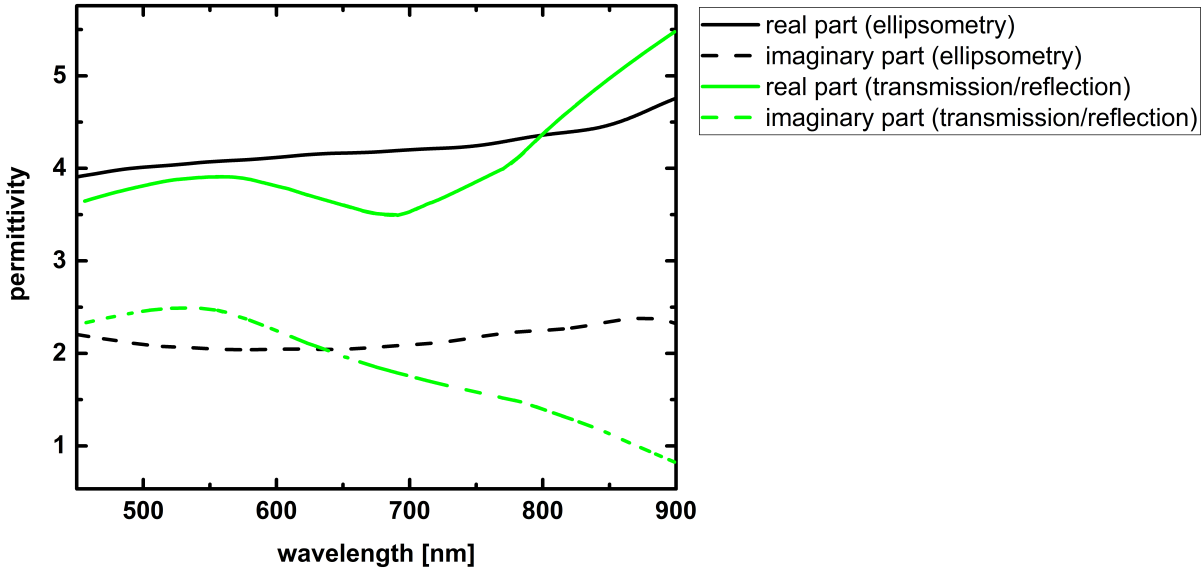


Figure 3.5: Permittivity measured with ellipsometry (height 88 nm) and with transmission and reflection of the pad with approximately the same height as used for ellipsometry (95 nm).

for EBID where the deposition of areas with sizes of μm^2 takes unreasonable long. However, imaging-ellipsometry is capable to measure areas of a few micrometer [89], which is in the range of EBID. To measure the permittivity of EBID material with another method holds the promise to verify the results from the brute force algorithm. For ellipsometry an EBID pad with side length of $50 \mu m$ and 88 nm in height is fabricated. Figure 3.5 shows the complex permittivity of the EBID-platinum determined with ellipsometry together with the result from the brute force algorithm of a pad in the same height range. The ellipsometry measurement shows a continuous increase of the real part with increasing wavelength, while the imaginary part has a small parabolic shape. The real part shows the same magnitude as well as wavelength dependence as determined with the brute force algorithm, even though the results show some deviation from another. This remaining difference could result from small mismatch in height or on different deposition conditions. The sample prepared for ellipsometry is grown on a silicon substrate because of the well-known properties of silicon, making it most suitable for ellipsometry. However, for the brute force algorithm transmission measurements are necessary demanding a transparent substrate. Furthermore the deposition conditions are different in the case that for larger pads the refreshing time (time between the electron beam is on the same position again) is longer. This might result in different composition and thus different permittivity. The deviation from both methods is more pronounced for the imaginary part. For the lower wavelength range both methods give similar results. The decrease determined by the brute force method is not resembled in the ellipsometry measurements. Even though both methods do not perfectly match each other they

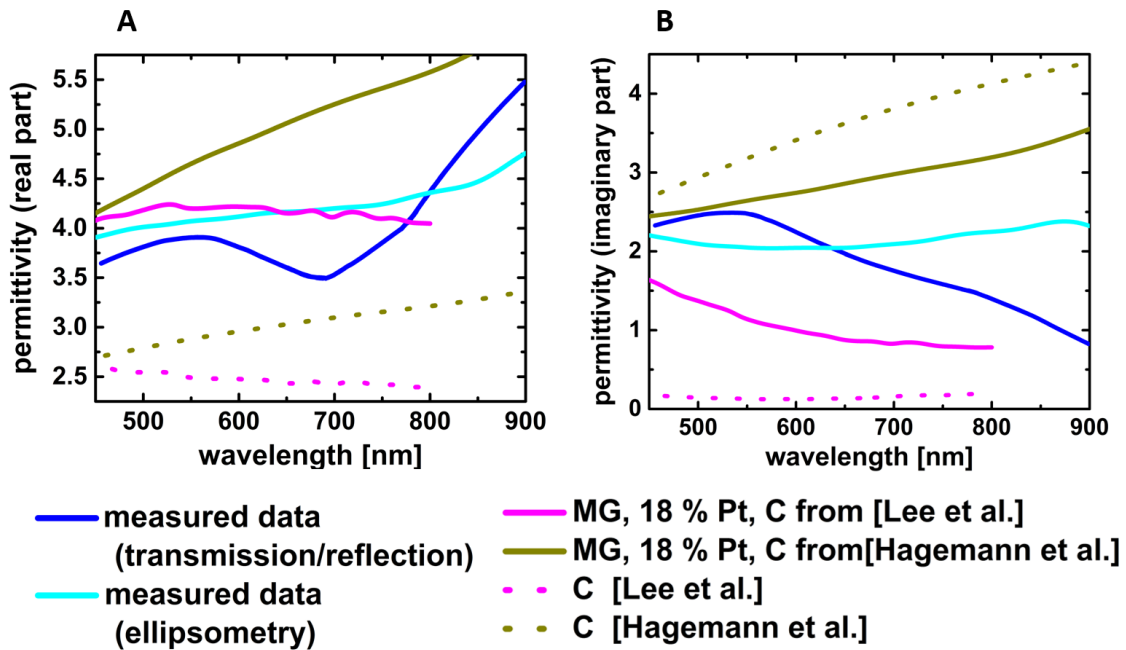


Figure 3.6: A) Real part and B) imaginary part of the effective permittivity of a mixed material composed of carbon from Hagemann et al. [90] and Lee et al. [91] with a platinum volume fraction of 18 %. The material parameters for platinum are taken from [19].

both show a dielectric behavior of the material with a low absorption coefficient. The real part of the dielectric function is positive over the whole spectral range, indication that the as-deposited EBID material shows no feature of a metal.

Maxwell-Garnett model for EBID-platinum From the investigation of the carbon state inside the EBID material no direct link to the permittivity can be made. However, the knowledge about the nanocrystalline graphite restricts the possible carbon permittivities to some extent. Together with the results from the EDX measurements some boundaries for the input parameters for the Maxwell-Garnett model can be identified and the results can be compared to the measurements from the ellipsometry and the brute force algorithm. In figure 3.6 the permittivity of a mixtures of amorphous carbon with platinum is plotted as well as the permittivity obtained from the ellipsometry measurement and the brute force algorithm. Figure 3.6 A shows the real part and B the imaginary part respectively. The material parameters for platinum are taken from [19] and two amorphous carbon configurations are used, Hagemann et al [90] and Lee et al. [91]. The second configuration is carbon deposited by EBID with a carbon containing precursor. This is one example where the dielectric function of EBID material was measured. In this study, dark-

field scattering properties of as-deposited purely organic EBID material, just containing carbon and oxygen, using oil molecules (octadecyl-naphthalene) as a precursor supply, has been investigated. The size structure is around 200 nm in height and width while the length is 4.5 μm . The refractive index has been measured to be almost constant, with a value around 2.5 for the real part and a very low imaginary part. Starting around 0.7 for 250 nm and even decreasing for longer wavelength [91]. The permittivity of the effective medium is plotted for a volume fraction of 18 %. For comparison also the permittivities of the pure carbon phases are plotted in the graph. The real part of the permittivity is well resembled by the MG model and the carbon configuration obtained from the carbon containing EBID precursor. The values obtained from the carbon configuration from Hagemann et al. gives larger values than measured. The decrease for the imaginary part of the permittivity with higher wavelength is reproduced by the carbon configuration from EBID. However, the values are too small. This suggests that an additional loss channel is present in the case of EBID-platinum, additionally to case of pure EBID-carbon. The incorporation of oxygen into amorphous carbon leads to a decrease in the real part of the refractive index [92] and thus to a decrease in the real and imaginary part of the permittivity. This effect might explain the higher values, obtained from the carbon configuration from Hagemann. The MG model shows that in the typical metal volume range from EBID material the optical properties are determined by the configuration of carbon where the inclusion of metal particles leads to higher values for the real part of the permittivity. This might drastically change in the case of purified material where the metal component becomes dominant. The results support the validity of the MG theory for modeling the permittivity of EBID materials while at the same time points out the difficulties by the unknown carbon configuration which depends on the deposition parameters.

3.2 $\text{Me}_2\text{Au}(\text{acac})$ (Gold)

Gold is one of the most used materials for plasmonic applications even though there is a search for replacing it with other materials [93]. In the visible and near-infrared range silver is the best plasmonic material because it has the lowest losses. In terms of losses gold is the second choice while it is used more frequently because of its higher chemical stability compare to silver [94]. Besides platinum, gold containing EBID precursors are well investigated. Between the various possible EBID precursors available for gold deposition the precursor AuClPF₃ is one of the view examples where the resulting structures are of pure gold crystals [95]. However, the precursor is unstable under room temperature and has to be kept below 10 °C to avoid any decomposition during storage, making it difficult to handle. The electrical resistance of the pure gold crystals is still about ten times the bulk value due to the grain size structure of the material [96]. The

precursor used in this work is the metal organic precursor $\text{Me}_2\text{Au}(\text{acac})$. The metal content for this precursor is rather low. Reported are values from 5 at.% [80] up to 12 at.% [97] for the as-deposited structures. There are a variety of different approaches to increase the metal content of EBID structures mostly applied to planar deposits [80].

So far there hasn't been paid a lot of attention to the optical properties of EBID material and its use in nano-optic or plasmonics. As-deposited dots from the precursor have been shown to support broad resonances without any distinct feature while annealing the material results in scattering spectra with a peak at around 600 nm [98]. This can be attributed to Mie resonances of small gold particles. Another investigation with the gold precursor resulted in a thickness dependent refractive index ranging from dielectric to slightly metallic in the thickness range from 50 nm to 15 nm [36]. Since the material composition of EBID depends on the deposition parameters, a different metal to carbon ratio could be one explanation for the height dependence. Another explanation for the metallic behavior of very thin pads could be that the size of the gold clusters in the EBID material are approaching the thickness of the pad, thus no longer forming isolated spheres but a material composite of connected gold spheres.

3.2.1 Structural properties of EBID-gold

As mentioned the gold content from EBID deposits of gold precursors are between 3 - 15 at.% depending on the deposition conditions. In this thesis EDX measurements on nanopillars in a TEM shows 10 at.% gold, 11 at.% oxygen and 79 at.% carbon, well in the range of literature values. There are not many information about the resistivity of this specific precursor. Other gold containing precursor like $(\text{Me}_2\text{Au}(\text{tfa}))$ give higher metal contents in the as-deposited structures of around 20 at.%, with resistivities about $10^4 \mu\Omega\text{cm}$ [96]. It has been shown [95] that the resistivity of gold EBID can be decreased by three orders of magnitude when changing the pattern from a single slow to multiple fast scans while keeping the dose and the beam current constant. However, the improved conductivity was attributed to different percolation of the gold crystals rather than a higher metal content. The typical EBID microstructure suggests that, as long as no connection between the metal clusters is reached, the resistivity is dependent on the distance between neighboring clusters and the resistivity of the surrounding carbonaceous matrix [99, 100]. This results from the fact that the metal inclusions are highly conductive in contrast to the surrounding carbon. To determine the resistivity of the as-deposited EBID material from the gold containing precursor current-voltage curves are recorded between gold pads with different distances. From the slope the specific resistivity is determined to $3.6 (\pm 14) 10^4 \mu\Omega \text{ cm}$ for the as-deposited EBID material, which is slightly higher than the value from $\text{Me}_2\text{Au}(\text{tfa})$.

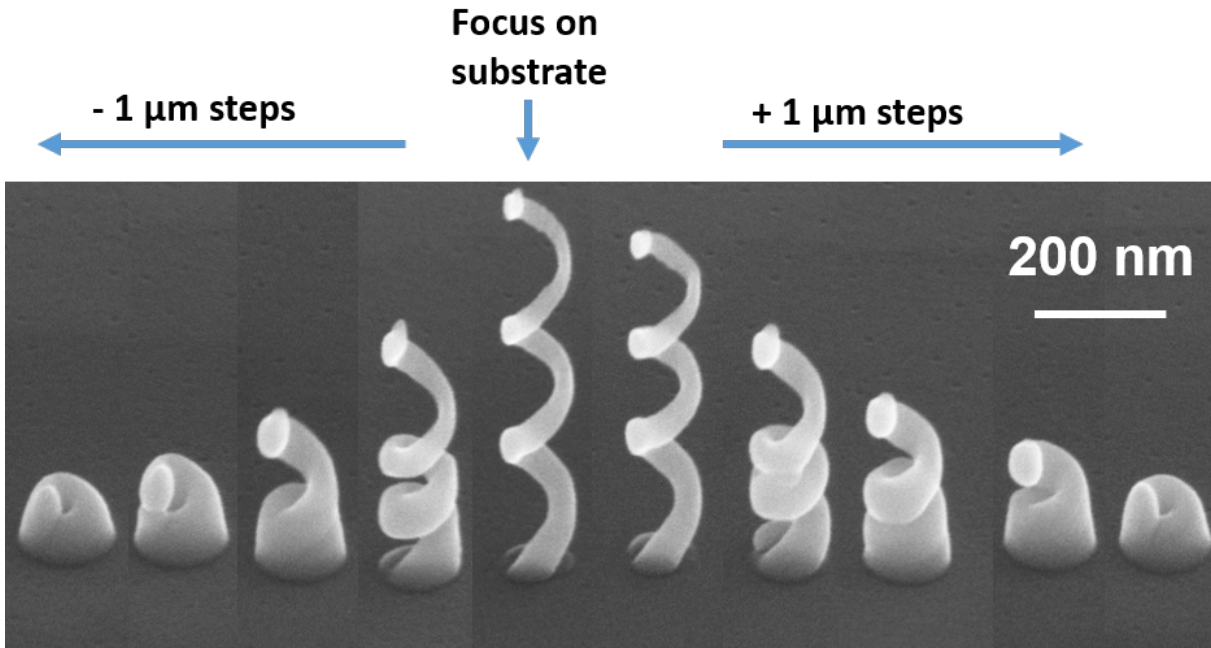


Figure 3.7: EBID helices grown at different focal planes of the electron beam. The helix in the middle is deposited with the focus on the substrate while the helices to the left and to the right are grown with the focus above and below the surface in $1 \mu\text{m}$ steps .

3.2.2 Plasmonic nanostructures by EBID-gold: Fabrication and optical properties

Deposition of 3D structures One big advantage of EBID fabrication is its ability to create complex three-dimensional structures, like helices. One important parameter is the focus height of the electron beam. This is especially critical because the focus height has to be manually adjusted before every deposition and is not numerically given into the software as an input parameter, like the accelerating voltage. Thus, the reproducibility of the focus is critical. When changing the focus the number of electrons impinging onto the surface does not change. Thus a decrease in the deposition rate is not expected. In fact for the platinum containing precursor even an increase in the deposition rate for a defocused electron beam was observed [101]. But additional to the increase in volume growth rate was the broadening of deposited pillars observed, where the vertical growth rate was largely decreased for the defocused beam. Figure 3.7 shows helices grown with different focal planes of the electron beam. The other deposition parameters are kept constant at 15 keV energy, beam current 203 pA, pixel spacing of 1 nm and a dwell time of 1.2 ms, 1.4 ms and 1.8 ms corresponding to the first, second and third pitch. For the helix in the middle the electron beam is focused onto the substrate and then decrease in one μm steps for the helices to the left and increased in the same step size for the helices to the right. The decreased vertical growth rate shrinks the helix to a broad nanopillar.

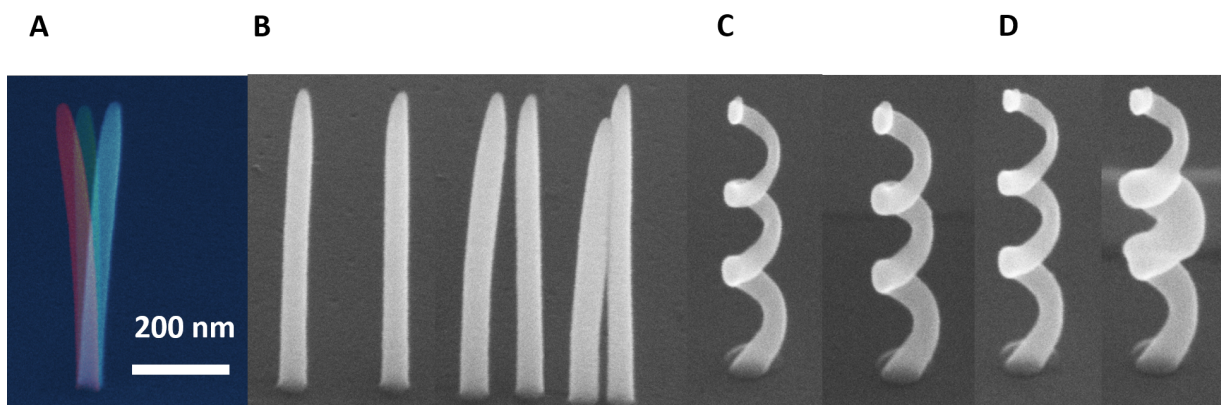


Figure 3.8: A) Bending of an EBID pillar by placing the electron beam on the right (blue) and left (red) site of the pillar. B) Bending and thickening of an EBID pillar when depositing a second pillar in close proximity. C) Post thickening of the second and third pitch of an helix to achieve equal wire thickness. D) Thickening of the second pitch from a helix, with high spacial precision as well as co-deposition on the substrate.

Modification by post-deposition and -irradiation While most EBID structures can be deposited within a single step process, there are ways to further modify and tune the deposited structures. The impact of the electron beam results in a positive charged surface while the bulk material has an excess of electrons. In the case of a single nanostructure like a nanopillar it is expected that most primary electrons (PE) hitting the pillar will be deflected out to the side or entering into the substrate. SE and BE will be excited on the way of the PE and leave the structure if they are within their escape depth. Thus a nanopillar bombarded with PE is positively charged. The pillars in figure 3.8 are deposited at 15 keV energy, 203 pA beam current in spot mode with a deposition time of 6 seconds. Figure 3.8 A shows an as-deposited pillar (green) together with the same pillar where the electron beam has been placed for 30 seconds 50 nm to the left (red) and right (blue), respectively. It is observed that the pillar bends towards the electron beam. The PE has in good approximation a Gaussian shape, so even if the focus of the beam is put 50 nm next to the structure the tail of the Gaussian beam hits the EBID pillar, resulting in a positive charge. The process of bending the EBID pillar is reversible by placing the electron beam on the other site until the point where the pillar is straight again. In figure 3.8 B the same effect is visible when depositing two pillars in close proximity to each other. As the distance decreases the first pillar starts to bend towards the second pillar, probably due to the same mechanism as the deposited structures bend towards the electron beam. Another modification visible when a second pillar is grown next to another is an increase in thickness for the first pillar. The thickening of the first pillar is due to the tail of the PE to the scattering electrons from the second pillar. This effect gives a limit to the distance of two EBID structures without perturbation. In reference [102] this effect was used to increase the growth rate of EBID structures due to an

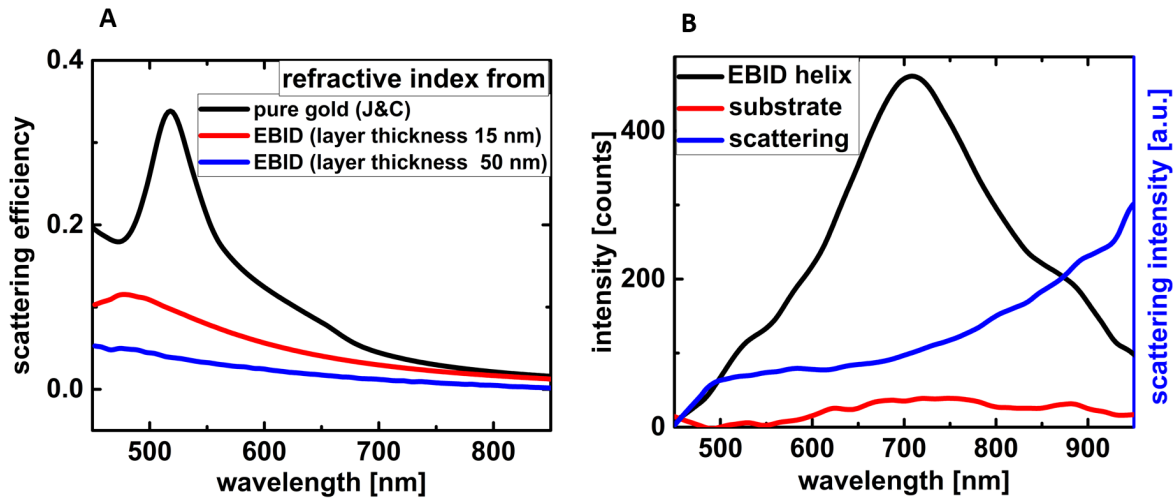


Figure 3.9: A) Mie calculated scattering spectra of a pure gold sphere of 70 nm diameter, with values from [20] compared with scattering obtained from the dielectric function of EBID from [36] for the thinnest and thickest pad. B) Measured scattering spectra of a single as-deposited EBID helix. Also plotted are the intensities taking from the substrate and the helix.

increase of electron yield through forward scattering. However, this effect can further be used to intentionally modify grown EBID structures. The helix in figure 3.8 C shows a decrease in arm thickness from the first round to the third. This unequal radius results from the broadening effect of the already deposited pitches with every new one. This can be compensated by post thickening of the second and third pitch. The grown EBID helix is tilted to 52 degree. A rectangular pattern shape with 15 keV, 203 pA, pitch distance 10 μm and dwell time 1 μs is used to thicken the middle pitch for 90 seconds and the third pitch for 180 seconds. In D the thickening has been performed on the second pitch while the time has been increase to 5 minutes to show the spatial precision of the post processing step. Visible is also that during the thickening process of the helix a square is deposited on the substrate resulting from the electrons which are transmitted through the helix.

Scattering of as-deposited EBID-gold helices A careful search of the relevant literature gave no result on scattering properties of as-deposited EBID-gold structures reported so far, except [98], who investigated dots and pillar arrays, as mention before. A single EBID-gold helix with three pitches is investigated with darkfield scattering spectroscopy. Figure 3.9 B) shows the scattering spectrum which increases towards higher wavelength. Within the measured spectral range no distinct features are present. Figure 3.9 A shows a Mie-calculated scattering spectrum from a sphere with a diameter of 70 nm. The permittivity for the EBID material has been taken

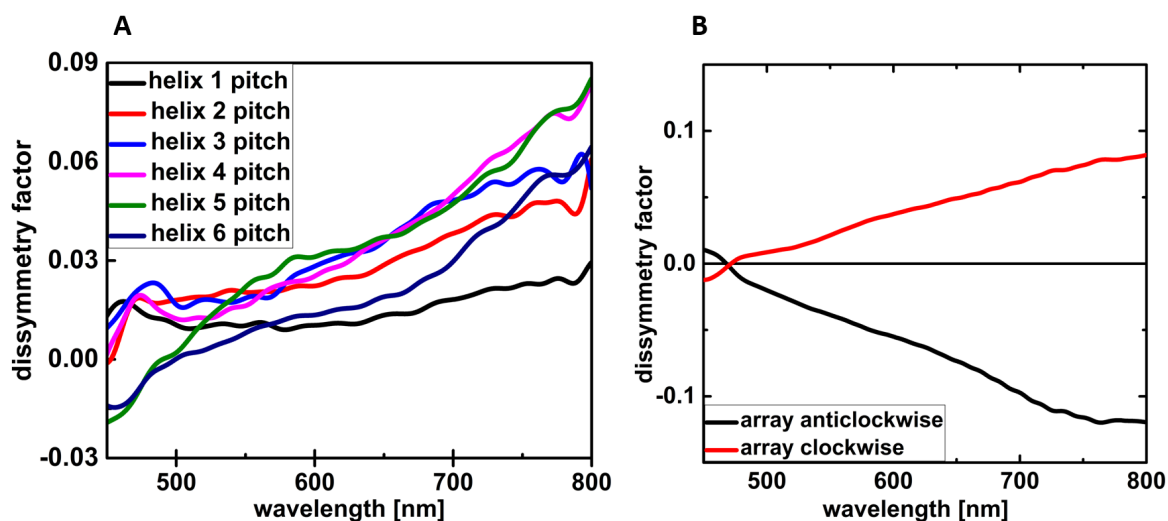


Figure 3.10: A) Dissymmetry factor of a single as-deposited EBID-gold helix with pitches from 1 to 6. B) Dissymmetry factor of a helix array with 3x3 helices, three pitches and its mirror image. Data taken from [103].

from [36] for the thinnest and thickest sample height. As comparison, the scattering spectrum of a pure gold sphere with the values taken from [20] has been added. Due to the dielectric nature of the EBID material no distinct resonance is visible for the values from the 50 nm height pad while the other one shows a very shallow peak around 500 nm. Both plots mainly show a smooth decrease in scattering intensity as expected for small particles with constant refractive index. In comparison the pure gold sphere shows a strong resonance around 540 nm. While the scattering spectrum of the helix shows an increase at higher wavelength suggesting a broad resonance which might be attributed to the helical shape. In general the dielectric EBID material hinders the plasmonic resonance, responsible for the strong scattering of small metal particles.

Transmission dissymmetry of as-deposited EBID-gold helices Although the scattering spectrum of the as-deposited helix does not show any distinct features they do exhibit a difference in transmission of left- and right-circular polarized light shown in figure 3.10, taken from [103]. The single helices show an increasing dissymmetry factor with increasing wavelength. Visible is also a slight increase with increasing pitch number while the overall signal is low. The dissymmetry signal is stronger when depositing an array of helices, plotted in 3.10 A. The array consists of 3x3 helices with a distance of 500 nm between the centers of the helices. The array does not change the general behavior but increases the intensity. Even though the array does not alter the wavelength dependence, the dissymmetry factor cannot simply be calculated by multiplying the number of helices with the response of a single one, but shows a lower value. In figure 3.10 B

the dissymmetry factor of a 3x3 array of helices with three pitches is compared with the same array where the direction of rotation of the helices is reversed. Depicting a mirror image of each other the array with the helices rotating anticlockwise shows a slightly lower absolute value of the dissymmetry. The reason for that could be small geometrical variations in the helices of the two arrays or being attributed to the uncertainty of the measurement. The inversion of the signal when changing the rotation of the helix is an indicator that in fact the circular dichroism is measured and no artifact from the light source together with the linear dichroism (LD) of the helices. That arrays of as-deposited EBID-gold helices do exhibit an linear dichroism has been shown in [49]. Because of the rotational symmetry of the single helix the origin of the LD is most likely due to the end of the helix which breaks the rotational symmetry. Another influence could arise from the array and not the single element.

3.3 $\text{Cu}(\text{tbaoac})_2$ (Copper)

High electrical and thermal conductivity are the most famous properties of copper and the reason it is commonly used in electric and electronic devices. Together with its high abundance and cheap price copper was one of the most important metals in the 20th century used for cables, generators and transformers [104]. During the last years FIBID and EBID has been used to electrically contact nanometre-sized materials [105, 106]. This depositions were always performed with a platinum containing precursor which is very well investigated, regarding deposition parameters, conductivity and purification methods [67, 101, 107]. Comparing the bulk resistivities of platinum and copper, platinum is about 6 times as high. Making copper the more favorable material for electrical wires. While silver and gold are two of the most prominent materials used for plasmonics, so far only a few investigations about plasmonics with copper have been made [108]. Even though in the periodic table copper stands above silver and gold in the 11th group of the periodic table, featuring the same electron configuration of a full d band and a half filled s band [109]. The similar configuration suggest that the properties of copper could be as well suited for plasmonic applications. The desired configuration for plasmonic applications is a high negative value of the real part of the permittivity and a low value of the imaginary part. Indicating a strong localization of the electro-magnetic field and a low absorption respectively. Figure 3.11 shows the permittivity of the three metals gold, silver and copper. Material values are all taken from [20]. The real part shows a similar metallic behavior for all three materials, while the value for silver is slightly more negative. In the imaginary part the interband transitions are visible in form of a step increase. For copper this transition starts around 600 nm, for gold around 500 nm while the value for silver is shifted to smaller wavelength, starting around 300 nm. It has been shown for all three metals that they exhibit localized surface plasmon resonances

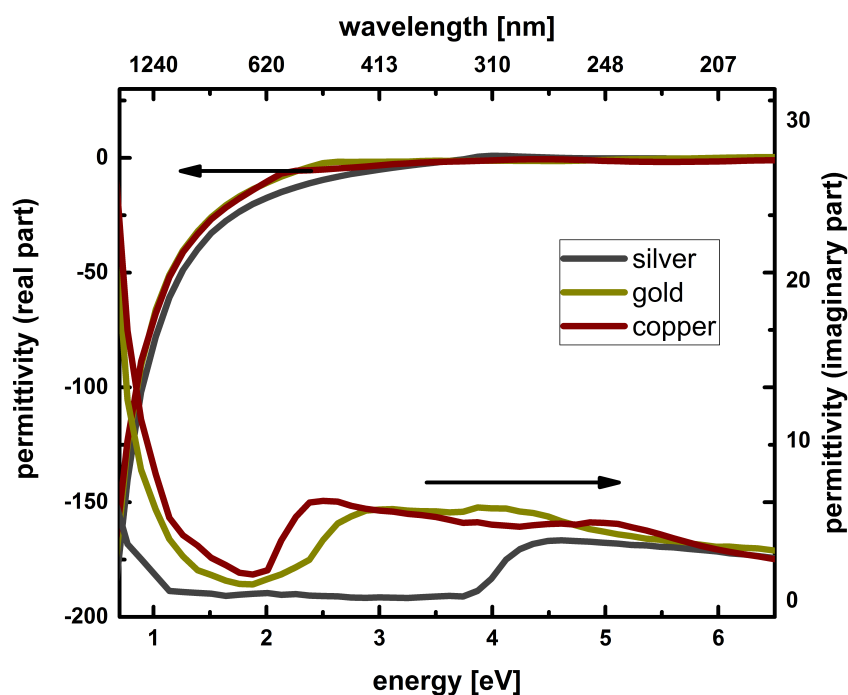


Figure 3.11: Complex permittivity of Ag, Au and Cu from Johnsson and Cristy [20]. The similar behavior of the optical properties is due to the similar electron configuration. In the imaginary part are the different energies visible where the interband transition occurs.

tunable throughout the visible to near infrared spectrum [108, 110, 111]. Without decreasing the efficiency, silver shows a larger tuning range towards smaller wavelength because of the spectral position of the interband transition. The advantage of gold over silver and copper is the chemical stability in ambient conditions. The sulfidation of silver leads to a red-shift and decrease of the dipole plasmon resonance [112]. Copper is also unstable under ambient conditions. At the copper air interface copper oxides are formed which can be either cuprous oxide (Cu_2O) or cupric oxide (CuO) depending on the condition during oxidation. For room temperature the (Cu_2O) face is dominant [113]. For copper particles it was found that the oxidation follows a linear growth behavior without any self-limiting process within the time frame of one year [113]. Therefore a way of hindering the oxidation of copper nanoparticle when using it for plasmonics has to be found. It has been shown that a multi-layer graphene can effectively hinder the oxidation of copper nanoparticles [114]. The grown carbon matrix during the EBID process could act as a natural barrier for the oxidation of the copper structures.

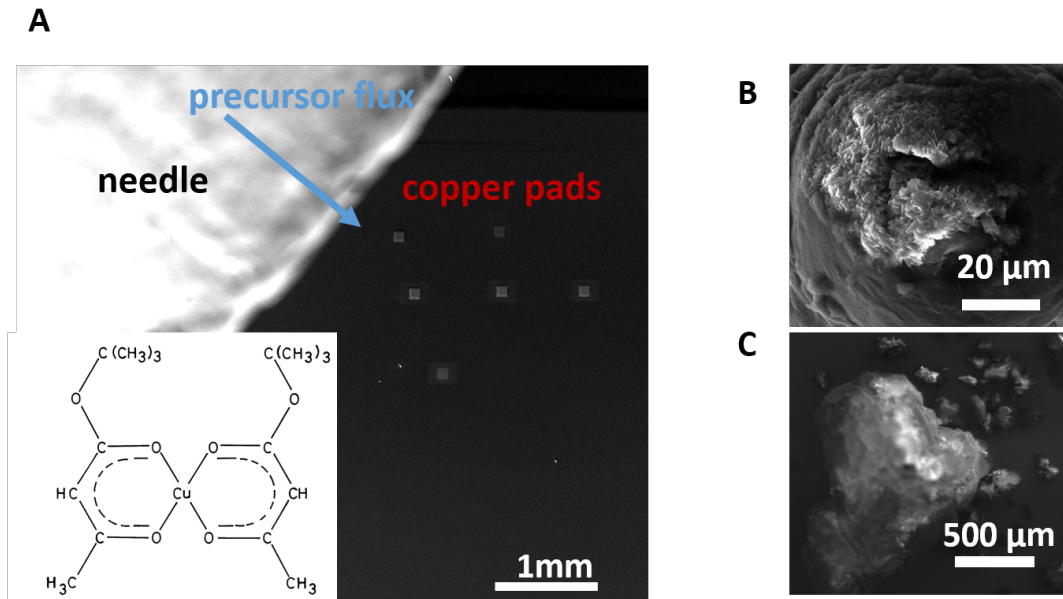


Figure 3.12: A) Deposited copper pads and the needle of the GIS system. In the left lower corner is the structure of the copper containing precursor $\text{Cu}(\text{tbaoac})_2$ [117]. The atomic composition of the precursor according to the formula is 1:6:16:26 (Cu,O,C,H). B) Precursor frozen to the substrate at a temperature of 80 °C. C) Scanning electron micrograph of the precursor.

3.3.1 A novel copper precursor for EBID: Deposition and 3D structures

Fabrication of copper containing deposits by electron beam induced deposition has been shown with a type of precursor containing hexafluoroacetylacetonate ($\text{C}_5\text{H}_2\text{F}_6\text{O}_2$) bound to the copper atom. With this type of precursor planar structures as well as nanopillars has been realized. The metal content of this precursor is between 11 at.% [115] and 15 at.% [116] for the as-deposited material. In Luisier et al.[116] the purity of the material was improved during the Auger electron spectroscopy measurement leading to copper contents of up to 70 at.%. In reference [115] the measured resistivities was two times below the value of bulk copper with is in contradiction to the low metal content. In the case of Luisier et al. [116] the deposited material showed an insulating behavior and the resistivity could only be measured after purification. A possible explanation for the mismatch between metal content and very good resistivity stated by the authors [115] is that both experiments, metal content and resistivity, were performed under different deposition conditions (30 kV and 50 kV respectively). The copper content of the precursor is in the same range observed for other materials deposited by EBID [8]. All reported copper precursors contain fluorine which can be unwanted inside an SEM chamber due to its etching properties. The used metal-organic precursor bis(*t*-butylacetoacetato)Cu(II) is a fluorine free precursor which has been introduced for chemical vapor deposition (CVD) of copper films [117]. The CVD process leads

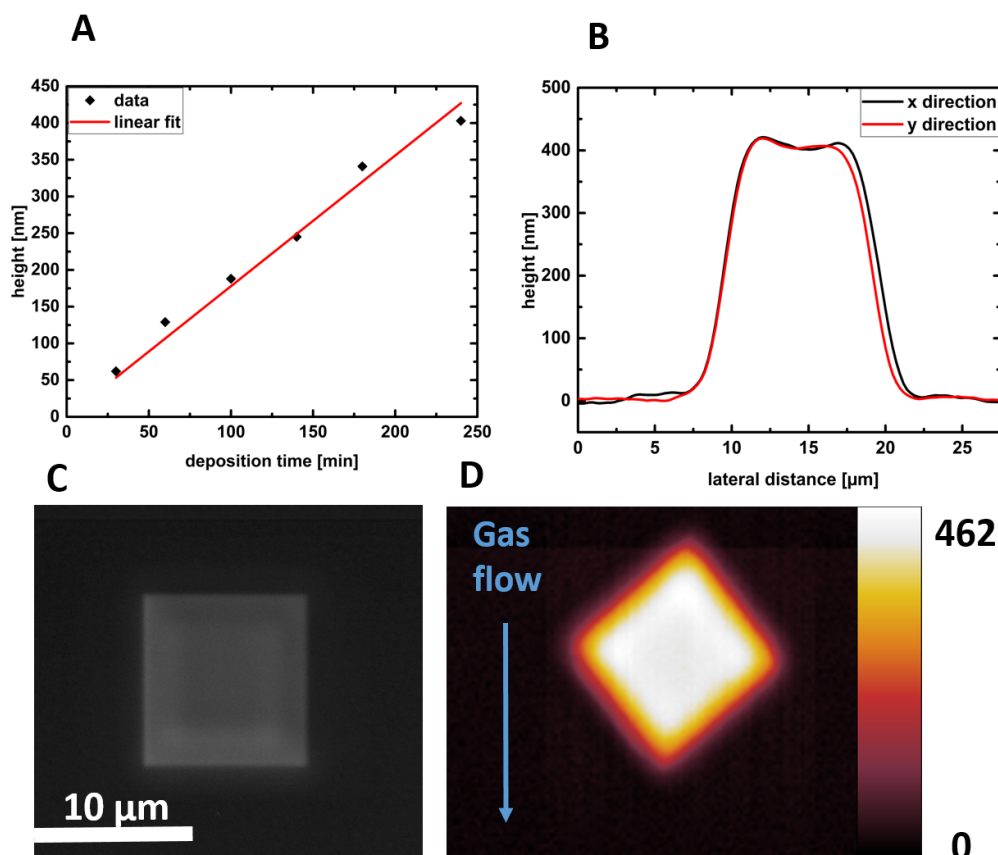


Figure 3.13: A) Height of EBID pads for different deposition times, a dwell time of 1 μs and a point distance of 3 nm. B) Atomic force microscope line scans of one EBID pad. C) Scanning electron micrograph of an EBID pad. D) Atomic force micrograph of the same pad.

to planar copper deposits with resistivity as low as $1.67 \mu\Omega\text{cm}$ and copper content around 74 at.%. The study of the sublimation of the precursor [117] shows a start by a temperature above 90°C . To achieve a stable precursor flow the temperature had to be chosen above that point. On the other hand a low temperature is wanted in EBID to avoid any CVD process during the growth. For all the experiments the temperature of the reservoir is set to 100°C . For substrate temperatures below 90°C condensation of the precursor on the substrate is observed, figure 3.12). Thus the temperature is set to 100°C .

Deposition and growth rates The deposition mechanism has been investigated by x-ray photoelectron spectroscopy and Auger electron spectroscopy for the $\text{Cu}(\text{I})(\text{hfac})(\text{vtms})$ [118]. The main decomposition path was found to be a dissociative electron attachment (DEA) process with

a threshold of 4 eV. For the precursor examined in this work no dissociation path has been studied so far. In the case of CVD the suggested path is a pyrolysis mechanism where CO₂ is realized during the process. For calculating the deposition rate of the novel precursor, pads with different deposition times are fabricated and their height measured by atomic force microscopy, figure 3.13. The deposition current is measured to be 7 nA. Other deposition parameters are 15 keV energy, 10 μs dwell time, 3 nm pitch distance and the number of scans increase from 30 to 300. The chamber pressure during the deposition was around 5·10⁻⁴ mbar. The chamber pressure drops to 5·10⁻² mbar the first time the valve to the precursor chamber is opened at 100 °C. Most likely due to the release of water absorbed by the crystal precursor. After the normal pressure is restored, opening and closing the valve do not lead to any measurable pressure change in the vacuum chamber, suggesting a vapor pressure below 5·10⁻⁴ mbar. The square pads have an edge length of 10 μm. The volume of the pads were calculated by the pad area (100 μm²) multiplied by their height measured in the middle of the pads. By this the high edges of the pad as well as the not perfectly sharp sides are neglected. With this the volume deposition rate (R) is

$$R = 0.026 \frac{\mu m^3}{nA \cdot min},$$

which is comparable with the deposition rate of common platinum precursors [101]. The AFM image reveals the top edge of the pad being higher than the point in the center, having an indented shape. This indicates a precursor limiting growing regime, where the middle of the scanning are becomes depleted and though the deposition rate decreases [6, 119]. Also noticeable is the shoulder pointing towards the direction of the gas flow is slightly higher than the one at the opposite site, originating from a different precursor supply [120].

Nanostructuring One big advantage of EBID is its ability to fabricate complex three dimensional nanostructures by utilizing the small interaction volume of the electron beam with the substrate. The simplest nanostructure can be produced by spot mode irradiation. Figure 3.14 A shows a fabricated EBID pillar with a diameter of 100 nm and a height about 1.5 μm and a deposition time of 60 seconds grown at a current of 0.05 nA. The estimated volume deposition rate from the nanopillar is $0.0047 \frac{\mu m^3}{nA \cdot min}$. Comparison of the deposition rate of the planar structures and the nanopillar reveals a strong decrease in deposition rate of about one order of magnitude. A possible explanation for the difference is the change in molecular supply when depositing planar structures compared to nanostructures. While in the latter case the molecules are dissociated at one point, leading to a strong molecular limited regime. In the case of planar structures there exist a certain time until the same point is irradiated again. Even though the deposition current for the planar structures are much higher compared to the nanopillars. Another effect, in the case

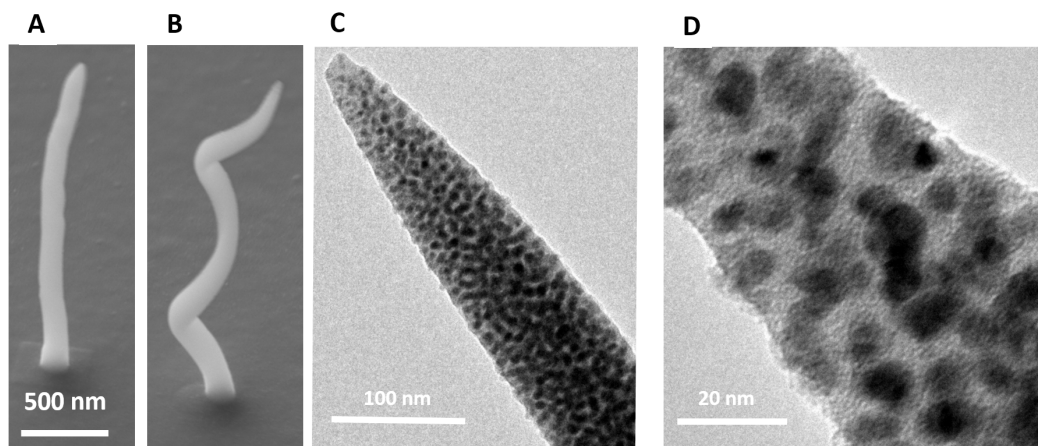


Figure 3.14: A) Electron micrograph of a single nanopillar deposited on glass covered with 50 nm ITO. B) Copper helix with three pitches. C, D) Transmission electron micrographs of a copper pillar. Visible is the typical EBID structure, copper particles embedded in an amorphous carbon matrix

of high nanopillars is that the molecules have to diffuse to the top for further vertical growth. Taking that into account the growth rate value for the pillar is just an averaged growth rate for the specific height of 1.5 μm . The growth rate of the nanopillar tip in comparison with known copper precursor from literature [116], shows a slightly higher tip growth rate of 50 nm / sec. The helix in figure 3.14 B is deposited with a circular pattern with radius of 120 nm, a point to point distance of nominal 0.5 nm and a dwell time of 30 ms. The total deposition time of the helix is 2 min.

3.3.2 Structural properties of EBID-copper

In the TEM images in figure 3.14 C and D the typical structure of EBID material is visible. The dark dots are copper particles embedded in an amorphous carbon matrix visible in light. From the high resolution TEM the size of the particle can be estimated to have a diameter about 10 nm. Often EBID material suffers from a high carbon content especially when using organic precursors. The metal content can be about 8 or 15 at.% for organic gold and platinum precursor respectively [121]. By EDX, it is difficult to determine the absolute percentage values of the constituents of the EBID material since light elements like oxygen and carbon are difficult to quantify. For better comparison the peak ratios from copper to oxygen and carbon are plotted in table 3.1, as well as the EDX spectra of a copper foil with a high purity (> 99,999 %) 3.15. As expected the peak ratios of pure copper show very high values, with just traces of oxygen and

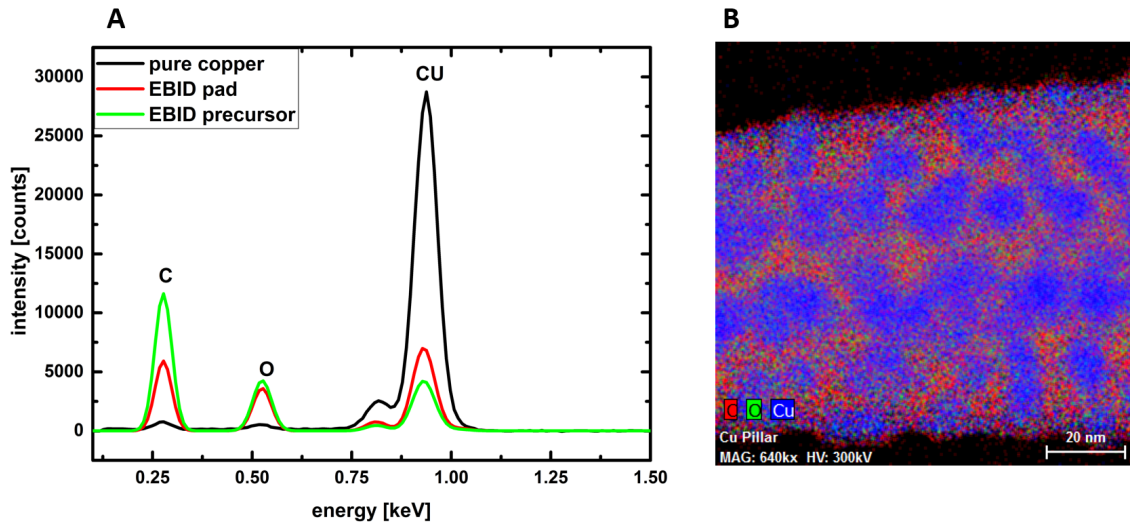


Figure 3.15: A) EDX spectra of the solid crystalline precursor, a copper foil with a purity > 99,999 % and an EBID pad grown on a silicon substrate with a height of 400 nm. B) EDX mapping of the elements oxygen, carbon and copper from an EBID pillar taking in a TEM.

peak ratio	pure copper	EBID pad	EBID precursor
Cu/O	38.7	1.9	0.9
Cu/C	54.2	1.2	0.4
at. %			
Cu	97	24	11
O	1	24	23
C	1	51	66

Table 3.1: Peak ratios from EDX measurements on EBID an pad, pure copper and the copper precursor.

carbon which most likely result from residual gases in the vacuum chamber. To determine the composition of the precursor is even more critical because the precursor decompose during the measurement by the impact of the electron beam. Calculation from the chemical formula gives a composition of 4 at.% Cu, 26 at.% O and 70 at.% C. The measured copper content is 7 % above the calculated value from the formula, likely due to the decomposition. The spectrum of the EBID pad shows no signal from the silicon substrate therefore all signal originate from the EBID pad itself. The measurement shows a high copper content of 24 at.% with is a large increase to the pure precursor. The spectrum also propose that mostly carbon is removed during the deposition process while the oxygen content stays constant within the reliability of the measurement. In the EDX mapping in 3.15 B of an EBID pillar the common EBID structure of metal particles embedded in an amorphous carbon matrix is confirmed. The oxygen signal in the mapping is

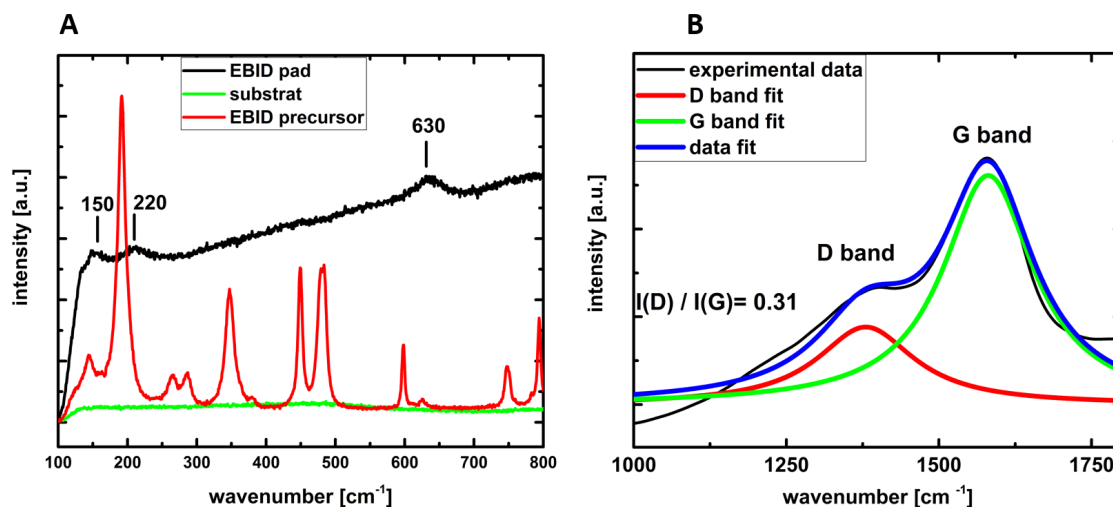


Figure 3.16: A) Raman spectra of an EBID pad, EBID precursor and the substrate. The complex structure of the precursor develops into a broad spectrum, typical for amorphous material. Indicated are three Raman lines for Cu_2O [122] corresponding well with the measured spectrum. B) Raman features of the amorphous carbon matrix in the EBID material.

visibly mostly in the areas of the matrix but not absent in the copper particles, hinting to partial oxidized copper. This assumption is later in this thesis further supported by the Raman spectrum of a deposited pad. Since the material composition of EBID material changes with the deposition parameters the EDX signal from nanostructures is expected to exhibit a different composition than planar deposits. During the EDX measurement on single nanopillars in a TEM a strong signal from the substrate was always visible which makes the analysis difficult. The average EDX signal from 8 nanopillars gives an composition of 26 at.% Cu 13 at.% O 61 at.% C. This shows a low increase in copper and carbon content compare to oxygen. To come to a better understanding of the material configuration and change during deposition Raman spectroscopy measurements are performed on EBID pads as well as on the precursor before deposition. The Raman spectrum in figure 3.16 A of the precursor shows a complex structure with a number of distinct peaks. Under the impact of the electron beam the spectrum changes to a broad Raman response typical for amorphous materials. The diverse feature of the material before and after EBID suggest a complete break of all bonds present in the crystalline structure. The three small peaks visible in the deposited EBID pad at 150, 220 and 630 nm suggests a partial oxidized copper state in the copper particles [122]. This is important in view of the dielectric function of the resulting material since the permittivity depends on the oxidation state. In figure 3.16 B is one larger peak around 1580 cm^{-1} and one minor peak around 1350 cm^{-1} visible. These can be attributed to the amorphous carbon of the EBID material. These peaks are referred to as D for disordered and G

for graphite peak [120]. The intensity ratio of the D to G peak is a measure of the amorphization state of carbon. The low value of 0.3 for the EBID carbon as well as the G-peak position of 1580 cm^{-1} hints to highly amorphous carbon [82]. In comparison to the platinum precursor the lower D to G ratio and the G-peak position and higher wavenumbers indicate that the carbonaceous structure is different for the EBID-copper material compared to the EBID-platinum. The lower peak ratio indicates a larger ratio of amorphous carbon to crystalline graphite.

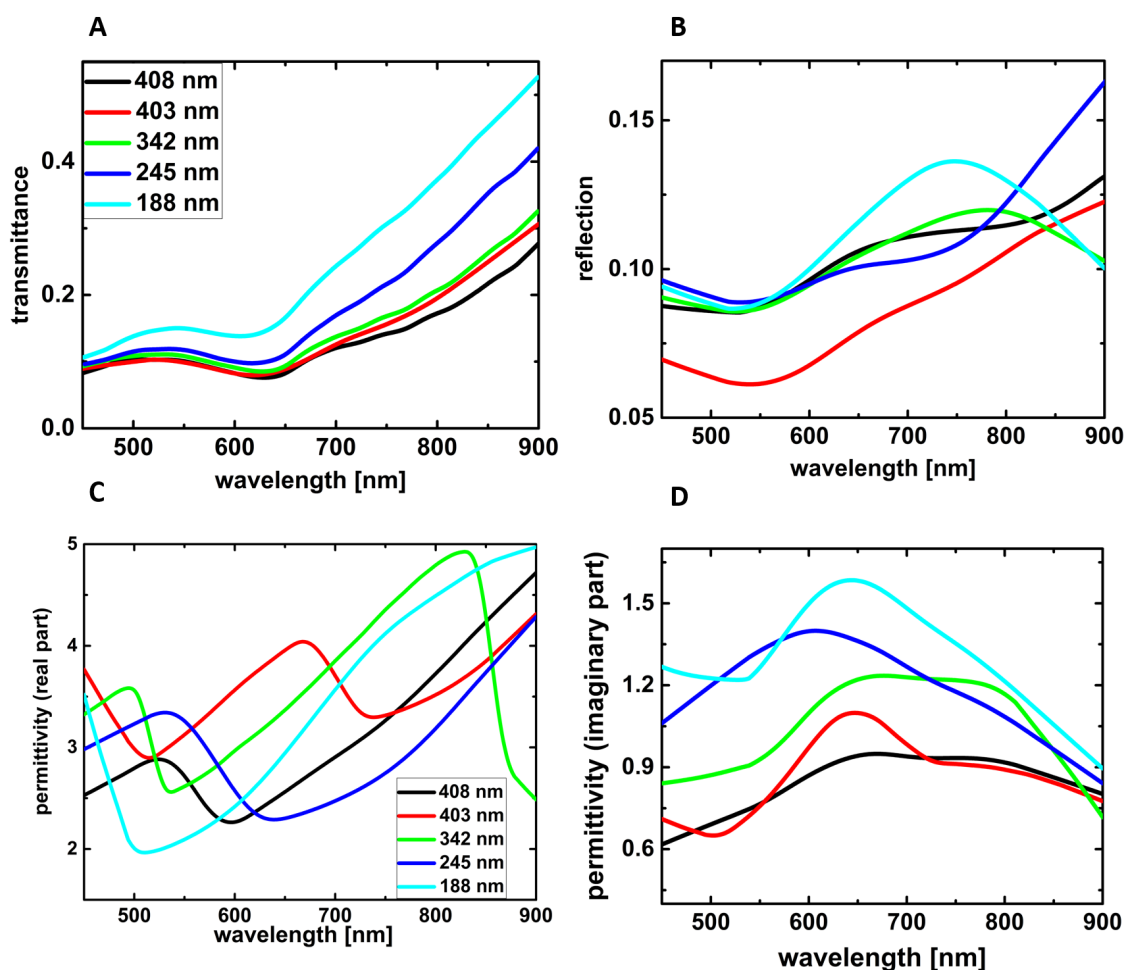


Figure 3.17: A, B) Measured transmission and reflection of EBID pads for five different heights. Retrieved real C) and imaginary D) part of the permittivity for each pad.

3.3.3 Permittivity of EBID-copper: Optical measurements and a model

Permittivity from transmission and reflection To determine reliably values for the optical response of EBID fabricated material is difficult due to the long deposition times for large areas. This makes standard measurements like ellipsometry very time consuming or even unrealistic. To find the permittivity values for the invested copper precursor the same method as in reference [36] is used. The reflection and transmission of EBID pads with a side length of $10 \times 10 \mu\text{m}$ deposited on a glass substrate covered with a 50 nm layer of ITO and a brute force algorithm is used to retrieve the optical constants. The measured transmission and reflection curves together with the permittivities for five different pad heights are plotted in figure 3.17 A and B. The transmission measurements show an almost flat dependence in the wavelength range up to 600 nm,

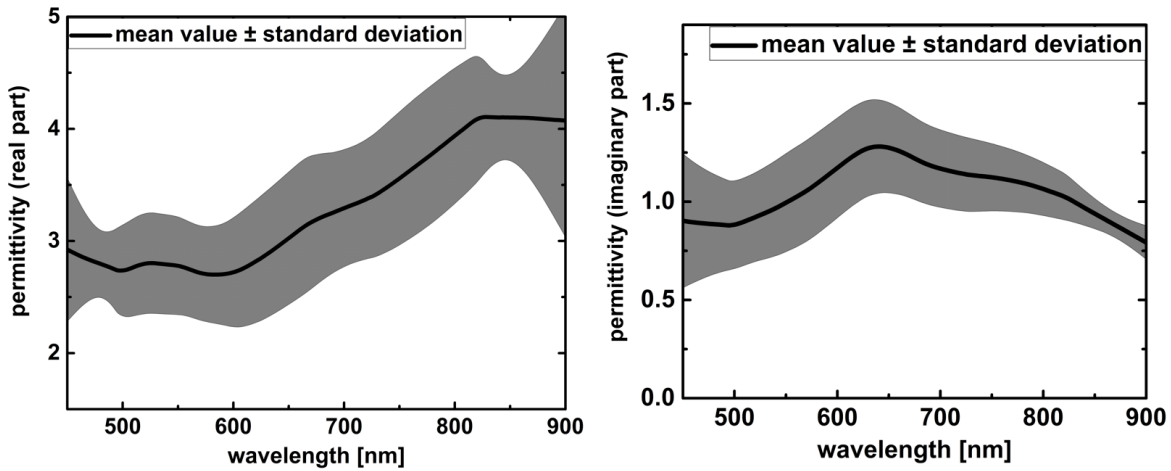


Figure 3.18: Averaged real A) and imaginary B) permittivity for the five EBID-copper pads, together with the standard deviation of the five pads.

followed by a linear increase. While the reflection is below 20 % for all measured pads it shows slightly different behavior for different thicknesses. At about 750 nm a peak for the pad with a thickness of 186 nm is visible which could possibly originate from a resonant mode, where the pad height is roughly one quarter of the wavelength. All pads show a dielectric behavior with a positive real part of the permittivity for all wavelength. Thus also for the copper precursor with a higher metal fraction than the platinum precursor the optical properties are to a great extent determined by the carbonaceous matrix.

The permittivities of the individual pads show a large variation. However, direct correlation between the pad height and the permittivity could not be found. The different deposition times could lead to different material compositions, as seen for the platinum deposits. In the case of a nanopillar the composition is not uniform throughout its height [77]. Another explanation is a different configuration of the copper crystals or the carbon matrix. Belic et al [68] found a growth in crystal size for a gold precursor under electron irradiation. While the change in carbon configuration for different deposition parameters is not well known it has been shown that a post heating step is changing it to a great extent [88]. In comparison the deposits of the platinum precursor showed a clear trend to higher metal content and higher degree of graphitization with higher pads. If the difference for the deposits of the copper precursor is due to another height range of the pads or another precursor is not clear yet. Figure 3.18 shows the averaged permittivity of the five copper-pads together with the standard deviation. This shows a clear trend of an increase in the real part of the permittivity from 3 to 4 with increasing wavelength. The imaginary part shows a maximum around 550 nm, which could correspond to a Mie resonance of copper particles in the carbon matrix.

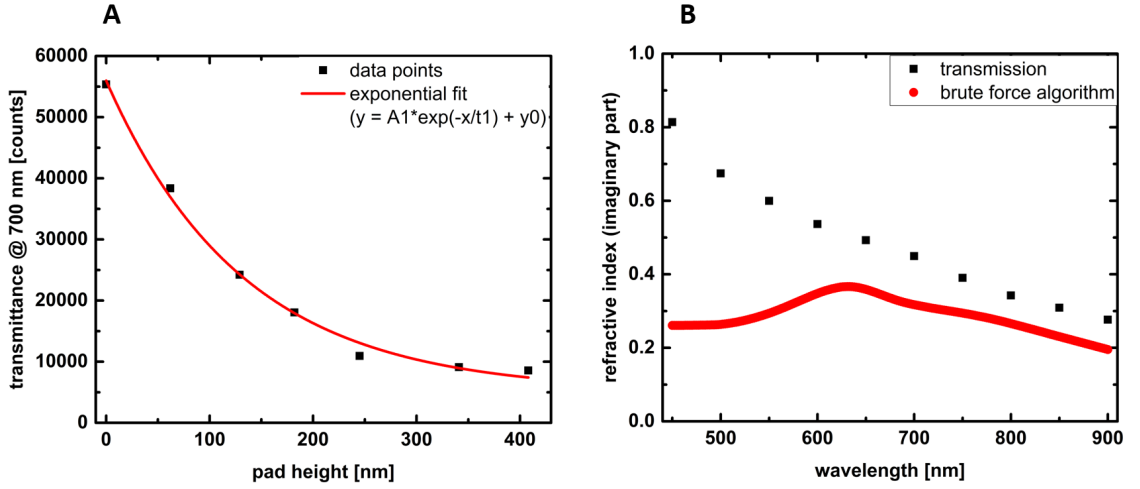


Figure 3.19: A) Exponential decay of light intensity versus layer thickness of EBID pads. B) Comparison of the imaginary part of the refractive index determined with the brute force algorithm and with the transmission measurements using formula 3.1.

Attenuation factor from transmission measurements There is another way to evaluate the transmission data and determine the imaginary part of the refractive index and by this verifying the data from the brute force algorithm. In this method the following formula is used to link the absorption of light by traveling through a media with the imaginary part of the refractive index

$$a = \frac{4\pi\kappa}{\lambda}. \quad (3.1)$$

To determine a the transmission at one wavelength is plotted against layer thickness and fitted with an exponential decay. The resulting exponential decay factor is set into equation 3.1 to calculate the imaginary part of the refractive index. There is a systematic error when using this method because the multiply reflection between the surfaces are not taken into account. But it provides an approximation of the magnitude of a and can be used to verify the brute force algorithm. The transmission measurements are done from the direction of the substrate. Thus the same intensity impinging on the different EBID pads. The value at thickness 0 nm corresponds to the transmission of the substrate far away from the deposited EBID pads. At higher wavelength the two method give similar results while at wavelength below 600 nm the brute force algorithm shows a decrease while the values determined from 3.1 shows a steady increase.

Maxwell-Garnett model for EBID-copper The MG model is used to calculate the permittivity from EBID-copper. The input parameters for the MG model are the permittivities of the

components and their volume filling fraction [24].

$$\epsilon_{MG} = \epsilon_C \frac{\epsilon_{Cu} + 2\epsilon_C + 2f(\epsilon_{Cu} - \epsilon_C)}{\epsilon_{Cu} + 2\epsilon_C - f(\epsilon_{Cu} - \epsilon_C)} \quad (3.2)$$

f is the volume filling fraction of the copper inclusion. The MG theory distinguishes between a background medium and the inclusions. Due to the higher content of carbon, it is set as background medium. The EDX measurements gives an atomic composition of the material. To estimate if the volume composition differs from the atomic composition the molar volume density has to be calculated. The EBID-copper consists of carbon, oxygen and copper. The density of carbon varies depending on the configuration and a value for pure oxygen gas is not useful and here neglected. The values from [123] for copper and amorphous carbon leads to the following molar volume:

$$\frac{V}{mol} = \frac{\text{molar density}}{\text{volume density}} \quad (3.3)$$

	copper	carbon
volume density	8.96 g/cm ³	1.95 g/cm ³
molar density	63.5 g/mol	12.1 g/mol
molar volume	7.1 cm ³ /mol	6.2 cm ³ /mol

Table 3.2: Molar densities of amorphous carbon and copper. Data are taken from [123].

The estimated molar volume of copper is only slightly above the value for amorphous carbon, suggesting that also the volume fractions just varies little from the atomic fractions. A big uncertainty in modelling the dielectric function of the EBID-copper is the influence of the large portion of oxygen in the deposits. Thus the material is no simple mixture of two pure elements. Especially, since carbon already by itself occurs in many configuration with very different properties. An analytic formula for the MG equation can just be given in the case of two phases. To approximate the dielectric function of the EBID-copper material the values for copper [20] is used, even though the EDX measurements showed a weak oxygen signal from the copper spheres and the Raman measurement gave a small signal from Cu₂O. Due to the small signals it is assumed that the main portion of the copper inclusions are of unoxidized. For the carbon matrix the Raman spectrum showed a highly amorphous carbon phase. The values for amorphous carbon from Hagemann et al. [90] are used, while the large oxygen content is not taken into account. Figure 3.20 shows the results from the MG theory of EBID-copper for three different copper concentrations. While the real part well resembles the measurements the imaginary part shows lower values. This suggests that the permittivity values assumed for the carbon phase

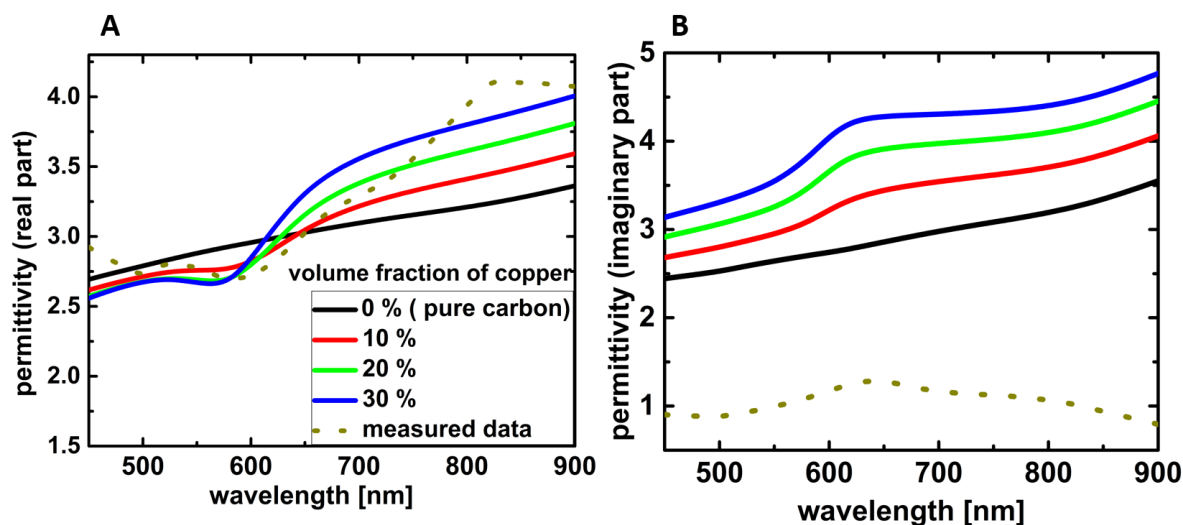


Figure 3.20: A) Real and B) imaginary part of the Maxwell-Garnett model. The model uses the dielectric function of copper from [20], and of carbon from [90].

are too high. A possible reason is the high oxygen content. Measurements on hydrogenated carbon with different oxygen contents have been shown that the refractive index is significantly decrease with increasing oxygen [92, 124]. The real part of the measured permittivity is close to the one for pure carbon. Thus the copper inclusions just play a minor role in the permittivity of the effective medium.

3.3.4 Plasmonic scattering by EBID-copper

The retrieved values for the permittivity of the five as-deposited EBID-copper pads showed a large variation and have been averaged in figure 3.17. To test if the mean value can be used to simulate the optical properties an array of 8×8 nanocones with a distance of 400 nm and a base diameter of 80 nm is fabricated, figure 3.21 A. It is measured by darkfield scattering spectroscopy and compared to FDTD simulations. Figure 3.21 B shows the measured and simulated scattering intensity. The as-deposited structures exhibit a resonance around 550 nm. The simulation with the retrieved permittivity resembles the resonance of the as-deposited cones. However, the measurement show a steeper decrease with increasing wavelength than simulated.

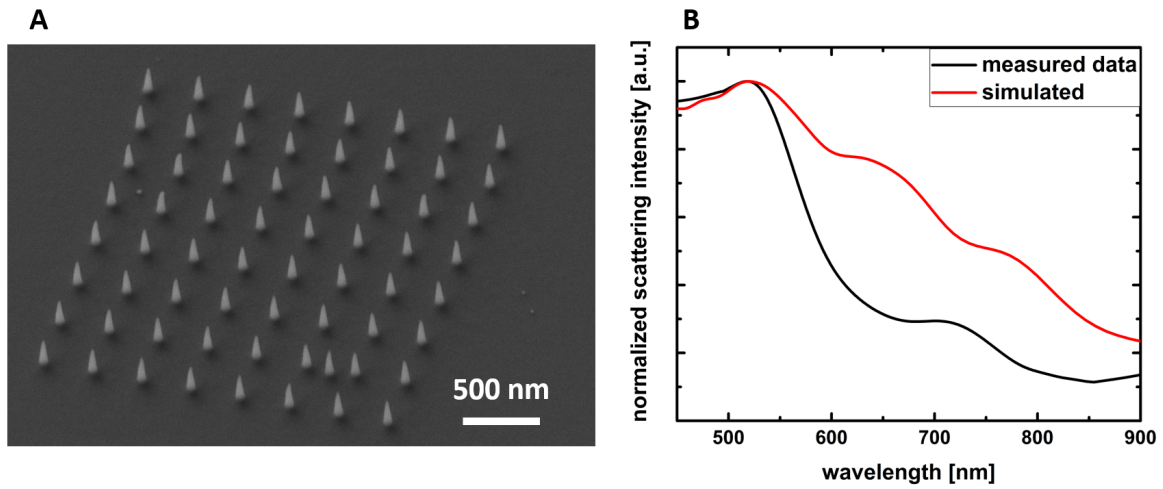


Figure 3.21: A) Array of 8 x 8 nanocones with a distance of 400 nm, base diameter of 80 nm and a height of 250 nm. B) Measured and simulated scattering spectra of the array.

4 Coating EBID nanostructures: From PVD to ALD

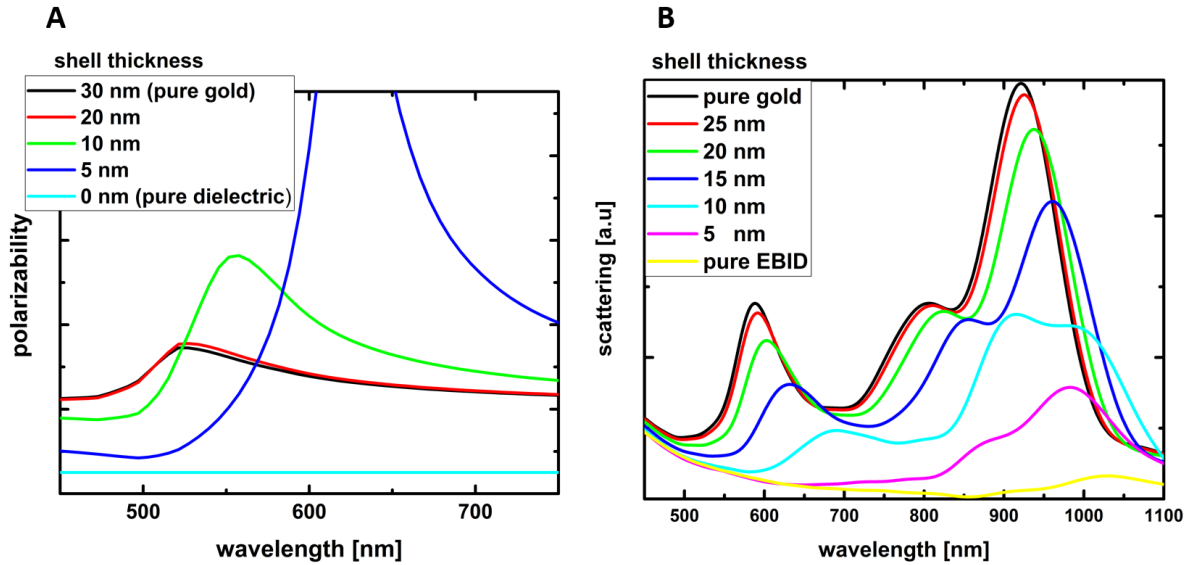


Figure 4.1: A) Extinction cross-section of a dielectric sphere ($\epsilon = 2$) with a radius of 30 nm coated with different thick gold layers from 0 nm (pure dielectric) to 30 nm (pure gold), calculated with equation 4.1. Data for gold are taken from Johnson & Christy [20]. B) Simulated scattering intensity of a three pitch helix ranging from pure EBID to pure gold examine the influence of different thick gold shells. EBID values are taking from [36] of the thinnest pads. Values for gold are taken from [20].

Despite the high resolution that can be achieved by electron beam induced deposition including the possibility to create truly three-dimensional nanostructures current applications in plasmonics are rather limited. The most important reason for this is the low metal content in the material and the consequently poor plasmonic response. To be able to explore the advantages of the flexibility of EBID fabrication for plasmonic it is necessary to find a way of improving the optical response without altering the high precision geometric features. A possible way is to use a two-step fabrication method in which the first step defines the geometry of the structure by EBID while the second step covers the EBID structures with a pure metal layer. This two step process has the advantage to be able to optimize the precursor and deposition parameter used for EBID independently from the coating process. In general the theoretical description of these core-shell structures becomes more complex because two different materials and their interfaces have to be considered. A core-shell structure can be described with a hybridization model in which plasmons are excited on the inside and the outside of the shell. These plasmons form a coupled state[125]. Yet, calculations of the scattering cross-section of the individual outer and inner plasmon reveals the dominance of the outer one for shell thicknesses around 20 nm in the

case of gold [126]. In the simply case of a coated sphere in the quasi static limit an analytic expression for the polarizability (α) is given by: [29]

$$\alpha = 4\pi r_2^3 \frac{(\epsilon_s - \epsilon_m)(\epsilon_c + 2\epsilon_s) + f(\epsilon_c - \epsilon_s)(\epsilon_m + 2\epsilon_2)}{(\epsilon_s + 2\epsilon_m)(\epsilon_c + 2\epsilon_s) + f(\epsilon_c - \epsilon_s)(2\epsilon_m - 2\epsilon_s)} \quad (4.1)$$

In this equation r_2 is the radius of the whole sphere and f the ratio of the radii of the inner and outer sphere ($f = \frac{r_1}{r_2}$). The polarizability depends on the dielectric functions of the core (ϵ_c), the shell (ϵ_s) and the surrounding medium (ϵ_m). It further depends on the radius of the inner r_1 and outer sphere r_2 . The skin effect of the metal shell allows the electromagnetic wave just to penetrate several nanometers inside the structure. Thus exciting the outer plasmon more effectively. Figure 4.1 A shows the minor difference of the polarizability of a pure 30 nm gold sphere and a core-shell structure of a 10 nm dielectric core with a 20 nm gold shell. The plots are calculated by evaluating equation 4.1, taking the surrounding medium to be vacuum, a dielectric core with a constant permittivity value of 2 and a gold shell with the material data from [20]. A metal shell also determines the scattering properties of more complex structures. In figure 4.1 B the scattering intensity for a helix with three pitches is calculated by the FDTD solver Lumerical. The radius of the helix wire is assumed to be constant with 30 nm while the EBID core is changed from 0 nm (pure gold) to 30 nm (pure EBID). The material properties of gold are taken from [20] and the material properties of EBID are taken from [36]. The graph shows no major changes for layer thicknesses above 15 nm. The weak influence of the core is not changing when taken other dielectric materials like silicon or air as core material. The common influence of a dielectric core in the case of the coated sphere and the helix is a resonance shift to higher wavelength. The same occurs if a metal particles is placed into a dielectric medium. Though in the case of a core-shell structure with a gold shell around 20 nm, the influence of the core can be simplified as an effective surrounding medium, without taken the hybridization model into account. Additionally the resonances of the helix are damped with an increase core thickness which is the opposite effect that occurs with a gold sphere placed inside a dielectric.

The major influence of the metallic shell promotes the idea that plasmonic structures with an EBID core can be used for plasmonics and show comparable performances as pure metals. A possibility to cover EBID deposits is to use physical coating techniques like sputtering or evaporation. This methods allow for an easy and fast coverage of different kinds of materials. In this thesis electron beam evaporation is used to cover EBID-gold helices with a 20 nm layer of pure gold. For this three-dimensional structures the sample has to be tilted and rotated during evaporation to achieve a uniform layer thickness on all sides. Nevertheless, when covering complex three-dimensional structures or arrays with elements close to each other, a shadowing effect is expected, where the structures have differently thick layers of metal on different sides. One

example in literature where the combination of EBID growth plus a metallic shell was used was in the fabrication of high aspect ratio nanoantennas, using a silicon containing precursor. These vertical nanorod antennas were covered with a layer of pure gold sputtered onto the structures after fabrication [127]. The rods were then investigated by cathodoluminescence. In this study, the influence of the core on the effective refractive index is still visible even at a layer thickness of 30 nm. Even though also in this case the influence of the core seems to decrease for increasing shell thickness the effect is still larger than in the calculated examples of a coated sphere and a coated helix. The reason is likely due to the different excitation methods. Considering light as the source of excitation the field is damped when penetrating the material. While electrons accelerated with 30 kV, [128] are penetrating the whole nano-antenna and though also exciting the plasmons on the inside of the metal dielectric interface directly.

4.1 EBID helices with a pure gold shell by physical vapor deposition (PVD)

Helices with sizes in the nanometer range can be fabricated by EBID but the material composition is not of pure gold but a carbonaceous matrix with gold inclusions. EBID-gold helices with three pitches are fabricated by EBID as described in chapter 3.2.2. In a second step a 20 nm thick pure gold layer is added by electron beam evaporation. Therefore, the sample is tilted to 90 degree and rotated to achieve a nearly uniform thickness on the structure.

4.1.1 Darkfield scattering of a single helix

Darkfield scattering spectroscopy is used to compare the plasmonic properties of as-deposited EBID-gold helices and core-shell helices with an EBID core and a plasmonically active pure gold layer. In comparison to most studies on EBID helices [78, 128, 129], where arrays of helices were studied, this thesis focuses on the properties of single plasmonic helices. In an array the local currents induced in the respective helices influences the neighboring ones which lead to a strong resonance shift in the infrared region [130]. By investigating single helices all effects which originate from the interaction of different helices in an array can be ruled out. Figure 4.2 shows a scanning electron micrograph of a single as-deposited helix with three pitches (A) and with an additional pure gold layer of 20 nm (B). The external diameter of the helix is 180 nm with an wire thickness of 65 nm (including the pure gold layer) and an averaged vertical pitch of 220 nm. In figure 4.2 C the darkfield scattering spectra of both helices are plotted. The graph shows the low broad scattering spectrum of the as-deposited helix changes into a spectrum with stronger signal, which shows two distinct resonances around 600 nm and 950 nm. To analyze the

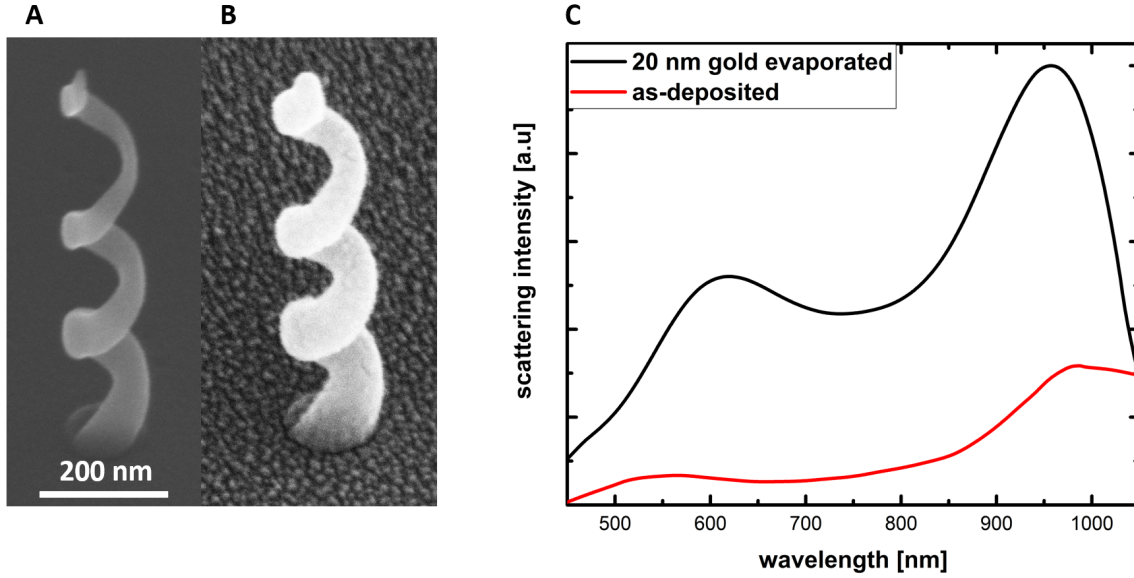


Figure 4.2: Helix with three pitches A) as-deposited and B) covered with a 20 nm layer of pure gold respectively. C) Darkfield scattering spectra of both helices.

resonances of a single gold-helix it is convenient to start at the resonance of a single gold sphere. According to Mie theory a small gold sphere supports a resonance around 550 nm [11]. This single resonance of a gold sphere splits into two resonances in the case of a nanorod [131]. A transverse mode for the polarization of the exciting light parallel to the short side of the nanorod and a longitudinal mode for the polarization parallel to the long side of the pillar [131]. In analogy to this an effective rod length can be assigned to the helix. The length of the rod is calculated by the arc length of the helix [132]

$$l_{\text{arc}} = N_{\text{Pitch}} \sqrt{\pi^2 d^2 + h^2}. \quad (4.2)$$

N_{Pitch} is the number of pitches, d is the external diameter and h is the height of one pitch. Discrete dipole approximation (DDA) calculations on a silver helix showed oscillating charges along the helix wire [132]. These oscillations result in a number of dipoles, with an effective dipole length of approximately half the arc length of one pitch. More precise in the case of a helix with three pitches $3/8$ of a single arc length. Thus the effective length does not strongly depend on the number of pitches, but the height of a single pitch and the radius of the helix. Figure 4.3 A shows the calculated scattering intensities of a gold nanorod with a radius of 35 nm and three different heights. Clearly visible is the appearance of the transversal and longitudinal mode for the two polarizations. The spectral position of the resonances coincide approximately with the observed resonances of the helix. In Figure 4.3 B the effective length of a helix with three pitches is plotted for different pitch heights and diameters of the helix. The increase of both diameter and pitch

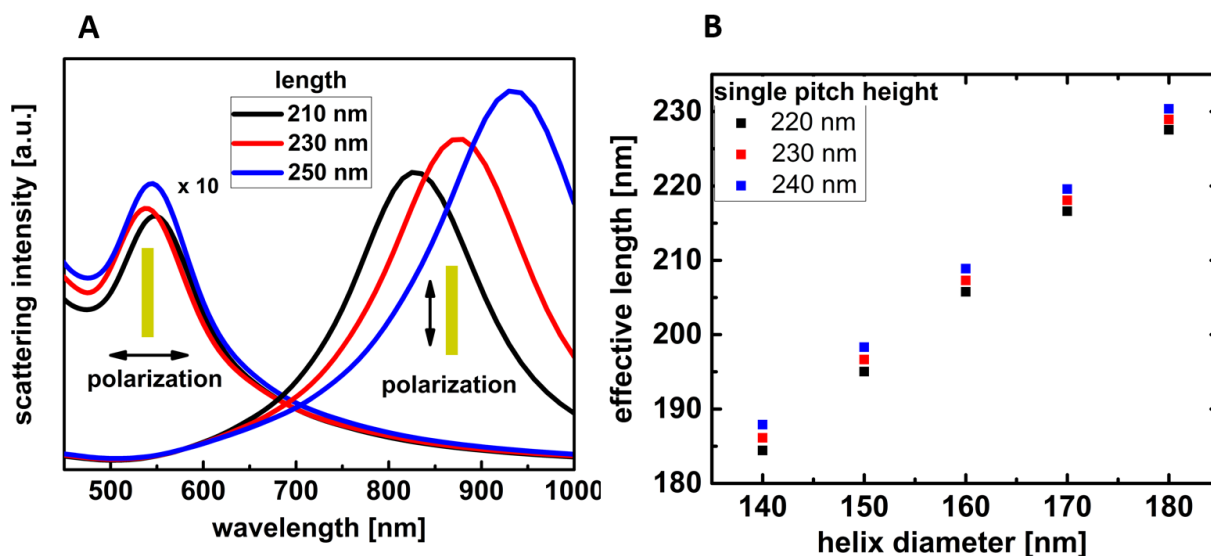


Figure 4.3: A) Scattering spectrum of a gold nanorod for two polarizations. B) Effective length of a helix for different pitch heights and diameters.

height increase the effective length. However, the influence of the diameter is much stronger. This model explains the minor influence of the number of pitches on the spectral position of the maximum dissymmetry, observed for core-shell gold helices [133].

4.1.2 Dissymmetry transmission measurement and simulation

In reference [103] (see also section 3.2.2) it has been shown that already the as-deposited EBID-gold helices show a dissymmetry in the visible spectral range. However, the signal from a single helix is very low. The scattering intensity of a helix could be well improved by adding a layer of pure gold onto the EBID material. The pure metal supports the oscillations of electrons in contrast to the dielectric as-deposited EBID material and thus displays a more pronounced spectrum and an increase in scattering intensity. Since the height of the dissymmetry value has its origin as well in the capability of the helix to support plasmons it is expected that the additional pure gold layer will also improve the dissymmetry factor. As circular polarized light is equivalent to a superposition of two orthogonal linear polarized light beams with a phase difference of ± 90 degrees, it is expected that the maximum of the dissymmetry factor should occur at the positions of the resonances of the scattering experiment [134].

The darkfield scattering spectrum of the gold covered helix supports two resonances, one in the visible spectral range around 600 nm and the other in the near infrared region around 950 nm. The origin of the two resonances can be explained by the effective dipole approximation. In this

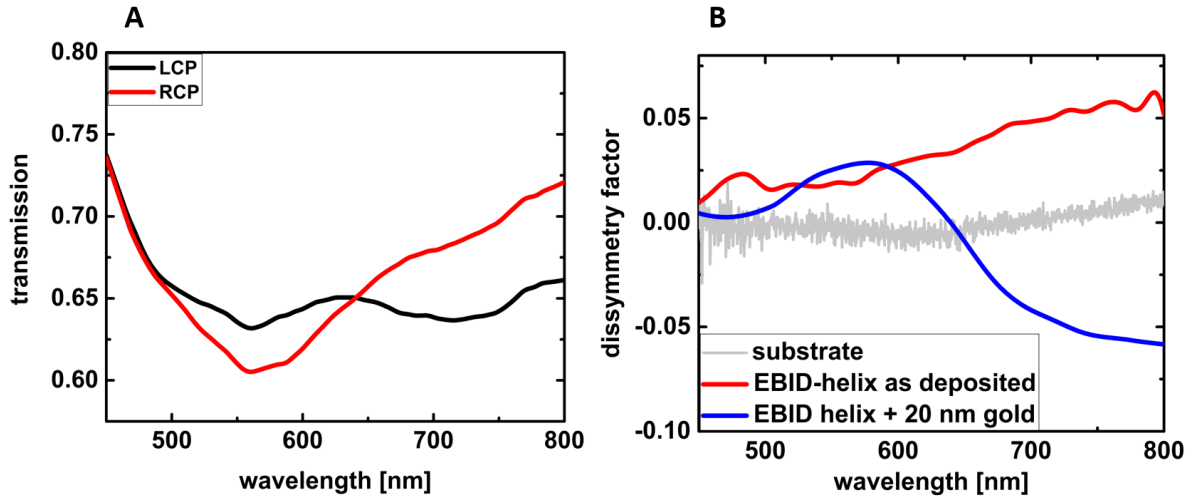


Figure 4.4: A) Transmission of right-circularly polarized and left-circularly polarized light through a single EBID-gold helix evaporated with a 20 nm layer of gold. B) Dissymmetry factor of the helix. As comparison the dissymmetry factor of an as-deposited helix [103] is also plotted in the graph (red line). The green line shows the background signal from the substrate.

the helix is treated as a nanorod with an effective length of approximately half the arc length of one pitch. However, one feature of helical structures is their sensitivity to the circular polarization state of light [135]. This sensitivity was first shown for the case of pure gold helices, fabricated by direct laser writing with sizes in the μm range [135]. These exhibit a contrast in transmission in which light of opposite handedness as the helix is transmitted while the other polarization is reflected. In this size range of the helices the operation wavelength was in the infrared region. The authors stated that the system can be tuned to lower wavelengths by miniaturization of the structure, as long as the operating frequency is below the plasma frequency of the metal [135].

An intuitive picture of the origin of circular dichroism (CD), defined as the difference in absorption between left- and right circularly polarized light, is given by the Born-Kuhn model for plasmonic structures [136]. This model accurately describes the origin of the CD signal for two vertical separated gold nanorods in a L-shape configuration. Resonances occur at those wavelengths, where the rotating electric field vector, aligns with both nanorods. This occurs at different wavelength for left- and right rotating fields. Even though the situation is different for a helix, because the whole structure is connected, the model shows the generally expected shape of a CD spectrum with a positive and negative part, which corresponds to symmetric and anti-symmetric excitation of the nanorods. Also the optical rotation of linearly polarized light with its maximum value at the position of zero CD is reflected by the model.

A dipole model [134] gives a more general explanation for the CD of chiral structures. The model

describes circularly polarized light as a series of dipoles aligned in the direction of propagation of the light and rotated according to the handedness of the light. The excitation of the structure occurs at points where the orientation of the dipoles fits with the orientation of the structure. This explanation has been used to interpret the results for truly three dimensional EBID helices [13]. Here, the individual pitches were described as unit cell which exhibit resonances according to the appropriate alignment of dipoles. The CD signal from the helix finally results from the hybridization of the respective pitch resonances [135].

Arrays of EBID helices with a silicon core were covered with pure gold by physical sputtering. These have been shown to exhibit a strong difference in absorption respective to the circular polarization in the visible range [128]. The helical arrays showed a maximum in the transmission difference between left- and right circular polarized light around 700 nm. Variation in the height of the helix showed an increase in optical activity with larger height while at the same time the position of the resonance stayed almost constant [133].

Figure 4.4 displays the difference in transmission of left- and right-circularly polarized light through a single EBID-gold helix with a 20 nm thick pure gold layer. The pure gold layer is added by e-beam evaporation on a rotating sample with a tilt of 90 degrees. The overall transmission is above 60 %. The minimum in transmission for the RCP is around 550 nm. In figure 4.4 B the dissymmetry factor of the same helix is plotted, where the as-deposited helix is added for comparison. The dissymmetry factor shows a more pronounced peak with the additional layer of gold onto the EBID helix. In the case of the helix with a pure gold shell the dissymmetry factor shows a maximum value around 600 nm.

A numerical investigation of metal helices revealed that the influence of the height of the helix is of minor importance while the resonance position does shift linearly with the radius [130]. The negligible influence of the pitch height on the spectral position of the dissymmetry was shown for EBID helices covered with gold [133, 137]. The same behavior is found in this thesis by increasing the number of pitches from three to five. For different pitches the position of the maximum value does not significantly shift. The maximum around 600 nm correspond to the lower wavelength resonance position observed in the darkfield scattering spectrum. Unfortunately, the setup does not allow for the dissymmetry measurement in the infrared region. Thus the selectivity on circularly polarized light of the second resonance can so far not be verified by measurement. Simulation of a pure gold helix shows the dependence on the circular polarization state of light also for the long wave resonance. Figure 4.5 shows the simulated transmission of right- and left circularly polarized light and the resulting dissymmetry factor. The lower wavelength part, which is accessible by our measurement setup, shows good agreement with the measurement. The first maximum of the dissymmetry is reproduced while in the simulation. The second max-

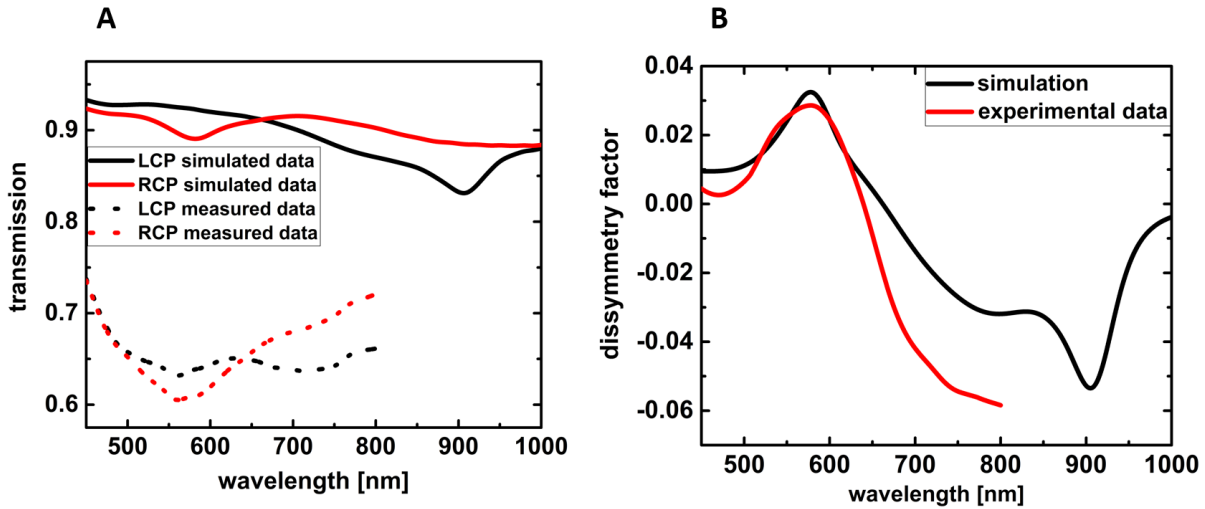


Figure 4.5: A) Simulated transmission of right- and left-circularly polarized light of a single gold helix. The measured data are added as dashed lines. B) Simulated and measured dissymmetry factor of the helix.

imum appears in the simulation at approximately the same wavelength as the second resonance in the darkfield scattering measurement. Hence, the number of resonances and their position can be identified by unpolarized darkfield scattering spectroscopy.

4.2 Atomic layer deposition (ALD) of platinum on EBID nanostructures

EBID enables the fabrication of complex 3D structures. The high carbon content on the other hand makes a uniform coating of pure metal desirable. With e-beam evaporation smooth coverage can be achieved in the case of simple single structures. To be able to cover arrays with small distance and more complex shapes, a more advanced technique is favorable.

Atomic Layer Deposition (ALD) is a chemical vapor deposition technique, capable of uniformly coating three-dimensional objects. A sequence of self-limiting processes allows for nanometer precise coverage of even structures with high aspect ratios [139]. The basic ALD process is divided into two parts, figure 4.6. First, the precursor (reactant) binds to functional groups on the surface. Consequently, a functionalized substrate is needed to start the ALD process. After purging the excess precursor with by-products out of the reaction chamber, the second half reaction starts with the introduction of the co-reactant. It binds to the adsorbed precursor until all free bonding sites are occupied and removes the ligands of the precursor. After the second purge step, where all reaction products are pumped out of the chamber, one ALD cycle is completed

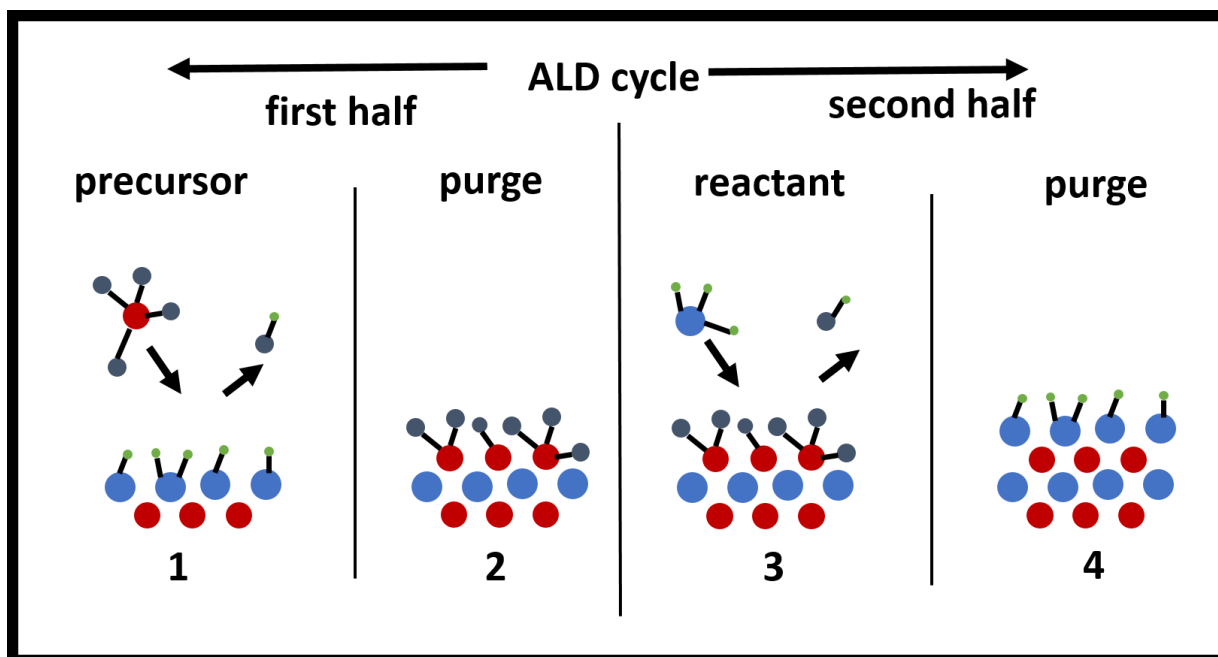


Figure 4.6: 4 steps of ALD deposition. 1) Adsorption of precursor molecules on the surface. 2) Purge of by-products as well as excess precursor. 3) Reaction of reactant with ligands from the precursor. 4) Purge reaction products plus excess reactant. Figure adapted from [138].

[138]. The four steps are repeated until the desired thickness of the ALD film is reached. In this work a FlexAL ALD machine from Oxford Instruments is used for the deposition of platinum layers.

There has been a variety of different materials explored for atomic layer deposition where oxides are most prominent [140]. Beyond oxides it has been shown that noble metals can be deposited by ALD e.g. Cu, Pt and Ag [141] which makes it a promising coating technique for plasmonics. Among these metals platinum is one of the most investigated. One possible precursor is MeCpPtMe₃, commonly used for EBID as well. Herewith, films with high uniformity as well as low resistivity could be fabricated at a temperature of 300 °C with oxygen as co-reactant [142]. The suggested thermal reaction mechanism is that atomic oxygen adsorbs on platinum surfaces during the oxygen pulse. It reacts with the ligands of the precursor, during the dose step and is released through CO₂ and H₂O among other by-products in the purge step [142]. The deposition rate shows a strong decrease in growth rate when the temperature is lowered [143]. While high temperatures are no general problem for EBID, three dimensional EBID structures tend to deform when exposed to high temperatures (see also figure 5.8). To avoid any structural changes the temperature of the ALD process has to be substantially lowered. At low temperature platinum oxide as well as pure platinum can be grown, depending on exposure time of the oxygen plasma,

substrate temperature and vapor pressure. However, there is a lower limit of 150 °C below no pure platinum films can be deposited without an additional oxidizing agent [144]. By an additional hydrogen plasma step it is possible to grow pure platinum films at room temperature [145]. The PtO_x which forms during the oxygen plasma step is reduced to pure Pt during a hydrogen plasma cycle.

Mackus et al. [146] were the first who combined the lateral resolution of EBID with the high purity of ALD by using an EBID seed layer. This method takes advantage of the substrate selective growth from ALD by pre-depositing an Al₂O₃ layer onto a silicon substrate. On top of this layer EBID-platinum squares with heights as low as two nanometer were deposited. The ALD-platinum is selectively grown onto the seed squares leaving the unpatterned part of the substrate unchanged [146]. This result nicely shows the possibility to combine EBID with ALD but does not explore the full flexibility of the 3D EBID capabilities.

4.2.1 Properties of ALD platinum

Permittivity To ensure the formation of pure platinum, ALD layers are characterized by optical and electrical measurements. The layers are fabricated with the following process: Substrate temperature 120 °C, supply line temperature 115 °C, 1 s precursor dose, 5 s purge, 2 s oxygen plasma, 5 s purge, 2 s hydrogen plasma, 10 s purge. Argon is used as carrier gas. 650 cycles result in a layer thickness of 20 nm, thus a deposition rate of 0.031 nm/cycle is achieved. Figure 4.7 B shows a SEM image of a planar deposited ALD layer with a thickness of 20 nm. Clearly visible is the formation of a closed layer. The image shows the ALD-platinum layer be composed of connected grains with sizes around 50 nm.

The optical properties of platinum show significant differences depending on the method of deposition and layer thickness [148, 149]. A discrepancy between sputtered and evaporated platinum was observed by Tompkins et. al [148]. It was found that the real part of the evaporated films had larger negative values. A possible reason is the different mass density of the films. Their evaporated films had a density of 18.8 g/cm³, compared to 14.6 g/cm³ for sputtered. The density for bulk platinum is 21.45 g/cm³. Both measurements were performed on thin films below 100 nm. [19, 147, 148]

The permittivity of the ALD-platinum is determined by ellipsometry on a 20 nm thick layer grown onto a silicon substrate. These layers are fabricated with the same process conditions used for nanostructures. The energy range in the measurement is between 1 - 5 eV (figure 4.7 A). The real part of the permittivity shows the typical metallic behavior with a large negative

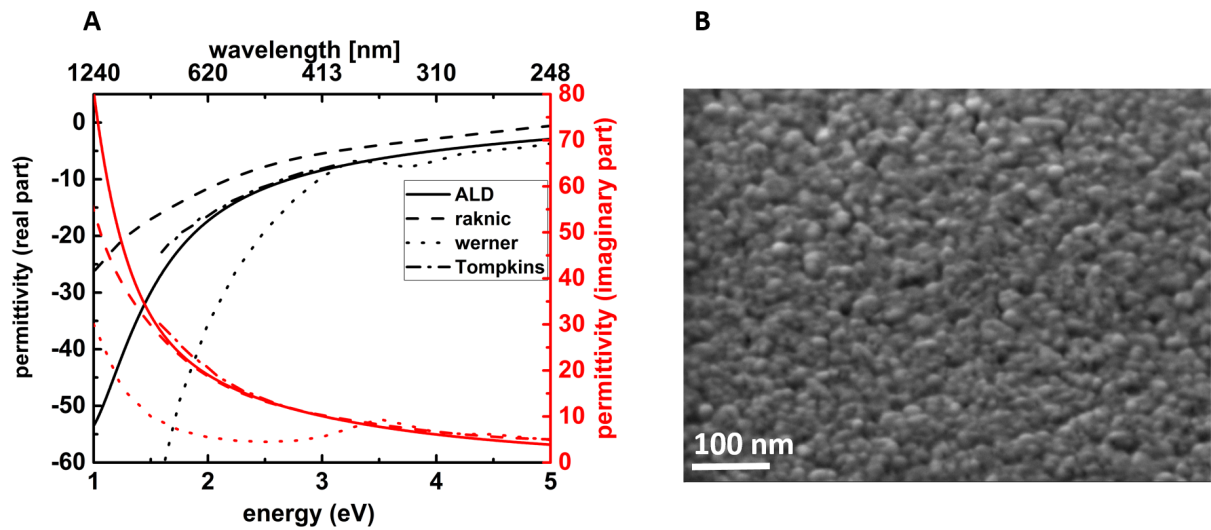


Figure 4.7: A) Comparison of the measured permittivity of ALD-platinum (20 nm ALD) with values from Raknic et al. [19], Werner et al. [147] and Tompkins et al. [148]. B) SEM image of the same platinum layer as used for the ellipsometry measurement.

value for low frequencies and an increase towards higher energies. In figure 4.7 A three literature values of platinum are added. Evaporated platinum films [148] (Tompkins et. al), modeled data on the basis of measurement on bulk platinum [19] (Rakic et. al) and results from reflection electron energy loss spectroscopy [147] (Werner et. al) are shown. The measured value is in good agreement with the measurements of Tompkins et al. [148], while these just provide data for the visible spectral range (400 nm - 800 nm) While all methods seem to result in similar values for the real part of the dielectric function in the ultra violet regime, they vary a lot in the low energy range.

Resistivity In addition to the optical properties does also the electrical resistivity of platinum depend on the chosen fabrication parameters. Bulk platinum has a resistivity of $10.6 \mu\Omega\text{cm}$ [151]. However, evaporated platinum films show higher values, which decrease by annealing at high temperatures [152]. The higher resistivity compared to bulk value is attributed to two effects. Evaporated films show smaller grains thus additional scattering at grain boundaries leads to an increased resistivity. The other effect is for thin films, where scattering on rough surfaces further increase the resistivity [153]. Physically deposited films often show a correlation of the grain size on the layer thickness and consequently a dependency of the layer thickness to the resistivity [154]. The same dependency was observed for ALD-platinum films [142]. The reason of the resistivity decrease can be attributed to larger grains that form during longer growth rates

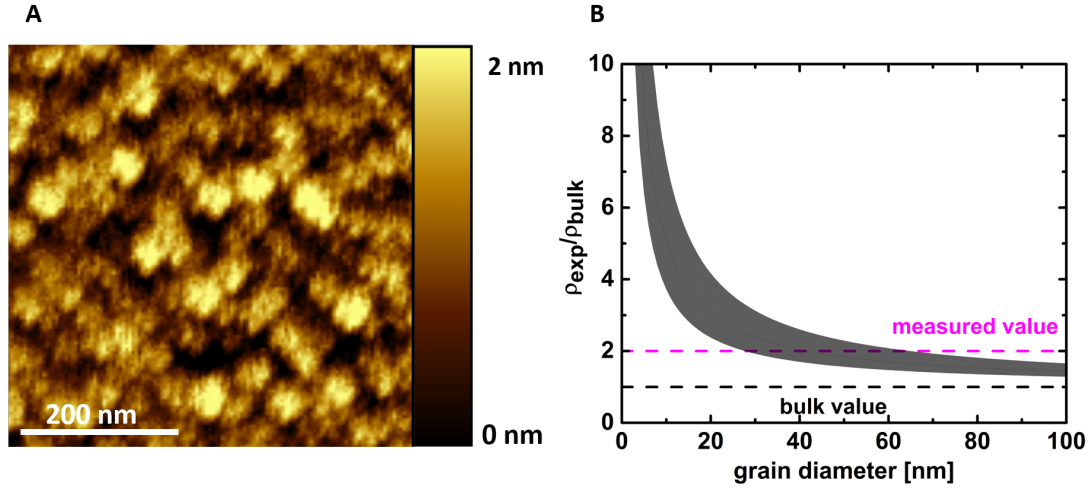


Figure 4.8: A) AFM image of a platinum film deposited with ALD. B) Dependence of the electrical resistivity on the grain size diameter calculated with the formula 4.3 from [150].

and thus thicker films. A value close to the bulk material was achieved for a layer thickness of 110 nm.[142]

A formula for the resistivity depending on the grain size is given by [150]:

$$\frac{\rho_{\text{exp}}}{\rho_{\text{bulk}}} = \frac{1}{1 - \frac{3}{2}\zeta + 3\zeta^2 - 3\zeta^3 \ln(1 + \zeta^{-1})}, \quad (4.3)$$

and

$$\zeta = \frac{\varpi G}{D(1 - G)}. \quad (4.4)$$

This equation gives the ratio of resistivity of platinum films with grain boundaries to the bulk value, where ϖ is the temperature dependent mean free path of the electrons in the platinum film without grain boundaries, about 20 nm for platinum. G is the reflection coefficient which is in the range of 0.5 - 0.7 [155] for platinum and D is the diameter of the grains.

In figure 4.8 B equation 4.3 is plotted for grain sizes from 1 - 100 nm. The shadowed area shows the values for G between 0.5 (lowest curve) and 0.7 (highest curve). The line in the middle is the solution for $G = 0.6$. The dashed lines denote the bulk resistivity of platinum and the value measured of the ALD film. With a resistivity of $21 \mu\Omega\text{cm}$ the ALD layer shows about twice the bulk value of platinum. According to figure 4.8 B this value suggest a grain size between 20 - 70 nm.

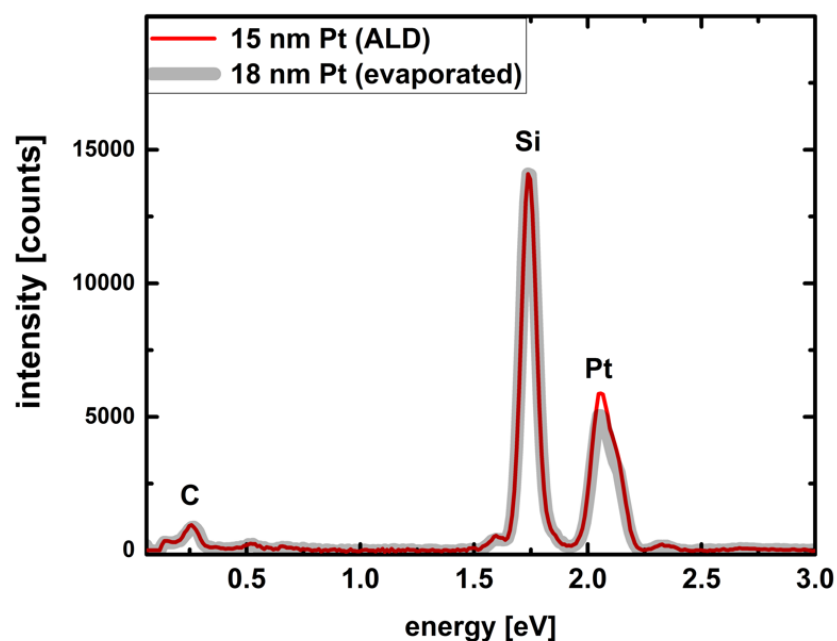


Figure 4.9: A) EDX spectra of a thin platinum layer deposited by ALD (red line) and with electron beam evaporation (grey line). Silicon peaks have been normalized to each other.

Estimation from AFM 4.8 and SEM 4.7 B images confirms a grain size in this range. The low roughness of the ALD layer with root mean square (RMS) values below one nanometer suggests that the main contribution to the electrical resistivity is due to electron scattering at the boundaries inside the film. The resistivity value of the measured ALD layer is in the range of literature values from platinum films deposited by CVD [142] and ALD [156].

Chemical composition Figure 4.9 shows the EDX spectra of platinum films deposited by ALD (red) and electron beam evaporation (grey). The spectra are taken at 5 kV in spot mode for both samples. The silicon peaks from the substrate are normalized to each other. The height of the platinum peak is slightly higher for the layer deposited by ALD. Possibly due to a higher density in the ALD film. The carbon peak can be attributed to the residual gases in the vacuum chamber. In both samples no oxygen peak is observed which supports the conclusions from the ellipsometry and electrical measurements that pure platinum is grown and no platinum oxide is present.

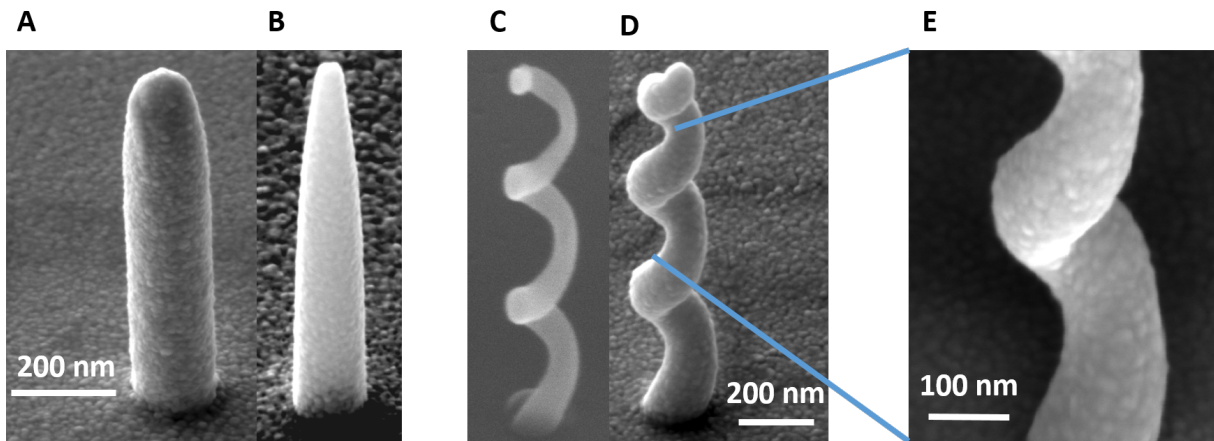


Figure 4.10: A), B) Nanopillars grown by platinum and carbon precursor respectively. Both covered with a 20 nm layer of ALD. C), D) EBID-helix before and after coverage with a 20 nm thick layer of ALD-platinum. E) Magnification of the middle part of the helix from D.

4.2.2 ALD coated EBID nanostructures: Scattering and dissymmetry

Figure 4.10 shows the capability of covering EBID nanostructures by ALD with a smooth layer of platinum and minimal shape distortion. Figure 4.10 A and B show two nanopillars grown with platinum (MeCpPtMe_3) and carbon ($\text{C}_{14}\text{H}_{10}$) containing precursors respectively. The different tip shape originates from the different precursor, not the ALD process. Both materials are covered with the same ALD process. At the bottom a smooth transition from the platinum on the substrate to the nanostructure is visible. Figure 4.10 C and D shows a helix before and after coverage with 20 nm of platinum by ALD. The helix dimensions are a pitch height of 220 nm, an wire thickness of 70 nm and an external diameter of 170 nm. The helix shows minimal shape distortion on the top, most probably induced by temperature during the ALD process. This might be improved by further lowering the temperature process. It has been shown that platinum can be deposited by ALD at room temperature [145]. However, in this work the ALD process at room temperature does not result in any deposition. The process in this work is performed at the lowest temperature (120 °C), where a deposition is observed.

Darkfield scattering As shown in chapter 3.2.2, the as-deposited EBID material has a dielectric rather than a metallic behavior. In the case of gold the optical response, with respect to the darkfield scattering intensity could be largely improved by an additional pure metal layer. In figure 4.11 A the darkfield scattering spectrum of an as-deposited EBID-platinum helix together with a helix which an additionally 20 nm thick ALD platinum layer is shown. The inset shows an optical picture of the microscope image in darkfield configuration of a single helix. The bright

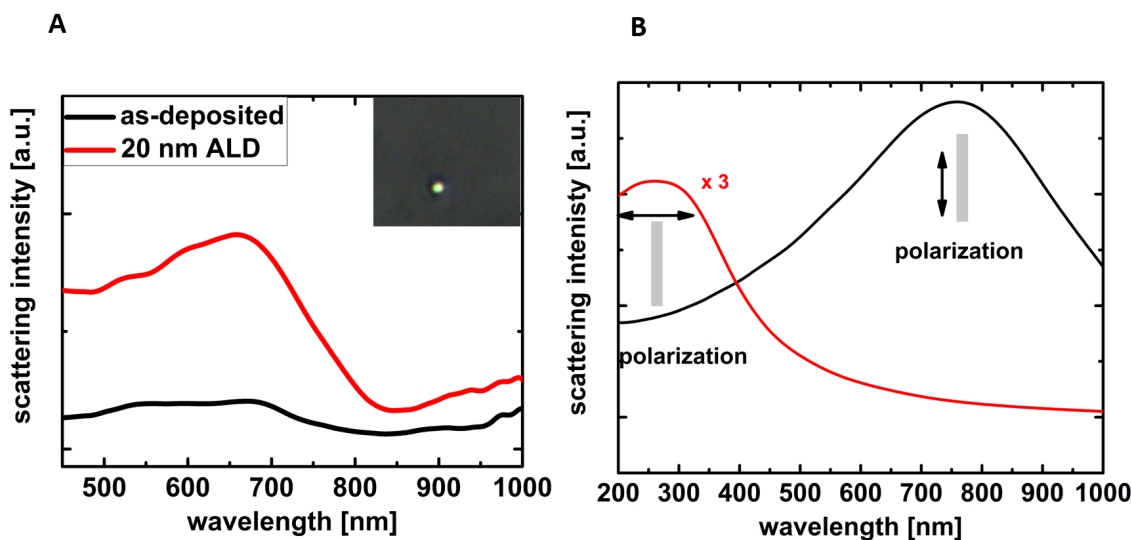


Figure 4.11: A) Measured darkfield scattering spectra of the EBID helix as-deposited (black) and covered with a 20 nm thick layer of platinum by ALD (red). B) Simulated scattering spectrum of platinum nanorod for both polarizations. The nanorod has a radius of 35 nm and a height of 230 nm.

spot depicts the position of the helix, clearly visible in contrast to the dark background of the substrate. The scattering spectrum shows a very broad resonance with its maximum around 680 nm. The second peak, which is observed in the case of an EBID-gold helix with a pure gold layer does not appear in the investigated spectral range. The low intensity from the substrate is another conformation of the closed smooth layer of the ALD-platinum. In the case of single platinum particles or a very rough surface, a stronger scattering signal from the substrate would be expected. In figure 4.11 B the simulated scattering intensities of a platinum nanorod with a height of 230 nm and a diameter of 70 nm for both polarization is plotted. As for the case of the gold helix, is the long wave resonance resembled by the scattering of the long axis of the nanorod. The short wavelength resonance in the simulation lies in the UV region cannot be verified with the light source used in this work.

Dissymmetry measurements and simulation Arrays of as-deposited EBID-carbon helices [129] and EBID-platinum helices [13] have shown a dissymmetry in transmission of left- and right circular polarized light. Though metallic material is not essential for circular polarization dependent transmission. In the infrared region, dielectric helices have been suggested to have higher suppression ratio, compared to their metal counterpart [157]. For helices in the size range of hundreds of nanometer, the CD signal could be improved by using a focused ion beam,

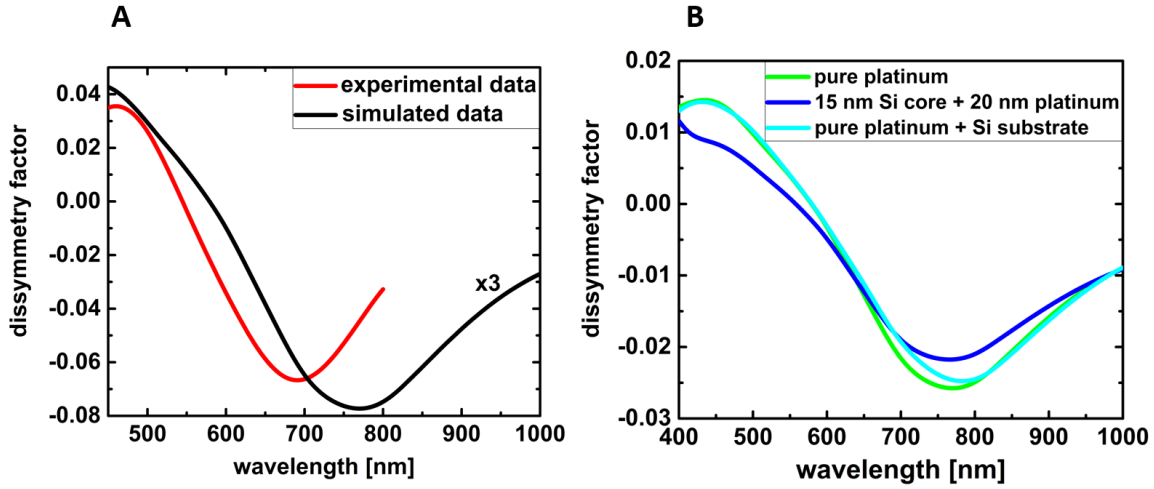


Figure 4.12: A) Measured dissymmetry factor of an EBID-platinum helix covered with 20 nm ALD-platinum compared with the simulation of a pure platinum helix. B) Simulated influence of substrate and a dielectric core on the dissymmetry factor of a platinum helix.

instead of an electron beam [13]. The reason is the higher platinum content for ion beam induced deposition. On the other hand the use of a focused Gallium ion beam limits the fabrication to larger structure sizes. Also the implementation of gallium ions into the structures cannot be hindered. Simulations on EBID-platinum helices with different volume fractions showed an improved CD signal for higher platinum content. The combination of EBID with ALD enables the fabrication of small structural sizes with a pure platinum shell.

For single as-deposited EBID-platinum helices no dissymmetry between the transmission of right- and left-circular polarized light could be detected. Due to the low signal from a single helix, the effect is not observable with the setup of this work. However, an additional layer of pure platinum enables the investigations of single helices, also for platinum. The dissymmetry factor as a measure of the different transmission of left- and right circular polarized light is plotted in figure 4.12 A. It shows a maximum value of 0.06 around 700 nm. At 550 nm the dissymmetry factor changes its sign, thus the other polarization state is preferably transmitted. Platinum and gold helices exhibit the same shape of the dissymmetry curve. Compared to gold the spectrum for platinum is shifted towards lower wavelength. This is due to the different dielectric function also visible in the Mie scattering spectra for platinum and gold spheres. In contrast to Mie scattering, the measured maximum dissymmetry value for platinum is higher than for gold. While in the work the negative dissymmetry peak in the case of platinum and positive in the case of gold could be measured the values are not directly comparable.

For FIBID-platinum helices a zero crossing was observed for helices with a diameter of 400 nm

while for the case of electron beam induced fabrication which result in a diameter of 230 nm no crossing was visible in the measured spectral range [13]. The reason is possibly that the positive CD signal lies in the UV region of the spectrum.

The dissymmetry factor in this thesis is simulated by a finite difference time domain technique and compared to the measured data. The results are depicted in figure 4.12 A and B. The simulated structures resemble well the measured behavior, with a small shift to higher wavelength. To investigate a possible influence of the remaining EBID core to the CD signal, a dielectric core is added to the simulated structure. The new configuration is a dielectric silicon core of 15 nm radius with a 20 nm pure platinum shell. In another model a silicon substrate is added to a pure platinum helix. The core and substrate not show a major influence on the position or the intensity of the dissymmetry signal, see figure 4.12 B. In both cases the difference from the simulated pure platinum helix is minor. The peak values is highest for the case of pure platinum while the spectral position of the peak does not shift largely.

As mentioned before does as-deposited EBID helices exhibit beside their circular dichroism also a linear dichroism. This can be explained if a single pitch of a helix thought of as a split ring where one end has been pulled up in the third dimension, as described in [135]. A split ring shows different behavior if the impinging light is polarized parallel or perpendicular to the slit [158]. Thus split rings show as well a circular dichroism when illuminated under non-normal incidence [159]. To control if the measured circular dichroism is not an artifact from the linear dichroism of the structure and a not perfectly polarized light source, the structure is rotated 90 degrees and the spectrum measured again. In the case of a linear dichroism the sign would change however the same spectrum is recorded for the sample rotated 90 degrees.

5 Purification of EBID nanostructures

The carbon contamination in EBID structures from metal-organic precursor compounds is the main drawback for applications in plasmonics. In the previous section, two coating methods were presented for the case of gold and platinum. Both improved the optical response of chiral EBID nanostructures. The simple electron beam evaporation process is successful for single nanostructures while shadowing effects are expected to arise for small distances as in arrays. Especially ALD is a very promising coating technique for nanostructures because shadowing is not an issue. Additionally ALD features uniformity and high thickness precision. However, only few metallic precursors are available for ALD. Furthermore, the process is complex, time consuming and requires expensive equipment. For this reason additional purification techniques of EBID materials are investigated concerning shape preservation of nanostructures and plasmonic response.

Most purification methods employ in-situ substrate heating during the deposition process [160], post-treatments of the structures by annealing in different oxidizing atmospheres [80, 161] electron irradiation or laser treatment of the structures [70]. A flow of oxygen during the deposition process leads to highly pure gold deposits, as recently shown [162]. These examinations resulted in high purification of mainly planar deposits. To purify complex three-dimensional EBID nanostructures is still a challenge. Ozone oxidation in moderate temperatures around 175 °C was a first attempt to purify 3D structures [58]. In-situ electron beam irradiation on vertical standing nanopillars from the precursor $\text{Me}_2\text{Au}(\text{tfa})$ was another approach. With an additional oxygen plasma step gold crystals were found inside the structures [68]. For plasmonic applications a pure gold layer on the outside is needed. The deposition of gold containing precursor $\text{Me}_2\text{Au}(\text{acac})$ inside an environmental scanning electron microscope (ESEM) with water as background gas leads to the formation of structures consisting of a dense core surrounded by a carbonaceous shell [163]. The ESEM broadens the focus of the electron beam leading to feature sizes in the micrometer range. Another gold precursor $\text{Me}_2\text{Au}(\text{tfa})$ was used in a dual GIS system together with water vapor and achieved highly conductive and pure gold structures [164].

In this work deposits from the precursor $\text{Me}_2\text{Au}(\text{acac})$ are attempted to be purified after deposition in a similar way.

5.1 Purification of an EBID-gold pillar with water vapor

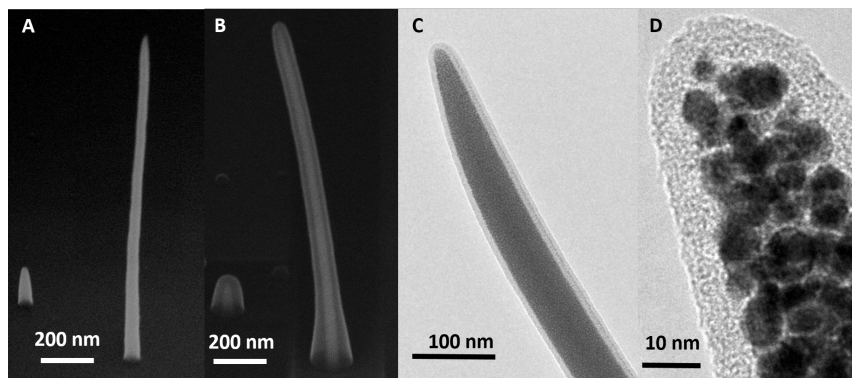


Figure 5.1: Scanning electron micrographs in tilted view (38 degree) of single EBID pillar deposited using the precursor $\text{Me}_2\text{Au}(\text{acac})$ on silicon substrate A) before and B) after 2 min electron irradiation in the presence of water vapor. C) Transmission electron micrograph of a pillar treated with the same recipe as the one in B. D) Magnification of the tip of the nanopillar from B.

EBID nanopillars of 50 nm in diameter and 1.5 μm in height are irradiated in a water vapor background (10^{-4} mbar) for two minutes. As shown in 5.1 A and B a core shell structure has formed. TEM investigations 5.1 C and D confirms the formation of a dense core surrounded by a carbonaceous shell. This is similar to the deposition in an ESEM, where water vapor was present during the deposition [163]. In plasmonic applications the interaction between light and the structure is localized to the surface. Thus a pure metal surface is needed.

5.2 Plasma purification of EBID-gold nanostructures

To directly achieve plasmonically active metal surfaces in combination with shape preservation, a simple and fast oxygen plasma cleaning step at room temperature is investigated. The geometrical modification of the structure under purification is examined by REM and TEM measurements on single pillars. The quality of purification is measured by the change in resistivity of planar structures as-deposited and after purification and by EDX analysis. The results presented in this chapter are published in reference [165]. The TEM measurements were done by A. Manzoni in cooperation with the author of this thesis. The electrical measurements were done with S. Jäckle in cooperation with the author of this thesis. The simulation were done by K. Höflich in cooperation with the author of this thesis.

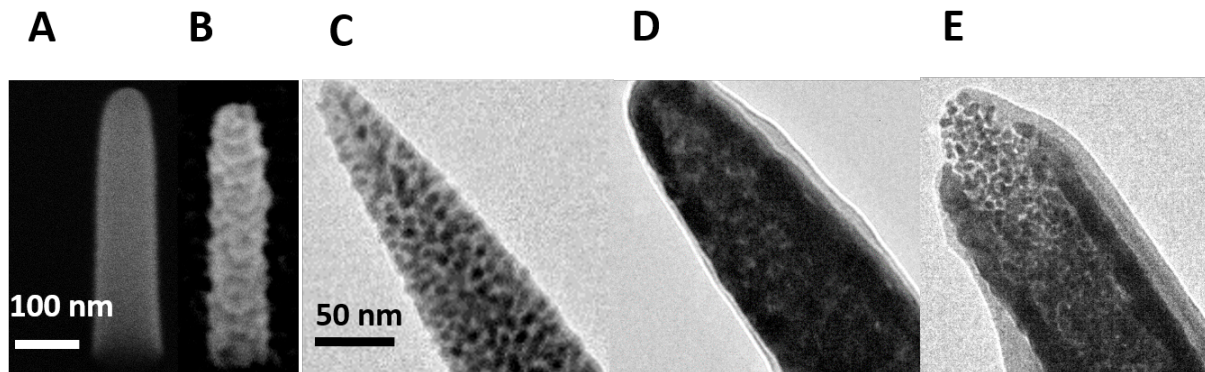


Figure 5.2: Scanning electron micrographs in tilted view (38 degree) of single EBID pillar deposited using the precursor $\text{Me}_2\text{Au}(\text{acac})$ on silicon substrate A) before and B) after a plasma treatment of 2 min which results in a reduction in diameter and height of 18 nm. Transmission electron micrographs of a pillar C) as-deposited, D) purified and, E) after an additional cross-section cut to increase the visibility of the core-shell structure. The bright layers onto the visible pure gold layer are caused by carbon deposition from residual gases present in the vacuum chamber of the TEM. Figure as published in [165].

5.2.1 Geometrical modification by plasma purification: Core-shell structure

The influence of the plasma treatment on the geometry of single pillars is investigated. After deposition the sample is removed from the SEM chamber and placed in a table top plasma cleaner cleaning system (zepto-diener electronic) operating at 40 kHz in oxygen atmosphere at 0.3 bar with at an input power of 70 W.

Figure 5.2 A and B show the EBID-pillar before and after oxygen plasma treatment for two minutes. A significant increase of surface roughness is observed besides a reduction in volume during the plasma process. The formation of a core-shell structure is shown in 5.2 C, D and E. The as-deposited pillar in figure 5.2 C shows the typical composite structure of EBID materials. Gold crystals (dark spots) which are evenly distributed within a carbonaceous matrix (bright areas). Figure 5.2 D shows the purified pillar. The core-shell structure is already visible. However, hard to distinguish from the core due to the low transparency. Therefore, the pillar is thinned by a focused ion beam, which unveils the core-shell structure more clearly, figure 5.2 E. The outer shell of high gold content has a thickness of about 20 nm, and the inner core consist of as-deposited EBID material. The deposition of residual gases during the TEM measurement leads to an additional bright shell on the outside of the structure.

The diameter reduction during the plasma treatment is independent from the initial diameter depicted in figure 5.3 B. Instead, the same reduction of 18 nm is observed for all initial diameters. This suggests that the purification process has a certain limited penetration depth, already ob-

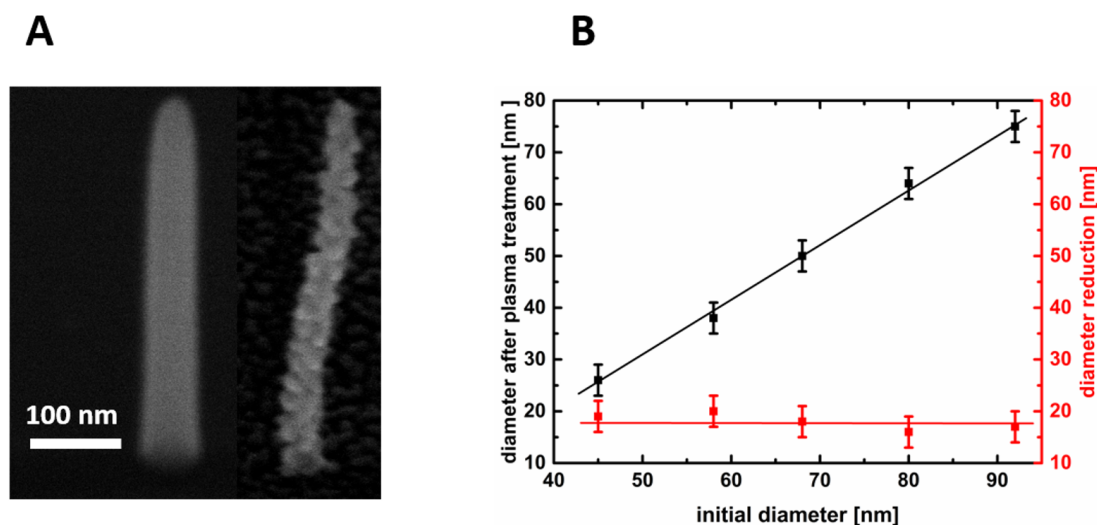


Figure 5.3: A) Deformation of a thin pillar during plasma treatment. B) Diameter reduction of EBID pillars for different starting thicknesses after purification of 2 min in oxygen plasma. Lines are only for guidance. Figure as published in [165].

served for hydrogen radicals [80]. In the investigated case of oxygen plasma, the process stops after a closed gold layer is formed. The volume reduction is due to the oxidation of carbon atoms. Most likely released through CO or CO₂ [107]. The stability of the shape shows a significant dependence on the diameter. Only pillars with diameters larger than 60 nm reliably preserve their shapes. Deformation of the the structure starts for smaller diameters, seen in figure 5.3. The as-deposited pillar is shown on the left side and the pillar after plasma purification on the right. As for larger diameters is a reduction of around 18 nm observed. Additionally, the pillar bends towards the side which results in a small s-like shape. Figure 5.4 shows the purification of nanopillars at different time steps. The time evolution suggests a top-down or in the case of 3D structures and out-to-in purification. This top-down evolution is in agreement with earlier purification studies by electron irradiation in oxygen atmosphere on EBID-platinum [107]. In this study the top-down purification is due to a low permeability coefficient and a high chemisorption of oxygen. This leads to purification limited close to the surface. The opposite purification way (bottom-up) was observed by the purification with water vapor. This is attributed to a higher permeability coefficient and a lower chemisorption of water compared to oxygen[166]. The out-to-inside purification observed in this thesis is a hint that the permeability coefficient of the oxygen radicals are comparably small to the case of molecular oxygen.

Gold layer growth is usually accompanied by Ostwald ripening, which results in the formation of small islands before a close gold layer is formed [167]. A closed layer forms, depending on

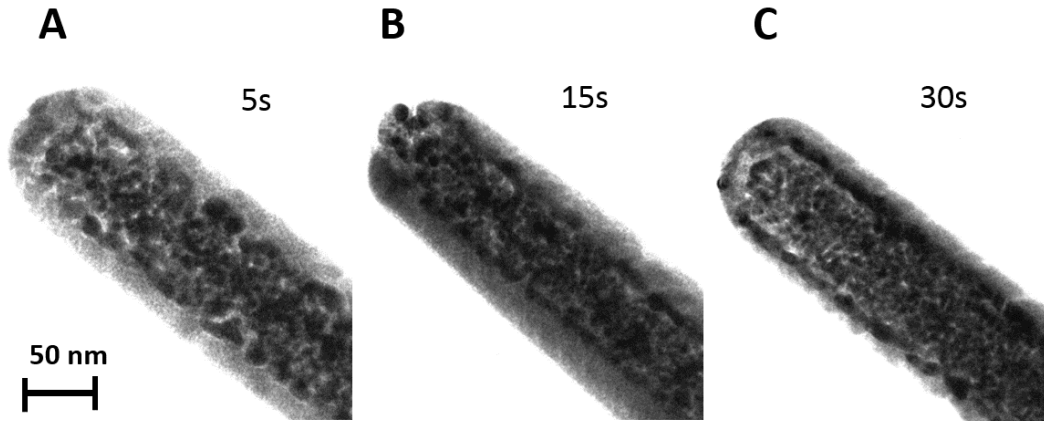


Figure 5.4: Early steps of the plasma purification process shows TEM cross-sections for pillars purified 5s (A), 15s (B) and 30s (C) respectively. Figure as published in [165].

the temperature, between 10 - 20 nm,[168]. This supports the suggestion that the purification with oxygen plasma is possible to the point where a closed gold layers has formed. The closed gold shell hinders the penetration of oxygen to the EBID core and thus further purification.

5.2.2 Quality of gold shell after purification

In EBID material the resistivity and metal content are correlated [12]. To quantify the purification effect of the oxygen plasma treatment on EBID structures electrical resistivity measurements of the as-deposited-EBID material and after purification are compared. Resistance measurement on four EBID bridges between differently spaced gold pads is carried out. The different distances allow to eliminated the contact resistance between the EBID material and the gold pads. The distances of the gold pads is 0.7 μm , 1.7 μm , 2.7 μm and 3.7 μm . The gold pads are deposited by electron beam evaporation by a Balzer PLS 570 evaporator with a base pressure around 10^{-6} mbar. The height is 100 nm onto 10 nm adhesion layer titanium. The measurements are performed using a Keithley SCS 4200 semiconductor characterization system. To prevent Joule heating only currents $< 1\text{mA}$ are used.

Figure 5.5 A shows an atomic force micrograph of an EBID bridge together with the extracted height profile. The height profile is used to determine the cross-section of the bridge. Figure 5.5 B display the resistance before and after the plasma purification. A specific resistivity of

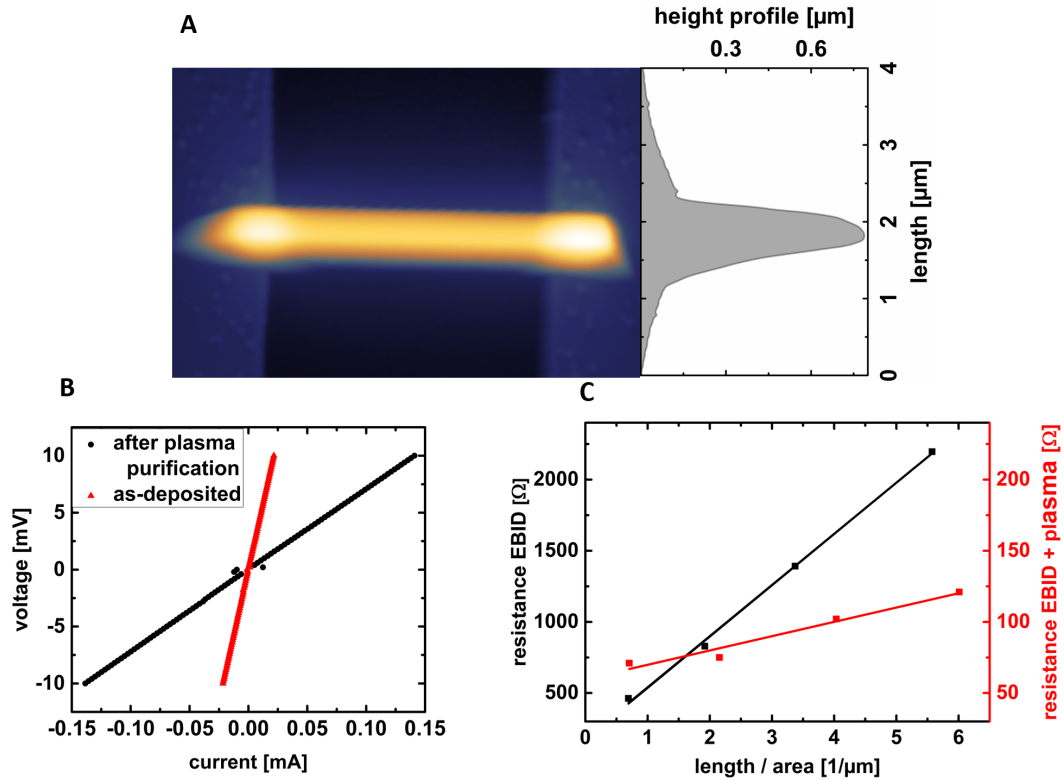


Figure 5.5: A) Atomic force micrograph and extracted height profile of EBID bridge between two gold pads. B) Current-voltage curve for the as-deposited and purified structure. Visible is the large decrease in resistance due to the removal of isolating material C) Resistance over length/area of EBID bridges measured between four different distances before (black) and after (red) plasma purification. Figure adapted from [165].

$360 (\pm 14) \mu\Omega \text{ cm}$ for the pure EBID material is determined from the slope. For the purified material this decreases to $10 (\pm 2) \mu\Omega \text{ cm}$. In both cases the curves show an ohmic behavior by the linear dependence between current and voltage. For pure EBID structures often a non-ohmic behavior is observed [68, 164]. Since currents in this thesis are below 0.15 mA, significantly lower than in the literature [164] and [68] a direct comparison is not possible. However, it is worth mention that for the EBID structures a current could only be measured if the substrate is before the deposition cleaned in oxygen plasma. Suggesting that the surface contamination occurring during the storage of the substrate leads to a barrier between the gold pads and the EBID material.

Also the contact resistance, extracted from the y-axis intercept, decreases from $173 (\Omega) \text{ pm } 45$ to $60 (\pm 6) \Omega$. The large improvement in resistivity is solely to the purified gold shell, since the core consist of as-deposited material. Consequently the measured value gives an upper limit for the resistivity of the shell. With a constant 20 nm thick shell throughout the whole bridge, based

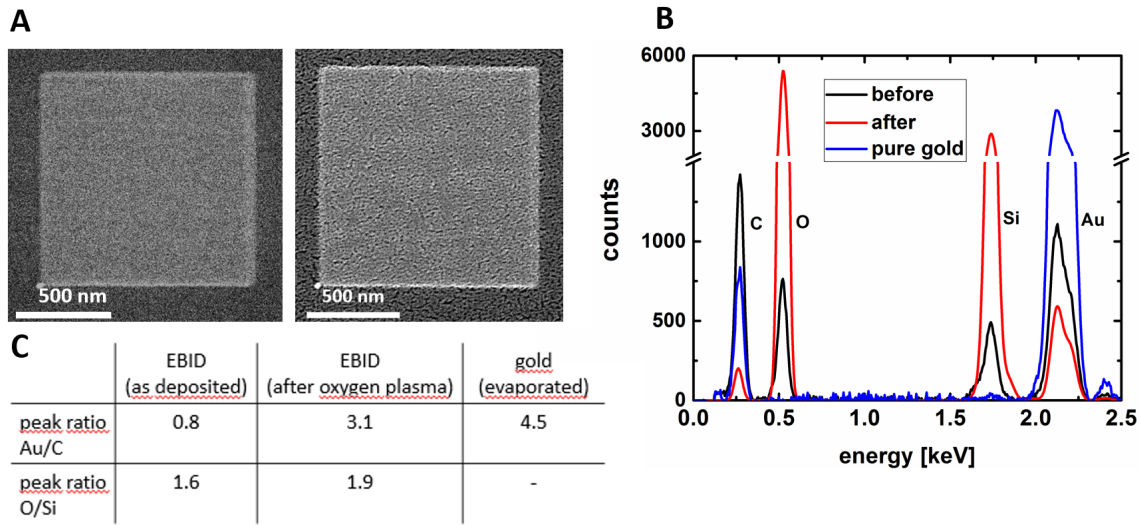


Figure 5.6: A) Scanning electron micrographs of the EBID pads as-deposited (left) and after plasma purification (right). B) EDX spectra of EBID pad as-deposited (black curve), purified (red curve) and pure gold (blue curve) for comparison. C) Peak ratios of gold to carbon for all three cases and oxygen to silicon for the EBID material before and after purification. Figure as published in [165].

on the TEM results, the specific resistivity of the shell material is $110 (\pm 50) \mu\Omega\text{cm}$. The core material resistivity is identified with the measured value for the as-deposited material. Bulk gold has a resistivity of $(2 \mu\Omega\text{cm})$, which is almost two orders of magnitude smaller compared to the purified shell. As explained in chapter 3.1.1, this behavior can be explained by additional scattering at grain boundaries inside the material [169]. The grain boundaries in the purified material originated from the individual gold clusters in the as-deposited EBID material. Additional increase in resistivity is due to the high surface roughness. Also an imperfect purification of the shell material cannot be ruled out. The volume reduction and improved conductivity suggest a carbon removal during the oxygen plasma step. To validate this assumption EDX measurements are performed on as-deposited and purified structures. Since the exact measurement, especially for thin pads where the influence of the substrate is still present is rather difficult by EDX, the relative peak ratios are compared. Figure 5.6 A and B show scanning electron micrographs of planar EBID pads before (left) and after (right) plasma purification, used for EDX analysis. The height of the pad after plasma purification is 12 nm. With a penetration depth of around 20 nm for the oxygen plasma the layer is assumed to consist only of purified material. An evaporated gold layer of 250 nm is used as a reference for pure gold. Figure 5.6 C and D show the EDX spectrum and peaks ratios of gold to carbon and oxygen to silicon for the as-deposited and purified pads.

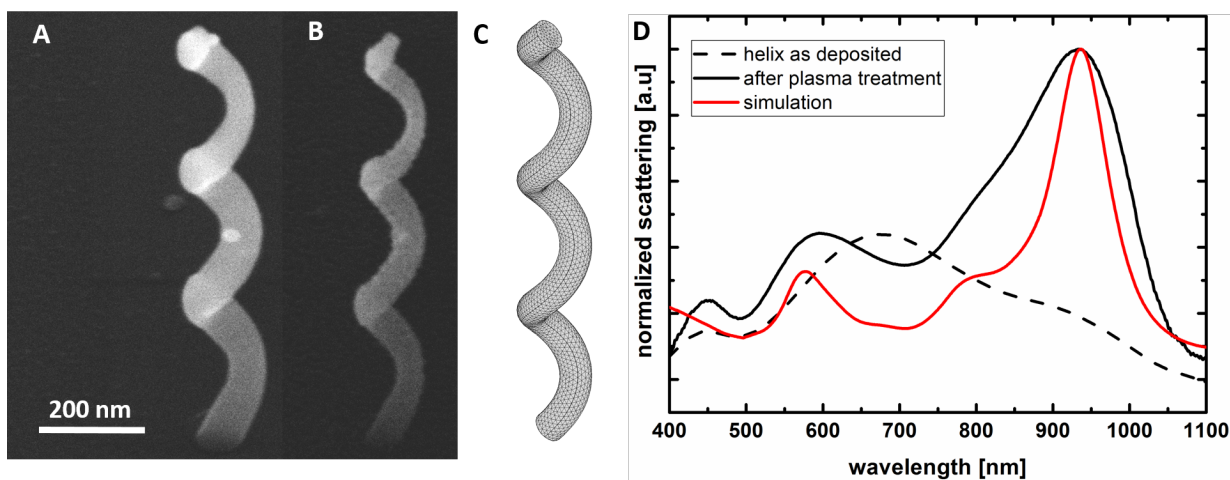


Figure 5.7: Scanning electron micrographs in tilted view of helix with three pitches as-deposited A) and B) after plasma purification. C) Mesh plot of the corresponding modelled helix, D) comparison of the as-deposited, plasma treated and simulated scattering spectra. Figure as published in [165].

The EDX spectrum of the pure gold sample (blue curve) is added to the graph. However, also the pure gold sample exhibits a carbon signal which originates from the residual gases in the vacuum chamber. The gold to carbon peak ratio increases from 0.8 to 3.1 from the as-deposited to the purified pad. The silicon peak from the substrate increases for the purified sample. The reason is a thinner pad and the formation of voids, thus a stronger signal from the substrate is detected. The same holds true for the oxygen peak, partly originates from the SiO_x of the substrate. The EDX measurements further proves the removal of carbon by the oxygen plasma step.

5.2.3 Plasmonic scattering of a single purified EBID-gold helix

Finally, the purification of complex three dimensional structures, in this study gold helices with three pitches, is investigated. The plasmonic activity of the purified helices is examined using dark field scattering spectroscopy and compared to finite element modeling of geometrically equivalent pure gold helices.

Figure 5.7 shows scanning electron micrographs of a helix with three pitches as-deposited A), after plasma purification B) and the model used for the simulation C). Comparing figure 5.7 A and B reveals the shape maintenance of the helix during the purification process. The helix dimensions are extracted from the SEM images, under consideration of the tilted view of 38 degree, to be 120 nm of external diameter, a pitch height of 320 nm and an arm thickness (after purification) of 30 nm. Figure 5.7 C shows the dark field scattering spectrum measurement,

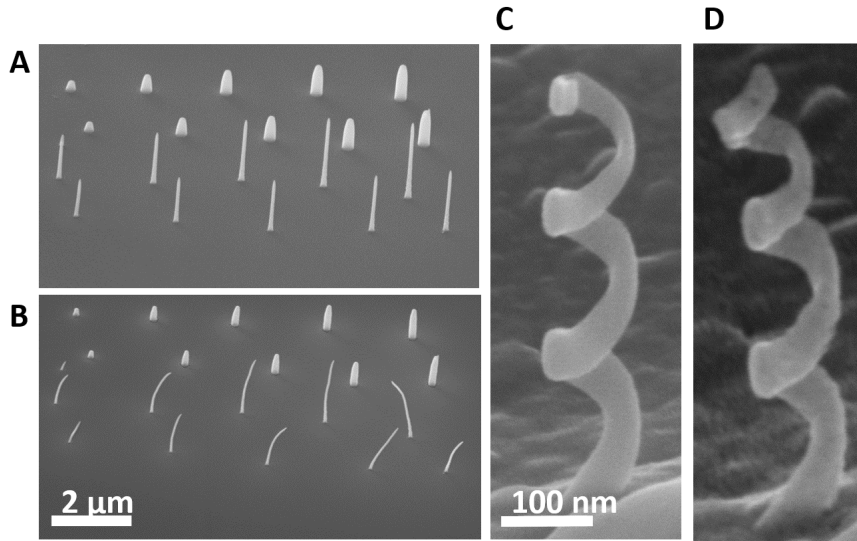


Figure 5.8: A,B) Array of EBID pillar with varying thickness annealed at 200 °C under ambient conditions for 1 hour. Thinner pillars show more deformation compared to thicker ones. C, D) EBID helix annealed with the same parameters. The thinnest third pitch shows a deformation while the rest of the shape stays unchanged.

compared to the simulated scattering efficiencies of a pure gold helix. Both spectra show two distinct strong resonances as observed for the case of EBID helices covered with a pure gold layer by electron beam evaporation. In comparison with the simulation the measured resonances show a broader linewidth. The reason are additional losses by grain boundaries and surface roughness, also responsible for the larger conductivity of the purified material compared to bulk gold. The measured short wavelength resonance around 570 nm is slightly shifted to higher wavelength compared to the simulations. The long wavelength resonance at 950 nm is almost perfectly resembled by the simulation. The peak around 450 in the measurement is not resembled by the simulation. This peak is not present in the case of a EBID helix covered with a 20 nm of pure gold layer by electron beam evaporation. Thus the origin is likely to surface roughness around the helix induced by the purification. The overall agreement between experiment and theory proves that the purified EBID-helix can be simulated by a pure gold one.

5.2.4 Limitations of plasma purification of nanostructures

Temperature influences the EBID process in two ways. At first, an increase in substrate temperature leads to a decrease in deposition rate due to the lowered residence time of the molecules on the surface [170]. Hence, EBID at very low temperatures leads to a large increase in deposition rate [171]. The deposition process changes in the sense, that the injected precursor molecules

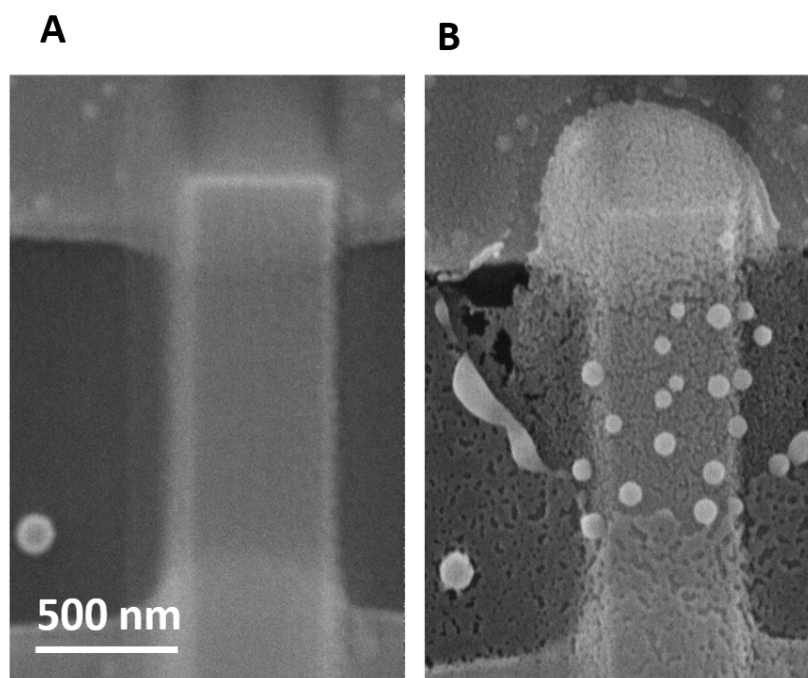


Figure 5.9: A) Thin bridge after plasma purification and B) after electrical measurement.

freeze onto the substrate. This leads to multiple layers of precursor while EBID at room temperature is normally limited to a monolayer. After that the molecules are dissociated by the electron beam and the unpatterned part is sublimated during reheating. However, the increase in deposition rate due to multiple layer hinders the formation of three dimensional structures [171]. The other impact of heat is the change in composition of the material. Deposition of EBID on a preheated stage has shown to enhance the gold content while the platinum content did not show any improvement [172]. A post annealing step in air leads to an increase in the platinum content, suggesting that oxidizing species are needed to initiate the carbon removal [173]. Besides the purity the conductivity is improved by using a post annealing step both for platinum and gold containing depositions [174]. For annealing temperatures as high as 600 °C even a gold content above 92 % has been reported. While this purification can be used for planar structures, nanostructures suffer from deformation at these temperatures [69]. Figure 5.8 shows the deformation of EBID nanostructures by annealing at 200 °C for 60 min in ambient conditions. From A,B it can be seen that thicker pillars are deforming less.

This is further supported by 5.8 C,D where a helix is heated to 200 °C and only the upper part of the helix shows deformation. Another interesting finding is that with our purification routine it is not possible to fabricate thin conductive gold layers which just consist of purified material. A shrinking of around 18 nm and a resulting shell of 20 nm purified material would suggest

that an initial thickness of 38 nm would result in a 20 nm thick layer of pure purified material. Anyhow the resulting structure shows a granular morphology with gold clusters instead of a smooth conformal layer. Electrical measurements results in the destruction of the bridge grown by EBID. In figure 5.9 a thin bridge is shown after plasma treatment A) and after the electrical measurements B). The reason, most likely, lies in the granular structure of the gold. Only a few connecting paths are formed as small conducting bridges between the two gold pads. After the purification process the whole current leads to excessive heating at these bottlenecks. As a result the gold melts down and clusters together. Thus in both cases for three dimensional nanostructures as well as for planar structures only a core shell structure and no pure functional gold structure can be achieved. For the nanostructures the core seems to act as a stabilizer for the mobile gold atoms forming on the shell while in the planar structures the additional material hinders the formation of voids while as long as EBID material is exposed to the oxygen plasma the purification continues until a closed surface has formed. However as for the application in plasmonic the response is mainly determined by the outer part the inner as-deposited EBID material should have a minor influence. For the use of electrical connections fabricated by EBID, however, a thicker pure gold film would be more favorable. Hence, the purification method applied for EBID material depends on the type of application.

6 Summary and Outlook

Within the work of this thesis the permittivities of a commonly used platinum and a novel copper containing precursor were determined by transmission/reflection measurements and additionally by imaging ellipsometry for EBID-platinum and resembled by a Maxwell-Garnett mixing Model. The materials show dielectric behavior over the whole measured spectral range. Investigations of the structure with TEM and Raman confirm that the deposits consist of metal nano particles in an amorphous carbon matrix.

For EBID-platinum Raman measurements reveal that with longer irradiation times and therefore thicker pads the amorphous carbon matrix changes its configuration towards graphite. In addition to the carbon configuration, EDX measurements show that also the material composition of planar EBID-platinum deposits changes for different deposition times too. They show a slightly higher platinum content for longer deposition times and hint to a small decrease in oxygen. However, the carbon content stays constant, different from most observed purification processes of EBID materials where the purification is explained by the release of carbon monoxide CO or dioxide CO₂ species. A possible explanation for the existence and release of volatile oxygen from deposits grown by the non-oxygen containing platinum precursor is the adsorption of water, during precursor storage or the in cooperation of residual oxygen gas during growth. Release of only oxygen was otherwise only observed in the case of post vacuum annealing oxygen-containing cobalt EBID material [88]. As anticipated, an EDX study performed in this thesis on an EBID-platinum helix shows a rather low oxygen content, as in thick planar samples, explained by the high aspect ratio and therefore long irradiation times on one spot. It is legitimate to assume, that also the carbon configuration of high aspect nanostructures is closer to that of thicker pads, exhibiting a higher graphite content.

Both effects, the change in carbon configuration and in platinum content, lead to a thickness dependent permittivity of the material. Future TEM and EDX measurements on cross-sections of EBID pads could reveal if the change in carbon configuration occurs homogeneously, or with a gradient. The presence of a gradient seems very likely as the lower part of the pad is irradiated longer than the top. Furthermore it would be interesting to directly investigate the carbon configuration on EBID nanostructures with Raman, which could be possible by measuring on a large array.

In comparison to the EBID-platinum, Raman measurements on planar pads from the novel EBID-copper reveal an even higher ratio of amorphous carbon to graphite in the matrix. The copper content in thick deposits, determined by EDX, is about 24 at.%, a rather high value for EBID material from organo-metallic precursors. Comparable EBID-platinum pads only show a metal content of about 18 at.%. This makes the copper precursor a promising candidate, espe-

cially when combined with further purification techniques.

For the common EBID-platinum as well as the novel EBID-copper the real part of the permittivity could be resembled by a Maxwell-Garnett mixing Model with carbon and the corresponding metal. According to the Raman measurements, different carbon configuration are used for EBID-platinum and EBID-copper. It has to be pointed out, that the exact permittivity of the carbon matrix can only be approximated and correlated to the measured permittivity. The measured imaginary values of the permittivities show, in both cases, higher values than the model. This may indicate an additional energy loss channel which is not considered in the permittivities of the single constituents, probably due to the approximated carbon configuration. However, in summary the model is an adequate approximation for as-deposited EBID materials. The extracted permittivity from the transmission/reflection measurements of the copper precursor could resemble darkfield scattering measurements of nanostructures fabricated by the new precursor. This indicates that the permittivity of nanostructures is likely very similar to the values for thick pads.

To improve the plasmonic performance of EBID nanostructures the effect of a metallic shell around a EBID-core is investigated. In this thesis this is achieved by either deposition of an additional pure layer or by purifying the EBID nanostructures themselves. This way the plasmonic resonances of single gold and platinum helices could be investigated.

EBID helices from a gold containing precursor are cladded with a pure 20 nm gold layer by e-beam evaporation. The core-shell structures are investigated by darkfield scattering and circular polarized dependent light transmission. In comparison to the as-deposited structures, the core-shell structure exhibits a stronger and more pronounced scattering intensity as well as an improved dissymmetry factor. The helix exhibits two resonances around 600 nm and 950 nm. Both are visible in the darkfield scattering measurement whereas, due to the limited spectral range in the transmission measurement just the dissymmetry of the lower one is visible. However, simulation in this thesis predicts that the high wavelength resonance should also exhibits a dissymmetry with opposite sign. This should be confirmed by measurements with a larger spectral range in the future. The wavelength position of maximum dissymmetry for the low wavelength resonance has been shown to depend only little on the height of core-shell helices [137]. Simulation in this work shows that the pure gold shell of 20 nm is sufficient to describe the optical behavior as if it was a pure gold structure. The reason for that is the limited penetration depth of visible light into gold. As a consequence, the light only interacts with the surface of the structure, not its core. Simulations of pure gold helices predict a strong dependence of wavelength position of maximum dissymmetry on the diameter of helix [130]. This dependence may allow to tune the point of maximum dissymmetry, if confirmed by future measurements.

A novel approach for the coating of EBID nanostructures is explored in this thesis. An ALD

process is developed which allows the conformal coverage of even high aspect nanostructure with minimal shape distortion. It is shown that the ALD process is applicable to different types of precursors. This decouples the processes of geometrical fabrication and material response. The precursor can be chosen according to availability, deposition rate or performance while the plasmonic response is determined by the additional ALD layer. In general ALD allows for coverage of any 3D structure and is therefore a good match to the flexible EBID process. While in this thesis an ALD-platinum precursor was used to form metal shells on EBID structures the development of new ALD-precursors might in the future also enable other noble metal to be added on EBID by ALD. Planar ALD-platinum layers are characterized by electrical and optical measurements showing that platinum of very pure quality is deposited. While the EBID-platinum consists to a high fraction of carbon and is therefore dielectric, the ALD-platinum is purely metallic. Simulations suggest that the influence of the remaining EBID core when depositing a 20nm ALD-platinum shell is of minor importance to the optical performance. Similar to the EBID-gold covered by an evaporated gold shell, also in this case the core-shell structures shows an improved optical response in comparison to as-deposited structures. While EBID-platinum structures show only a weak polarization dependence in transmission, only visible when measured in an array [13], the ALD-platinum coverage allows the optical investigation of single platinum helices, shown for the first time in this thesis. The dissymmetry of a single helix with a dissymmetry factor with a maximum value of around 0.06 at 700 nm is measured. The dissymmetry spectra looks similar to the one obtained from arrays. An interesting question that arises is at what distance in an array interactions between the helices start to change the optical response. The EBID process also allows for an easy arrangement of helices in specially designed arrays e.g. feature rotational symmetry. It has been shown that this lateral arrangement can improve the circular dichroism and minimize the conversion from one polarization state to the other [175]. Therefore specially designed arrays of ALD-coated EBID nanostructures would allow for an even higher optical response.

In addition of the deposition of an additional pure metal layer, purification on EBID deposits is investigated in this thesis. Purification of EBID-gold in an oxygen plasma shows the formation of a core-shell structure similar to e-beam evaporation. The outer part of the helix is purified to a high degree. Electrical and optical measurements show that the shell material behaves like pure gold. During purification the thickness of EBID-gold pads and the size of EBID-gold helices is reduced due to the removal of carbon. However, in this thesis it shows that the shape of highly 3D nanostructures could be maintained throughout the purification process for structures with the smallest wire thicknesses of 80 nm. For smaller sizes deformation occurs in the case of 3D structure while the purification of thin planar structures lead to the formation of voids. The promising results from this ex situ, easy to implement purification with a standard table top plasma cleaner could in future be applied to even more complex three dimensional structures.

This is especially interesting for intertwined helices, since these structures cannot be conformally coated by evaporation because of shadowing effects. However, these intertwined helices promise to have large chiral fields in their proximity, which could be used for chiral molecule detection [176]. Besides purification, this thesis shows for the first time metal ALD-coating of EBID-nanostructures, which might be very promising for these structures as during the ALD process no shadowing occurs.

Kurzfassung

Elektronenstrahl induzierte Abscheidung (EBID) ist eine 3D Drucktechnik mit Auflösung im Nanometerbereich. Die Möglichkeit Material strukturiert abzuscheiden, erlaubt die optischen Eigenschaften nach Bedarf anzupassen. Eine Vielzahl von Ausgangsstoffen für EBID wurden hinsichtlich ihrer chemischen und elektrischen Eigenschaften untersucht. Jedoch wurde EBID nur selten als Herstellungsmethode für Nanooptik oder Plasmonik eingesetzt. Der Hauptgrund ist der hohe Kohlenstoffgehalt in EBID-Strukturen aus metal-organischen Ausgangsstoffen. Diese Arbeit trägt zur Entwicklung neuer Ausgangsstoffe, dem Verständnis der optischen Eigenschaften un-modifizierter EBID-Abscheidungen, sowie der Untersuchung zusätzlicher Prozessschritte zur Verbesserung der optischen Eigenschaften von plasmonischen EBID-Abscheidungen bei.

Optische Untersuchungen der Permittivität an einem häufig verwendeten Platin sowie an einen neuartigen Kupfer Ausgangsstoff zeigen ein dielektrisches Verhalten der EBID-Abscheidungen und können durch ein Maxwell-Garnett Model angenähert werden. Das EBID-Kupfer weist einen vielversprechend hohen Kupferanteil von 24 at.% auf. Jedoch zeigen die optische Untersuchungen, dass trotz des hohen Kupfergehalts die Permittivität des Materials hauptsächlich durch den Kohlenstoff und dessen chemische Konfiguration bestimmt wird.

Das optische Verhalten von EBID-Nanostrukturen kann durch eine geschlossene Metallschicht verbessert werden. Hierfür werden zwei Ansätze verfolgt; Aufbringen einer zusätzlichen puren Metallschicht und Aufreinigung der EBID-Abscheidungen. Der Vergleich von Dunkelfeldstreuung und polarisationsabhängiger Transmission mit Simulationen an einer EBID-Helix zeigt, dass eine 20 nm dicke Goldhülle, abgeschieden mit Elektronenstrahl-Verdampfung, zum selben Verhalten führt wie eine reine Goldhelix. Der Grund hierfür ist die geringe Eindringtiefe des Lichtes in das Gold. Eine Helix mit drei Windungen zeigt einen asymmetrischen Transmissionsfaktor von 0.03 bei 600 nm. Zum ersten Mal wird die Atomlagenabscheidung (ALD) zur Beschichtung von 3D EBID-Strukturen untersucht. Im Gegensatz zur Verdampfung erlaubt ALD konforme Beschichtung von komplexen Strukturen. ALD-Platin zeigt in elektrischen und optischen Messungen ein rein metallisches Verhalten. Die Kombination aus EBID-Platin beschichtet mit ALD-Platin erlaubt die Untersuchung einer einzelner Platinhelix, welche sich wie eine Helix aus reinem Platin verhält. Solch eine Helix zeigt einen asymmetrischen Transmissionsfaktor von 0.06 bei 700 nm. Zusätzlich wird in dieser Arbeit die Aufreinigung von EBID Abscheidungen untersucht, um deren Metallgehalt zu erhöhen. Durch Sauerstoffplasma Aufreinigung wird der Kohlenstoffgehalt in der äußeren Schicht von goldhaltigen EBID-Abscheidungen deutlich reduziert. Elektrische und optische Messungen, sowie der Vergleich mit Simulationen, deuten auf eine fast pure Goldschicht hin, vergleichbar mit den beschichteten Goldhelices. Obwohl die EBID-Strukturen sich während des Plasmaprozesses verkleinern, behalten sie ihre 3D Form bei.

Abstract

Electron beam induced deposition (EBID) is a 3D printing technique with a resolution in the nanometer range. With its capability of structured deposition, the optical properties of materials can be tailored. A variety of precursor for EBID has been characterized by their chemical and electrical properties. However, EBID has been used only in few cases as a fabrication tool for nanooptics or plasmonics. The main drawback is the high carbon content in most EBID deposits from metal-organic precursors. This thesis aims at contributing to the development of new precursors, optical understanding of as-deposited EBID materials and investigation of additional steps that can improve the optical performance of plasmonic structures fabricated by EBID.

The optical investigation of the permittivity of deposits from a commonly used platinum and a novel copper containing precursor shows that the EBID material is dielectric and can be approximated by a Maxwell-Garnet mixing model. The EBID-copper shows a promisingly high copper content of around 24 at.%. However the optical characterization of the material shows that despite the high metal content, the permittivity of the material is mainly determined by the carbon matrix and its chemical configuration.

To increase the optical performance of plasmonic EBID nanostructures a closed metal shell has to be achieved. This is attempted by two different methods; post-coating of the deposited nanostructure with a pure metal or purification of the nanostructure itself. For single EBID-gold helices e-beam evaporation is investigated as post-coating method. Comparison of darkfield scattering and polarization dependent transmission, of a helix coated with 20 nm gold with simulations show that the core-shell helix acts like a solid gold one. This is due to the limited penetration depth of visible light into gold. A three pitch gold helix exhibits a dissymmetry factor of 0.03 around 600 nm. In this thesis for the first time, atomic layer deposition (ALD) has been investigated for coating of 3D EBID nanostructures. In contrast to metal evaporation ALD allows conformal coating of complex geometries. For EBID-platinum deposits a platinum ALD process has been developed. Electrical and optical measurements prove that the ALD-platinum is pure metallic. The combination of EBID-platinum covered by ALD-platinum allows optical investigation of a single platinum helix, plasmonically behaving like pure metal. Such a platinum helix shows a maximum dissymmetry factor of 0.06 around 700 nm. Additionally in this thesis EBID nanostructures themselves are purification to increase the metal content. By post oxygen plasma purification the carbon content in the outer shell of EBID-gold deposits can strongly be reduced. Electrical measurement as well as optical measurements in comparison to simulations point at an almost pure outer gold shell, comparable to EBID nanostructures coated by pure gold. While EBID nanostructures shrink during plasma purification their 3D geometric shape can be maintained.

Publication

C. Haverkamp, K. Höflich, S. Jäckle, A. Manzoni and S. Christiansen, *Plasmonic gold helices for the visible range fabricated by oxygen plasma purification of electron beam induced deposits*, *Nanotechnology* **28** (2016), 055303, <http://dx.10.1088/1361-6528/28/5/055303>

References

- [1] B. Berman. 3-D printing: The new industrial revolution. *Business Horizons*, 55(2):155–162, 2012.
- [2] Create it REAL Aps. www.createitreal.com/index.php/technology/process.
- [3] S. V. Murphy and A. Atala. 3D bioprinting of tissues and organs. *Nature biotechnology*, 32(8):773–785, 2014.
- [4] T. Gissibl, S. Thiele, A. Herkommer, and H. Giessen. Two-photon direct laser writing of ultracompact multi-lens objectives. *Nature Photonics*, 10(8):554–560, 2016.
- [5] S. Matsui. Springer Handbook of Nanotechnology. chapter 7, pages 211–229. Springer-Verlag Berlin Heidelberg, 2010.
- [6] A. Szkudlarek, W. Szmyt, C. Kapusta, and I. Utke. Lateral resolution in focused electron beam-induced deposition: scaling laws for pulsed and static exposure. *Applied Physics A*, 117(4):1715–1726, 2014.
- [7] B.B. Lewis, R. Winkler, X. Sang, P. R. Pudasaini, M. G. Stanford, H. Plank, R. R. Unocic, J. D. Fowlkes, and P. D. Rack. 3D Nanoprinting via laser-assisted electron beam induced deposition: growth kinetics, enhanced purity, and electrical resistivity. *Beilstein Journal of Nanotechnology*, 8:801–812, 2017.
- [8] I. Utke, P. Hoffmann, and J. Melngailis. Gas-assisted focused electron beam and ion beam processing and fabrication. *Journal of Vacuum Science & Technology B: Microelectronics and Nanometer Structures*, 26(4):1197, 2008.
- [9] Sir J. Pendry. Metamaterials and the Control of Electromagnetic Fields. In *Conference on Coherence and Quantum Optics*, page CMB2, Washington, D.C., 2007. OSA.
- [10] S. A. Maier and H. Atwater. Plasmonics: Localization and guiding of electromagnetic energy in metal/dielectric structures. *Journal of Applied Physics*, 98(1):011101, 2005.

REFERENCES

- [11] G. Mie. Beiträge zur Optik trüber Medien, speziell kolloidaler Metallösungen. *Annalen der Physik*, 330(3):377–445, 1908.
- [12] W. F. Van Dorp and C. W. Hagen. A critical literature review of focused electron beam induced deposition. *Journal of Applied Physics*, 104(8):081301, 2008.
- [13] M. Esposito, V. Tasco, F. Todisco, A. Benedetti, D. Sanvitto, and A. Passaseo. Three Dimensional Chiral Metamaterial Nanospirals in the Visible Range by Vertically Compensated Focused Ion Beam Induced-Deposition. *Advanced Optical Materials*, 2(2):154–161, 2014.
- [14] A. S. Maier. *Plasmonic Fundamentals and Applications*. Springer Science+Business Media LLC, 2007.
- [15] W. Demtröder. *Experimentalphysik 2*. Springer-Verlag Berlin Heidelberg, 4 edition, 2006.
- [16] R. P. Feynman, R.B. Leighton, and M. Sands. *Feynman Lectures on Physics*. California Institute of Technology, new millen edition, 2010.
- [17] Z. Li, M. Mutlu, and E. Ozbay. Chiral metamaterials: from optical activity and negative refractive index to asymmetric transmission. *Journal of Optics*, 15(2):023001, 2013.
- [18] N.D. Ashcroft, N.W. Mermin. *Solid State Physics*. Saunders College, 1976.
- [19] A. D. Rakić, A. B. Djurišić, J.M. Elazar, and M. L. Majewski. Optical properties of metallic films for vertical-cavity optoelectronic devices. *Applied Optics*, 37(22):5271, aug 1998.
- [20] P. B. Johnson and R. W. Christy. Optical Constants of the Noble Metals. *Physical Review B*, 6(12):4370–4379, 1972.
- [21] R. Ruppin. Evaluation of extended Maxwell-Garnett theories. *Optics Communications*, 182(4-6):273–279, 2000.
- [22] V. A. Markel. Introduction to the Maxwell Garnett approximation: tutorial. *Journal of the Optical Society of America A*, 33(7):1244, 2016.
- [23] D. E. Aspnes. Local field effects and effective medium theory A microscopic perspective. *American Journal of Physics*, 50(8):704–709, 1982.
- [24] G. A. Niklasson, C. G. Granqvist, and O. Hunderi. Effective medium models for the optical properties of inhomogeneous materials. *Applied Optics*, 20(1):26, 1981.

-
- [25] D. W. Hahn. *Light Scattering Theory*. University of Florida, 2009.
- [26] M. M. Shawrav, P. Taus, H. D. Wanzenboeck, M. Schinnerl, M. Stöger-Pollach, S. Schwarz, A. Steiger-Thirsfeld, and Emmerich Bertagnoli. Highly conductive and pure gold nanostructures grown by electron beam induced deposition. *Scientific Reports*, 6(1):34003, 2016.
- [27] A. J. Cox, A. J. DeWeerd, and J. Linden. An experiment to measure Mie and Rayleigh total scattering cross sections. *American Journal of Physics*, 70(6):620–625, 2002.
- [28] A. L. Aden and M. Kerker. Scattering of Electromagnetic Waves from Two Concentric Spheres. *Journal of Applied Physics*, 22(10):1242–1246, 1951.
- [29] C. F. Bohren and D. R. Huffman. *Absorption and Scattering of Light by Small Particles*, volume 1. Wiley-VCH Verlag GmbH, Weinheim, Germany, 1998.
- [30] P. Laven. MiePlot, <http://philiplaven.com/mieplot.htm>.
- [31] L. Saviot. Mie scattering calculator, <http://lucien.saviot.free.fr/index.en.html>.
- [32] K. HUANG. Lattice Vibrations and Optical Waves in Ionic Crystals. *Nature*, 167(4254):779–780, 1951.
- [33] J. Olson, S. Dominguez-Medina, A. Hoggard, L.Y. Wang, W.S. Chang, and S. Link. Optical characterization of single plasmonic nanoparticles. *Chem. Soc. Rev.*, 44(1):40–57, 2015.
- [34] R. Wegerhoff, O. Weidlich, and M. Kässens. *Basics of Light Microscopy & Imaging*. Git Verlag, 2008.
- [35] G. Brönstrup, C. Leiterer, N. Jahr, C. Gutsche, A. Lysov, I. Regolin, W. Prost, F. J. Tegude, W. Fritzsche, and S. Christiansen. A precise optical determination of nanoscale diameters of semiconductor nanowires. *Nanotechnology*, 22(38):385201, 2011.
- [36] P. Woźniak, K. Höflich, G. Brönstrup, P. Banzer, S. Christiansen, and G. Leuchs. Unveiling the optical properties of a metamaterial synthesized by electron-beam-induced deposition. *Nanotechnology*, 27(2):025705, 2016.
- [37] M. Losurdo and K. Hingerl. *Ellipsometry at the Nanoscale*. Springer-Verlag Berlin Heidelberg, Berlin, Heidelberg, 2013.
- [38] J. R. Ferraro, K. Nakamoto, and C. W. Brown. *Introductory Raman Spectroscopy*. Elsevier science, 2 edition, 1994.

REFERENCES

- [39] A. Cantarero. Raman Scattering Applied to Materials Science. *Procedia Materials Science*, 9:113–122, 2015.
- [40] J. Parsons, C .P. Burrows, J.R. Sambles, and W. L. Barnes. A comparison of techniques used to simulate the scattering of electromagnetic radiation by metallic nanostructures. *Journal of Modern Optics*, 57(5):356–365, 2010.
- [41] B.T. Draine and P.J. Flatau. Discrete-Dipole Approximation For Scattering Calculations. *Journal of the Optical Society of America A*, 11(4):1491, 1994.
- [42] J. Jin. *The Finite Element Method in Electromagnetics*. John Wiley & Sons, 2002.
- [43] A. Taflove and S.C. Hagness. *Computational Electrodynamics the Finite Difference Time Domain Methods*. Artech House, 2000.
- [44] Y Kane. Numerical solution of initial boundary value problems involving maxwell’s equations in isotropic media. *IEEE Transactions on Antennas and Propagation*, 14(3):302–307, 1966.
- [45] A.C. Cangellaris and D.B. Wright. Analysis of the numerical error caused by the stair-stepped approximation of a conducting boundary in FDTD simulations of electromagnetic phenomena. *IEEE Transactions on Antennas and Propagation*, 39(10):1518–1525, 1991.
- [46] B. Gallinet, J. Butet, and O. J. F. Martin. Numerical methods for nanophotonics: standard problems and future challenges. *Laser & Photonics Reviews*, 9(6):577–603, 2015.
- [47] L. Jiang, T. Yin, Z. Dong, M. Liao, S. J. Tan, X. M. Goh, D. Allieux, H. Hu, X. Li, J. K. W. Yang, and Z. Shen. Accurate Modeling of Dark-Field Scattering Spectra of Plasmonic Nanostructures. *ACS Nano*, 9(10):10039–10046, oct 2015.
- [48] COMSOL MULTIPHYSICS. <https://www.comsol.com>.
- [49] K. Höflich. *Plasmonische Eigenschaften von metallhaltigen Nanostrukturen*. PhD thesis, Martin-Luther-Universität Halle-Wittenberg, 2011.
- [50] L. Reimer. *Scanning Electron Microscopy*, volume 45 of *Springer Series in Optical Sciences*. Springer Berlin Heidelberg, Berlin, Heidelberg, 2 edition, 1998.
- [51] D.B. Williams and C. B. Carter. The Transmission Electron Microscope. In *Transmission Electron Microscopy*, pages 3–22. Springer US, Boston, MA, 2009.
- [52] modularflow. <http://www.modularflow.com/>.

-
- [53] I. Utke, S. Moshkalev, and P. Russell, editors. *Nanofabrication using focused ion and electron beams: principles and applications*. Oxford University Press, 2012.
- [54] J. D. Wnuk, J. M. Gorham, S. G. Rosenberg, W. F. Van Dorp, T. E. Madey, C. W. Hagen, and D. H. Fairbrother. Electron beam irradiation of dimethyl-(acetylacetonate) gold(III) adsorbed onto solid substrates. *Journal of Applied Physics*, 107(5):054301, 2010.
- [55] J.D. Wnuk, S.G. Rosenberg, J.M. Gorham, W.F. van Dorp, C.W. Hagen, and D.H. Fairbrother. Electron beam deposition for nanofabrication: Insights from surface science. *Surface Science*, 605(3-4):257–266, feb 2011.
- [56] A. Riazanova. *Direct Nanoprototyping of Functional Materials via Focused Electron Beam*. PhD thesis, KTH-Royal Institute of Technology, 2013.
- [57] J. D. Fowlkes, S. J. Randolph, and P. D. Rack. Growth and simulation of high-aspect ratio nanopillars by primary and secondary electron-induced deposition. *Journal of Vacuum Science & Technology B: Microelectronics and Nanometer Structures*, 23(6):2825, 2005.
- [58] K. Höflich, R. B. Yang, A. Berger, G. Leuchs, and S. Christiansen. The Direct Writing of Plasmonic Gold Nanostructures by Electron-Beam-Induced Deposition. *Advanced Materials*, 23(22-23):2657–2661, 2011.
- [59] J. D. Wnuk, J. M. Gorham, S. G. Rosenberg, W. F. van Dorp, T. E. Madey, C. W. Hagen, and D. H. Fairbrother. Electron Induced Surface Reactions of the Organometallic Precursor Trimethyl(methylcyclopentadienyl)platinum(IV). *The Journal of Physical Chemistry C*, 113(6):2487–2496, 2009.
- [60] M. Huth, F. Porrati, C. Schwalb, M. Winhold, R. Sachser, M. Dukic, J. Adams, and G. Fantner. Focused electron beam induced deposition: A perspective. *Beilstein Journal of Nanotechnology*, 3:597–619, 2012.
- [61] D. Drouin, A.R. Couture, D. Joly, X. Tastet, V. Aimez, and R. Gauvin. CASINO A Fast and Easy to use Modeling Tool for Scanning Electron Microscopy and Microanalysis. 29:92–101, 2007.
- [62] I. Utke, P. Hoffmann, B. Dwir, K. Leifer, E. Kapon, and P. Doppelt. Focused electron beam induced deposition of gold. *Journal of Vacuum Science & Technology B: Microelectronics and Nanometer Structures*, 18(6):3168, 2000.
- [63] A. Botman. *Towards high purity nanostructures from electron beam induced deposition of platinum*. PhD thesis, TU Delft, 2009.

REFERENCES

- [64] A. Botman, M. Hesselberth, and J.J.L. Mulders. Improving the conductivity of platinum-containing nano-structures created by electron-beam-induced deposition. *Microelectronic Engineering*, 85(5-6):1139–1142, 2008.
- [65] E. Villamor, F. Casanova, P. H. F. Trompenaars, and J. J. L. Mulders. Embedded purification for electron beam induced Pt deposition using MeCpPtMe 3. *Nanotechnology*, 26(9):095303, 2015.
- [66] S. Frabboni, G.C. Gazzadi, and A. Spessot. TEM study of annealed Pt nanostructures grown by electron beam-induced deposition. *Physica E: Low-dimensional Systems and Nanostructures*, 37(1-2):265–269, 2007.
- [67] S. Mehendale, J. J. L. Mulders, and P. H. F. Trompenaars. A new sequential EBID process for the creation of pure Pt structures from MeCpPtMe 3. *Nanotechnology*, 24(14):145303, 2013.
- [68] D. Belic, M. M. Shawrav, M. Gavagnin, M. Stoger-Pollach, H.D. Wanzenboeck, and E. Bertagnolli. Direct-Write Deposition and Focused-Electron-Beam-Induced Purification of Gold Nanostructures. *ACS Applied Materials & Interfaces*, 7(4):2467–2479, 2015.
- [69] A. V. Riazanova, J. J. L. Mulders, and M. B. Lyubov. Creation of patterned gold nanostructures via electron-beam-induced deposition. *Materials Research Society*, 1:0–5, 2013.
- [70] M.G. Stanford, B.B. Lewis, J.H. Noh, J. D. Fowlkes, N. A. Roberts, H. Plank, and P. D. Rack. Purification of Nanoscale Electron-Beam-Induced Platinum Deposits via a Pulsed Laser-Induced Oxidation Reaction. *ACS Applied Materials & Interfaces*, 6(23):21256–21263, 2014.
- [71] C. Langhammer, Z. Yuan, I. Zoric, and B. Kasemo. Plasmonic Properties of Supported Pt and Pd Nanostructures. *Nano Letters*, 6(4):833–838, 2006.
- [72] I. Zoric, M. Zach, B. Kasemo, and C. Langhammer. Gold, Platinum, and Aluminum Nanodisk Plasmons: Material Independence, Subradiance, and Damping Mechanisms. *ACS Nano*, 5(4):2535–2546, apr 2011.
- [73] S. Baldelli, A. S. Eppler, E. Anderson, Y.R. Shen, and G.A. Somorjai. Surface enhanced sum frequency generation of carbon monoxide adsorbed on platinum nanoparticle arrays. *The Journal of Chemical Physics*, 113(13):5432, 2000.
- [74] N. D. Israelsen, C. Hanson, and E. Vargis. Nanoparticle Properties and Synthesis Effects on Surface-Enhanced Raman Scattering Enhancement Factor: An Introduction. *The Scientific World Journal*, 2015:1–12, 2015.

- [75] H. Xu, J. Aizpurua, M. Käll, and P. Apell. Electromagnetic contributions to single-molecule sensitivity in surface-enhanced Raman scattering. *Physical Review E*, 62(3):4318–4324, 2000.
- [76] K. Ikeda, J. Sato, N. Fujimoto, N. Hayazawa, S. Kawata, and K. Uosaki. Plasmonic Enhancement of Raman Scattering on Non-SERS-Active Platinum Substrates. *The Journal of Physical Chemistry C*, 113(27):11816–11821, 2009.
- [77] H. Plank, T. Haber, C. Gspan, G. Kothleitner, and F. Hofer. Chemical tuning of PtC nanostructures fabricated via focused electron beam induced deposition. *Nanotechnology*, 24(17):175305, may 2013.
- [78] M. Esposito, V. Tasco, M. Cuscunà, F. Todisco, A. Benedetti, I. Tarantini, M. D. Giorgi, D. Sanvitto, and A. Passaseo. Nanoscale 3D Chiral Plasmonic Helices with Circular Dichroism at Visible Frequencies. *ACS Photonics*, 2(1):105–114, 2015.
- [79] M. Esposito, V. Tasco, F. Todisco, M. Cuscunà, A. Benedetti, D. Sanvitto, and A. Passaseo. Triple-helical nanowires by tomographic rotatory growth for chiral photonics. *Nature Communications*, 6:6484, 2015.
- [80] A. Botman, J. J. L. Mulders, and C. W. Hagen. Creating pure nanostructures from electron-beam-induced deposition using purification techniques: a technology perspective. *Nanotechnology*, 20(37):372001, 2009.
- [81] V. Friedli, I. Utke, K. Molhave, and J. Michler. Dose and energy dependence of mechanical properties of focused electron-beam-induced pillar deposits from $\text{Cu}(\text{C}_5\text{HF}_6\text{O}_2)_2$. *Nanotechnology*, 20(38):385304, 2009.
- [82] J. Robertson. Diamond-like amorphous carbon. *Materials Science and Engineering Reports*, 37(4-6):129–281, 2002.
- [83] A. C. Ferrari and J. Robertson. Interpretation of Raman spectra of disordered and amorphous carbon. *Physical Review B*, 61(20):14095–14107, 2000.
- [84] L. G. Canado, K. Takai, T. Enoki, M. Endo, Y. A. Kim, H. Mizusaki, A. Jorio, L. N. Coelho, R. Magalhães-Paniago, and M. A. Pimenta. General equation for the determination of the crystallite size l_a of nanographite by Raman spectroscopy. *Applied Physics Letters*, 88(16):12–14, 2006.
- [85] F. Tuinstra and J. L. Koenig. Raman Spectrum of Graphite. *The Journal of Chemical Physics*, 53(3):1126–1130, 1970.

REFERENCES

- [86] F. Porrati, R. Sachser, C. H. Schwalb, A. S. Frangakis, and M. Huth. Tuning the electrical conductivity of Pt-containing granular metals by postgrowth electron irradiation. *Journal of Applied Physics*, 109(6):063715, 2011.
- [87] D. D. Kulkarni, K. Rykaczewski, S. Singamaneni, S. Kim, A.G. Fedorov, and V. Tsukruk. Thermally Induced Transformations of Amorphous Carbon Nanostructures Fabricated by Electron Beam Induced Deposition. *ACS Applied Materials & Interfaces*, 3(3):710–720, 2011.
- [88] M. V. Puydinger dos Santos, M. F. Velo, R. D. Domingos, Y. Zhang, X. Maeder, C. Guerra-Nunez, J.P. Best, F. Beron, K. R. Pirota, S. Moshkalev, J.A. Diniz, and I. Utke. Annealing-Based Electrical Tuning of Cobalt Carbon Deposits Grown by Focused-Electron-Beam-Induced Deposition. *ACS Applied Materials & Interfaces*, 8(47):32496–32503, 2016.
- [89] Principles of Nulling and Imaging Ellipsometry. <https://www.accurion.com/imaging-ellipsometry>, 2002.
- [90] H.J. Hagemann, W. Gudat, and C. Kunz. Optical constants from the far infrared to the x-ray region: Mg, Al, Cu, Ag, Au, Bi, C, and Al₂O₃. *Journal of the Optical Society of America*, 65(6):742, 1975.
- [91] E.K. Lee, J.H. Song, K.Y. Jeong, J. H. Kang, H. G. Park, and M. K. Seo. Resonant light scattering from a single dielectric nano-antenna formed by electron beam-induced deposition. *Scientific Reports*, 5(1):10400, 2015.
- [92] G. Adamopoulos, C. Godet, B. Drevillon, Y. Saito, D.N. Batchelder, Annie Grosman, and C. Ortega. ECR deposition of hydrogenated diamond-like amorphous carbon films using acetylene oxygen plasmas. *Diamond and Related Materials*, 12(3-7):983–987, 2003.
- [93] G.V. Naik, V. M. Shalaev, and A. Boltasseva. Alternative Plasmonic Materials: Beyond Gold and Silver. *Advanced Materials*, 25(24):3264–3294, 2013.
- [94] P.R. West, S. Ishii, G.V. Naik, N.K. Emani, V.M. Shalaev, and A. Boltasseva. Searching for better plasmonic materials. *Laser & Photonics Reviews*, 4(6):795–808, 2010.
- [95] I. Utke, P. Hoffmann, B. Dwir, K. Leifer, E. Kapon, and P. Doppelt. Focused electron beam induced deposition of gold. *Journal of Vacuum Science & Technology B: Microelectronics and Nanometer Structures*, 18(6):3168, 2000.
- [96] I. Utke, B. Dwir, K. Leifer, F. Cicoira, P. Doppelt, P. Hoffmann, and E Kapon. Electron beam induced deposition of metallic tips and wires for microelectronics applications. *Microelectronic Engineering*, 53(1-4):261–264, 2000.

-
- [97] A. V Riazanova, Y.G.M. Rikers, J. J. L. Mulders, and L. M. Belova. Pattern Shape Control for Heat Treatment Purification of Electron-Beam-Induced Deposition of Gold from the Me 2 Au(acac) Precursor. *Langmuir*, 28(14):6185–6191, 2012.
- [98] S. Graells, R. Alcubilla, G. Badenes, and R. Quidant. Growth of plasmonic gold nanostructures by electron beam induced deposition. *Applied Physics Letters*, 91(12):121112, sep 2007.
- [99] I.S. Beloborodov, A.V. Lopatin, and V.M. Vinokur. Granular electronic systems. *Reviews of Modern Physics*, 79(June):469–518, 2007.
- [100] M. Huth, F. Kolb, and H. Plank. Dielectric sensing by charging energy modulation in a nano-granular metal. *Applied Physics A: Materials Science & Processing*, pages 1689–1696, 2014.
- [101] H. Plank, C. Gspan, M. Dienstleder, G. Kothleitner, and F. Hofer. The influence of beam defocus on volume growth rates for electron beam induced platinum deposition. *Nanotechnology*, 19(48):485302, 2008.
- [102] H. Plank, D.A. Smith, T. Haber, P. D. Rack, and F. Hofer. Fundamental proximity effects in focused electron beam induced deposition. *ACS Nano*, 6(1):286–294, 2012.
- [103] P. Denniger. Herstellung und optische Charakterisierung von Nanostrukturen. *Bachelor Thesis*, 2016.
- [104] A. Anyadike. *Copper a material for new millenium*. Woodhead Publishing Limited, 2002.
- [105] A. Vilà, F. Hernández-Ramirez, J. Rodríguez, O. Casals, A. Romano-Rodríguez, J.R. Morante, and M. Abid. Fabrication of metallic contacts to nanometre-sized materials using a focused ion beam (FIB). *Materials Science and Engineering: C*, 26(5-7):1063–1066, 2006.
- [106] D. Brunel, D. Troadec, D. Hourlier, D. Deresmes, M. Zdrojek, and T. Mélin. Characterization of ion/electron beam induced deposition of electrical contacts at the sub- μm scale. *Microelectronic Engineering*, 88(7):1569–1572, 2011.
- [107] J. D. Fowlkes, B. Geier, B. B. Lewis, P. D. Rack, M. G. Stanford, R. Winkler, and H. Plank. Electron nanoprobe induced oxidation: a simulation of direct-write purification. *Phys. Chem. Chem. Phys.*, 17(28):18294–18304, 2015.

REFERENCES

- [108] G. H. Chan, J. Zhao, E. M. Hicks, G. C. Schatz, and R. P. Van Duyne. Plasmonic Properties of Copper Nanoparticles Fabricated by Nanosphere Lithography. *Nano Letters*, 7(7):1947–1952, 2007.
- [109] Periodic table. <http://www.rsc.org/periodic-table>.
- [110] M. Hu, J. Chen, Z.Y. Li, L. Au, G.V. Hartland, X. Li, M. Marquez, and Y. Xia. Gold nanostructures: engineering their plasmonic properties for biomedical applications. *Chemical Society Reviews*, 35(11):1084, 2006.
- [111] T. R. Jensen, M. D. Malinsky, C. L. Haynes, and R. P. Van Duyne. Nanosphere Lithography: Tunable Localized Surface Plasmon Resonance Spectra of Silver Nanoparticles. *The Journal of Physical Chemistry B*, 104(45):10549–10556, 2000.
- [112] C. Fang, Y. H. Lee, L. Shao, R. Jiang, J. Wang, and Q.H. Xu. Correlating the Plasmonic and Structural Evolutions during the Sulfidation of Silver Nanocubes. *ACS Nano*, 7(10):9354–9365, 2013.
- [113] J.H. Kim, S. H. Ehrman, and T. A. Germer. Influence of particle oxide coating on light scattering by submicron metal particles on silicon wafers. *Applied Physics Letters*, 84(8):1278–1280, 2004.
- [114] S. Wang, X. Huang, Y. He, H. Huang, Y. Wu, L. Hou, X. Liu, T. Yang, J. Zou, and B. Huang. Synthesis, growth mechanism and thermal stability of copper nanoparticles encapsulated by multi-layer graphene. *Carbon*, 50(6):2119–2125, 2012.
- [115] Y. Ochiai. Electron-beam-induced deposition of copper compound with low resistivity. *Journal of Vacuum Science & Technology B: Microelectronics and Nanometer Structures*, 14(6):3887, 1996.
- [116] A. Luisier, I. Utke, T. Bret, F. Cicoira, R. Hauert, S.-W. Rhee, P. Doppelt, and P. Hoffmann. Comparative Study of Cu-Precursors for 3D Focused Electron Beam Induced Deposition. *Journal of The Electrochemical Society*, 151(9):C590, 2004.
- [117] A. Devi, J. Goswami, R. Lakshmi, S. A. Shivashankar, and S. Chandrasekaran. A novel Cu(II) chemical vapor deposition precursor: Synthesis, characterization, and chemical vapor deposition. *Journal of Materials Research*, 13(03):687–692, 1998.
- [118] S. Mezheny, I. Lyubinetsky, W. J. Choyke, and J. T. Yates. Electron stimulated decomposition of adsorbed hexafluoroacetylacetonate Cu(I) vinyltrimethylsilane, Cu(I)(hfac)(vtms). *Journal of Applied Physics*, 85(6):3368–3373, 1999.

- [119] I. Utke, V. Friedli, M. Purrucker, and J. Michler. Resolution in focused electron- and ion-beam induced processing. *Journal of Vacuum Science & Technology B: Microelectronics and Nanometer Structures*, 25(6):2219, 2007.
- [120] T. Bret, I. Utke, and P. Hoffmann. Influence of the beam scan direction during focused electron beam induced deposition of 3D nanostructures. *Microelectronic Engineering*, 78-79(1-4):307–313, 2005.
- [121] A. Botman, J. J. L. Mulders, R. Weemaes, and S. Mentink. Purification of platinum and gold structures after electron-beam-induced deposition. *Nanotechnology*, 17(15):3779–3785, 2006.
- [122] A. Singhal, M. R. Pai, R. Rao, K. T. Pillai, I. Lieberwirth, and A. K. Tyagi. Copper(I) Oxide Nanocrystals - One Step Synthesis, Characterization, Formation Mechanism, and Photocatalytic Properties. *European Journal of Inorganic Chemistry*, 2013(14):2640–2651, 2013.
- [123] William M. Haynes, editor. *Handbook of Chemistry and Physics*. Taylor & Francis, 97 edition, 2016.
- [124] S. F. Durrant, S. G. Castro, J. I. Cisneros, N. C. da Cruz, and M. A. Bica de Moraes. Amorphous oxygen containing hydrogenated carbon films formed by plasma enhanced chemical vapor deposition. *Journal of Vacuum Science & Technology A: Vacuum, Surfaces, and Films*, 14(1):118–124, 1996.
- [125] E. Prodan. A Hybridization Model for the Plasmon Response of Complex Nanostructures. *Science*, 302(5644):419–422, 2003.
- [126] S. F. Shayesteh and M. Saie. The effect of surface plasmon resonance on optical response in dielectric (core) metal (shell) nanoparticles. *Pramana*, 85(6):1245–1255, 2015.
- [127] H. Acar, T. Coenen, A. Polman, and L. K. Kuipers. Dispersive Ground Plane Core Shell Type Optical Monopole Antennas Fabricated with Electron Beam Induced Deposition. *ACS Nano*, 6(9):8226–8232, 2012.
- [128] H. Acar. *Fabrication of plasmonic nanostructures with electron beam induced deposition*. PhD thesis, Tu Delft, 2013.
- [129] M. Esposito, V. Tasco, F. Todisco, M. Cuscunà, A. Benedetti, M. Scuderi, G. Nicotra, and A. Passaseo. Programmable Extreme Chirality in the Visible by Helix-Shaped Metamaterial Platform. *Nano Letters*, 16(9):5823–5828, sep 2016.

REFERENCES

- [130] J. K. Gansel, M. Wegener, S. Burger, and S. Linden. Gold helix photonic metamaterials: A numerical parameter study. *Optics Express*, 18(2):1059, 2010.
- [131] S. Link and M. A. El-Sayed. Simulation of the Optical Absorption Spectra of Gold Nanorods as a Function of Their Aspect Ratio and the Effect of the Medium Dielectric Constant. *The Journal of Physical Chemistry B*, 109(20):10531–10532, 2005.
- [132] Z. Y. Zhang and Y. P. Zhao. The visible extinction peaks of Ag nanohelices: A periodic effective dipole model. *Applied Physics Letters*, 98(8), 2011.
- [133] D. Kusters, A. De Hoogh, H. Zeijlemaker, N. Rotenberg, and L. Kuipers. Core-shell plasmonic nanohelices. *ACS Photonics*, doi: 10.10(just accepted), 2017.
- [134] B. Frank, X. Yin, M. Schäferling, J. Zhao, S. M. Hein, P.V. Braun, and H. Giessen. Large-Area 3D Chiral Plasmonic Structures. *ACS Nano*, 7(7):6321–6329, jul 2013.
- [135] J. K. Gansel, M. Thiel, M.S. Rill, M. Decker, K. Bade, V. Saile, G. Von Freymann, S. Linden, and M. Wegener. Gold Helix Photonic Metamaterial as Broadband Circular Polarizer. *Science*, 325(5947):1513–1515, 2009.
- [136] X. Yin, M. Schäferling, B. Metzger, and H. Giessen. Interpreting Chiral Nanophotonic Spectra: The Plasmonic Born Kuhn Model. *Nano Letters*, 13(12):6238–6243, 2013.
- [137] A.K.D. Hoogh, N. D. Kusters, N. Rotenberg, H. Acar, H. Zeijlemaker, and L. Kuipers. Optical Activity of Chiral Plasmonic Nanohelices. volume 2542, page 213101, 2015.
- [138] E. Langereis, S. B. S. Heil, H. C. M. Knoops, W. Keuning, M. C .M. van de Sanden, and W. M .M. Kessels. In situ spectroscopic ellipsometry as a versatile tool for studying atomic layer deposition. *Journal of Physics D: Applied Physics*, 42(7):073001, 2009.
- [139] P. Chen, T. Mitsui, D. B. Farmer, J. Golovchenko, Roy G. Gordon, and D. Branton. Atomic Layer Deposition to Fine-Tune the Surface Properties and Diameters of Fabricated Nanopores. *Nano Letters*, 4(7):1333–1337, 2004.
- [140] R. W. Johnson, A. Hultqvist, and S. F. Bent. A brief review of atomic layer deposition: from fundamentals to applications. *Materials Today*, 17(5):236–246, 2014.
- [141] K. Bernal R., M. J. Saly, and Y. J. Chabal. Precursor design and reaction mechanisms for the atomic layer deposition of metal films. *Coordination Chemistry Reviews*, 257(23-24):3271–3281, 2013.
- [142] T. Aaltonen, M. Ritala, T. Sajavaara, J. Keinonen, and M. Leskela. Atomic Layer Deposition of Platinum Thin Films. *Chemistry of Materials*, 15(9):1924–1928, 2003.

- [143] J. Hamalainen, F. Munnik, M. Ritala, and M. Leskela. Atomic Layer Deposition of Platinum Oxide and Metallic Platinum Thin Films from Pt(acac)₂ and Ozone. *Chemistry of Materials*, 20(21):6840–6846, 2008.
- [144] I. J. M. Erkens, M. A. Verheijen, H. C. M. Knoop, T. F. Landaluce, F. Roozeboom, and W.M. M. Kessels. Plasma-Assisted Atomic Layer Deposition of PtOx from (MeCp)PtMe₃ and O₂ Plasma. *Chemical Vapor Deposition*, 20(7-8-9):258–268, 2014.
- [145] A. J. M. Mackus, D. Garcia-Alonso, H. C. M. Knoop, A. A. Bol, and W. M. M. Kessels. Room-Temperature Atomic Layer Deposition of Platinum. *Chemistry of Materials*, 25(9):1769–1774, 2013.
- [146] A. J. M. Mackus, J. J. L. Mulders, M. C. M. Van de Sanden, and W. M. M. Kessels. Local deposition of high-purity Pt nanostructures by combining electron beam induced deposition and atomic layer deposition. *Journal of Applied Physics*, 107(11):116102, 2010.
- [147] W. S. M. Werner, K. Glantschnig, and Cl. Ambrosch-Draxl. Optical Constants and Inelastic Electron-Scattering Data for 17 Elemental Metals. *Journal of Physical and Chemical Reference Data*, 38(4):1013–1092, 2009.
- [148] H.G. Tompkins, S. Tasic, J. Baker, and D. Convey. Spectroscopic ellipsometry measurements of thin metal films. *Surface and Interface Analysis*, 29(3):179–187, 2000.
- [149] Z. Li, P. Beck, D. A.A. Ohlberg, D. R. Stewart, and R.S. Williams. Surface properties of platinum thin films as a function of plasma treatment conditions. *Surface Science*, 529(3):410–418, 2003.
- [150] M. Avrekh, O.R. Monteiro, and I.G. Brown. Electrical resistivity of vacuum-arc-deposited platinum thin films. *Applied Surface Science*, 158(3-4):217–222, 2000.
- [151] R.A. Serway and W. J. Jr John. *Principles of Physics*. Saunders College, 5 edition, 1998.
- [152] J. D. Wrbanek and K. L. H. Laster. Preparation and Analysis of Platinum Thin Films for High Temperature Sensor Applications. *National Aeronautics and Space Administration NASA*, (January):19, 2005.
- [153] Q. G. Zhang, X. Zhang, B. Y. Cao, M. Fujii, K. Takahashi, and T. Ikuta. Influence of grain boundary scattering on the electrical properties of platinum nanofilms. *Applied Physics Letters*, 89(11):114102, 2006.

REFERENCES

- [154] M Cattani and M. C. Salvadori. Electrical resistivity of platinum and gold thin films: A theoretical approach. *Surface Review and Letters*, 11(03):283–290, 2004.
- [155] G. Ramaswamy, a.K. Raychaudhuri, K. Das Gupta, and G. Sambandamurthy. A study of the spatial variation of electric field in highly resistive metal films by scanning tunneling potentiometry. *Applied Physics A: Materials Science & Processing*, 66:S435–S439, 1998.
- [156] H. C. M. Knoop, A. J. M. Mackus, M. E. Donders, M. C. M. van de Sanden, P. H. L. Notten, and W. M. M. Kessels. Remote Plasma ALD of Platinum and Platinum Oxide Films. *Electrochemical and Solid-State Letters*, 12(7):G34, 2009.
- [157] A. S. Chadha, D. Zhao, and W. Zhou. Comparative study of metallic and dielectric helix photonic metamaterial. *Optical Materials Express*, 4(12):2460, 2014.
- [158] C. Rockstuhl, F. Lederer, C. Etrich, T. Zentgraf, J. Kuhl, and H. Giessen. On the reinterpretation of resonances in split-ring-resonators at normal incidence. *Optics Express*, 14(19):8827, 2006.
- [159] E Plum, X.-X. Liu, V A Fedotov, Y. Chen, D. P. Tsai, and N I Zheludev. Metamaterials: Optical Activity without Chirality. *Physical Review Letters*, 102(11):113902, 2009.
- [160] P. G. Blauner. Focused ion beam induced deposition of low-resistivity gold films. *Journal of Vacuum Science & Technology B: Microelectronics and Nanometer Structures*, 7(6):1816, 1989.
- [161] C. Elbadawi, M. Toth, and C. J. Lobo. Pure Platinum Nanostructures Grown by Electron Beam Induced Deposition. *ACS Applied Materials & Interfaces*, 5(19):9372–9376, 2013.
- [162] C. Mansilla, S. Mehendale, J. J. L. Mulders, and P. H. F. Trompenaars. Towards a single step process to create high purity gold structures by electron beam induced deposition at room temperature. *Nanotechnology*, 27(41):415301, 2016.
- [163] K. Mølhave, D.N. Madsen, A.M. Rasmussen, A. Carlsson, C. C. Appel, M. Brorson, C. J. H. Jacobsen, and P. Bøggild. Solid Gold Nanostructures Fabricated by Electron Beam Deposition. *Nano Letters*, 3(11):1499–1503, 2003.
- [164] M. M. Shawrav, P. Taus, H. D. Wanzenboeck, M. Schinnerl, M. Stoger-Pollach, S Schwarz, A Steiger-Thirsfeld, and E. Bertagnolli. Highly conductive and pure gold nanostructures grown by electron beam induced deposition. *Scientific Reports*, 6(July):34003, 2016.

- [165] C. Haverkamp, K. Höflich, S. Jäckle, A. Manzoni, and S. Christiansen. Plasmonic gold helices for the visible range fabricated by oxygen plasma purification of electron beam induced deposits. *Nanotechnology*, 28(5):55303, 2017.
- [166] B. Geier, C. Gspan, R. Winkler, R. Schmied, J. D. Fowlkes, H. Fitzek, S. Rauch, J. Rattenberger, P. D. Rack, and H. Plank. Rapid and Highly Compact Purification for Focused Electron Beam Induced Deposits: A Low Temperature Approach Using Electron Stimulated H₂O Reactions. *The Journal of Physical Chemistry C*, 118(25):14009–14016, 2014.
- [167] M. A. Listvan. Direct observations of small gold clusters and in situ cluster growth by stem. *Journal of Molecular Catalysis*, 20(3):265–278, sep 1983.
- [168] A. Schaub, P. Slepicka, I. Kasparkova, P. Malinsky, A. Mackova, and V. Svorečík. Gold nanolayer and nanocluster coatings induced by heat treatment and evaporation technique. *Nanoscale Research Letters*, 8(1):249, 2013.
- [169] Q. G. Zhang, B. Y. Cao, X. Zhang, M. Fujii, and K. Takahashi. Influence of grain boundary scattering on the electrical and thermal conductivities of polycrystalline gold nanofilms. *Physical Review B*, 74(13):134109, 2006.
- [170] S. J. Randolph, J. D. Fowlkes, and P. D. Rack. Effects of heat generation during electron-beam-induced deposition of nanostructures. *Journal of Applied Physics*, 97(12):124312, 2005.
- [171] M. Bresin, M. Toth, and K. A. Dunn. Direct-write 3D nanolithography at cryogenic temperatures. *Nanotechnology*, 24(3):035301, 2013.
- [172] J. J. L. Mulders, L. M. Belova, and A. V. Riazanova. Electron beam induced deposition at elevated temperatures: compositional changes and purity improvement. *Nanotechnology*, 22(5):055302, 2011.
- [173] A. Botman, J. J. L. Mulders, R. Weemaes, and S. Mentink. Purification of platinum and gold structures after electron-beam-induced deposition. *Nanotechnology*, 17(15):3779–3785, 2006.
- [174] H. W. P. Koops. Conductive dots, wires, and supertips for field electron emitters produced by electron-beam induced deposition on samples having increased temperature. *Journal of Vacuum Science & Technology B: Microelectronics and Nanometer Structures*, 14(6):4105, 1996.
- [175] M. Decker, R. Zhao, C. M. Soukoulis, S. Linden, and M. Wegener. Twisted split-ring-resonator photonic metamaterial with huge optical activity. pages 1–7, 2010.

REFERENCES

- [176] M. Schäferling, X. Yin, N. Engheta, and H. Giessen. Helical Plasmonic Nanostructures as Prototypical Chiral Near-Field Sources. *ACS Photonics*, 1(6):530–537, 2014.

Glossary

C cross-section.

C_{Ry} Rayleigh scattering cross-section.

D_i diffusion coefficient.

G bulk reflection coefficient of platinum.

I intensity.

J precursor flux.

N electron density.

N_A atomic density.

N_{Pitches} Number of pitches.

Q scattering efficiency.

R reflection.

V volume.

V_m volume molecule.

W energy rate.

Δ imaginary part of ξ .

\Re real part.

α polarizability.

β scattering parameter.

χ chirality factor.

δ skin depth.

ε permittivity.

ε_0 vacuum permittivity.

ϵ_{BG} permittivity of the Bruggemann model.

ϵ_{MG} permittivity of the Maxwell-Garnett model.

ϵ_r relative permittivity.

η dissociative cross-section.

γ damping coefficient.

κ extinction coefficient, imaginary part of the refractive index.

λ wavelength of light.

B magnetic flux.

D electric displacement field.

E electric field strength.

H magnetic field strength.

J_P polarization current.

J_{free} free currents.

J_{mag} polarization current.

M magnetization field.

P dipole field.

S poynting vector.

k wavevector.

μ permeability.

μ_0 vacuum permeability.

μ_r relative permeability.

ω angular frequency.

ω_0 eigenfrequency.

ω_P plasma frequency.

ϕ_0 angle of incident.

ψ real part of ξ .

ρ_{bound} free charges.

ρ_{free} free charges.

σ complex conductivity.

τ residual time of a molecule.

\tilde{n} complex refractive index.

φ susceptibility.

$\bar{\omega}$ temperature dependent mean free path of electrons.

ρ resistivity.

ξ complex reflection coefficient.

a absorption coefficient.

c speed of light.

d external diameter of a helix.

e electron charge.

f_b oscillator strength.

f_e electron flux.

g dissymmetry factor.

h height of one helix pitch.

l_{arc} arc length of a helix.

m surface molecular density.

m_0 density of one monolayer.

m_e effective optical electron mass.

n real part of the refractive index.

Glossary

r particle radius.

r_p reflection coefficient p-polarization.

r_s reflection coefficient s-polarization.

t time.

v_F Fermi velocity of electrons.

v_{ph} phase velocity of light.

f volume filling fraction.

s sticking probability.

Acknowledgments

With this I would like to thank all the people who have supported me during the last three years. First, I would like to thank my supervisor Prof. Silke Christiansen for given me the opportunity to do my PhD at the Hemholtz center in Berlin in cooperation with the Max Plank Institut in Erlangen. Special thank for the help during the whole time in Erlangen and Berlin to my adviser Katja Höflich for excellent supervision throughout the whole PhD project. Thanks to all the helpful scientific discussions and helpful guidance regarding presentations and publication in the years.

Especially the 1.5 years in Erlangen have been very instructive. From that time i would also like to thank the whole Christiansen Research Group, in particular to Michael Latzel for the explanation of every detail on every machine in the whole institute. Eduard Butzen for introducing me to SEM, EBID and EDX. Pawel Wozniak for a nice conference time together and helpful information on simulation and optical investigation. Thorsten Feichtner as helpful plasmonic and Lumerical lexicon. Isabel Gäßner, Irina Harder and, Alex Gumann for of gold depositions. Lisa Spann for all administrative support. Ralf Keding for protection against chemicals. Richard Hünermann for optical measurements. George Sarau for the Raman measurements and interpretation. Benjamin Winter for the TEM and EDX measurements. A warm thanks to the whole Lupi family who directly made me feel welcome in Erlangen. I would like to thank the group at the HZB in Berlin. Especially, Lasse Kling, Maximilian Götz and Karin Regelin for nice office conversations, coffee and lunch breaks. Also to Karin for fixing every administrative problem. Holger Kropf for all the help with the SEMs, FIB preparations and always know where to get help. Anna Manzoni and Uli Bloeck for TEM the opportunity to conduct the TEM measurements. Felix Kampmann for the opportunity to do Raman measurements in Berlin. Dagmar Köpnick-Welzel for the opportunity to work in the student lab. I want to say thank you to Ivo Utke for the change to perform experiments at the EMPA in Switzerland and to be always open to answer questions and discuss EBID topics. Christoph Günther for the opportunity to do ellipsometry measurements at the university in Chemnitz. Christoph and Basti for the corrections they gave me. I also would like to say thank you my flatmates from the Muskauer street Christoph and Vivi for the always relaxing atmosphere. Thank you Sara for everything. To the end thank to all friends and family for the support during this time.

CV

The CV is not included in the online version for privacy reasons

Selbständigkeitserklärung

gemäß § 7, Abs. 4 der Promotionsordnung
des Fachbereiches Physik
der Freien Universität Berlin
(Amtsblatt 34/2013, 2.September 2013)

Hiermit versichere ich alle Hilfsmittel und Hilfen angegeben zu haben, auf deren Grundlage die Arbeit selbständig verfasst wurde.

Die vorliegende Arbeit wurde nicht in einem früheren Promotionsverfahren angenommen oder als ungenügend beurteilt.

Berlin, den

.....

(Caspar Haverkamp)